Master's thesis and Internship : Power system dynamics of an islanded wind to hydrogen production hub: parametric assessment of system flexibility under wind power variations

Auteur : Castiaux, Joakim
Promoteur(s) : Cornélusse, Bertrand; Ewbank, Bastien
Faculté : Faculté des Sciences appliquées
Diplôme : Master : ingénieur civil en génie de l'énergie à finalité spécialisée en Energy Networks
Année académique : 2025-2026
URI/URL : http://hdl.handle.net/2268.2/26182

University Of Liege - Faculty Of Applied Sciences

Power system dynamics of an islanded wind to hydrogen production hub: parametric assessment of system flexibility under wind power variations

Master's thesis submitted in partial fulfillment of the requirements for the degree of Master of Science in Energy Engineering, specialized in Energy Networks

Promoter:
Pr. Bertrand Cornelusse

Author:
Joakim Castiaux

Supervisor:
Ir. Bastien Ewbank

Academic year 2025-2026

Acknowledgements

I would like to address a few words to all the people who helped me complete this work, and more generally, my studies.

First, I would like to thank Prof. Cornélusse for his advice, patience, and availability throughout this work, but also for all the interesting lectures over the past years. I would also like to express my sincere thanks to Bastien for his guidance, support, and the time he devoted to helping me.

I also thank all the members of the team for their warm welcome and for making me feel included, especially during the countless coffee breaks.

I would like to deeply thank my parents, who gave me the opportunity to study and who have always supported me, even during the difficult moments.

Finally, a particularly heartfelt thank you goes to Romane, my partner, without whom these studies would not have been the same, and whose unwavering support has meant a great deal to me.

The artificial intelligence tool *ChatGPT* was used as an assistance tool for correcting grammar and spelling mistakes, as well as for rephrasing certain sentences.

Abstract

Large scale wind to hydrogen systems are a promising option for producing low carbon hydrogen in regions with high wind potential. However, when hydrogen production is supplied locally by renewable generation, and especially when the electrical system is operated as an isolated network, the balance between production and consumption must be maintained internally.

This master's thesis explores the dynamic behaviour and stability margins of a simplified wind to hydrogen production hub considered as part of an islanded multi-hub system. The studied system corresponds to a 750 MW hub including converter interfaced wind generation, a converter interfaced electrolyser load, a synchronous condenser and an external synchronous generator. This generator does not represent a specific physical unit of the project, but is used as an equivalent source to model a balancing capability of the rest of the system.

The network is modelled in the RMS phasor domain and simulated with RAMSES. Individual time domain simulations are first used to analyse the physical mechanisms involved after wind power variations. Parametric sensitivity analyses are then performed to assess the influence of the wind ramp size, the electrolyser reaction delay and ramp rate, the external grid strength, the system inertia and the voltage support strategy of the converters.

The results show that, for the investigated disturbances, the frequency response is more critical than the voltage response. The main limiting factor is the duration of the active power imbalance between wind generation and electrolyser demand, which strongly depends on the timing and speed of the electrolyser response. The study also highlights the different roles of synchronous devices, system inertia and converter voltage control in the dynamic performance of the hub. It provides preliminary design indications for the coordinated operation of electrolyser demand, the wind production, the synchronous devices and converter control strategies.

Résumé

Les systèmes de production d'hydrogène à partir d'énergie éolienne de grande puissance constituent une solution prometteuse pour produire de l'hydrogène bas carbone dans les régions présentant un potentiel éolien important. Cependant, lorsque la production d'hydrogène est alimentée localement par une production renouvelable, et en particulier lorsque le système électrique est exploité comme un réseau isolé, l'équilibre entre production et consommation doit être maintenu localement.

Ce mémoire étudie le comportement dynamique et les marges de stabilité d'un hub simplifié de production d'hydrogène à partir d'énergie éolienne, considéré comme faisant partie d'un système isolé composé de plusieurs hubs. Le système étudié correspond à un hub de 750 MW comprenant une production éolienne raccordée par l'intermédiaire d'un convertisseur, une charge d'électrolyseurs également raccordée par l'intermédiaire d'un convertisseur, un condensateur synchrone et un générateur synchrone externe. Ce générateur ne représente pas une unité physique spécifique du projet, mais est utilisé comme une source équivalente afin de modéliser une capacité d'équilibrage du reste du système.

Le réseau est modélisé dans le domaine des phaseurs RMS et simulé avec RAMSES. Des simulations individuelles dans le domaine temporel sont d'abord utilisées afin d'analyser les mécanismes physiques intervenant après des variations de puissance éolienne. Des analyses de sensibilité paramétriques sont ensuite réalisées afin d'évaluer l'influence de l'amplitude de la rampe de puissance éolienne, du délai de réaction et de la vitesse de variation de l'électrolyseur, de la force du réseau externe, de l'inertie du système et de la stratégie de soutien en tension des convertisseurs.

Les résultats montrent que, pour les perturbations étudiées, la réponse en fréquence est plus critique que la réponse en tension. Le principal facteur limitant est la durée du déséquilibre de puissance active entre la production éolienne et la demande de l'électrolyseur, qui dépend fortement du délai et de la vitesse de réaction de celui ci. L'étude met également en évidence les rôles distincts des machines synchrones, de l'inertie du système et du contrôle en tension des convertisseurs dans les performances dynamiques du hub. Elle fournit des indications préliminaires de conception pour une exploitation coordonnée de la demande de l'électrolyseur, de la production éolienne, du support des machines synchrones et des stratégies de contrôle des convertisseurs.

Abreviations and acronyms

CIG	Converter Interfaced Generation
VSC	Voltage Source Converter
PSS	Power System Stabilizer
AVR	Automatic Voltage Regulator
OEL	Over Excitation Limiter
RoCoF	Rate of Change of Frequency
SC	Synchronous Condenser
GFL	Grid Following
GFM	Grid Forming
PLL	Phase-Locked Loop
$\mathbf{H_2}$	Hydrogen
$\mathbf{GH_2}$	Green hydrogen
MW	Megawatt
MVAr	Megavolt Ampere Reactive
MVA	Megavolt Ampere
kV	Kilovolt
Hz	Hertz
AC	Alternative Current
STEPSS	Static and Transient Electric Power Systems Simulation
RAMSES	Rapid Multiprocessor Simulation of Electric power Systems
PFC	Power Flow Computation
PCC	Point of Common Coupling

Table of Contents

Contents

1 Introduction

1.1 Context and motivations

This master's thesis is situated in the broader context of the energy transition, which aims to reduce greenhouse gas emissions, limit climate change, and mitigate the environmental impacts of current energy systems. Over the last two centuries, industrial development has strongly increased productivity and living standards [1], while broader improvements in nutrition, sanitation, public health and medical care contributed to the decline in mortality and to the acceleration of demographic growth [2],[3]. Together with the expansion of energy intensive modes of production and consumption, these changes have led to a sustained long term increase in energy demand and to a strong dependence on fossil fuels, which still account for the vast majority of global primary energy supply [4],[5]. Their large scale combustion remains one of the main contributors to climate change [6], while broader environmental issues, such as biodiversity loss and ecosystem degradation, are expected to be further aggravated by global warming [7].

The energy transition cannot rely on a single technological solution. A first lever is to reduce unnecessary energy consumption, through sobriety measures and better energy management. A second lever is to improve the efficiency of energy conversion and end-use processes [8]. In parallel, the remaining energy demand must progressively be supplied by low-carbon energy sources. Direct electrification is generally considered as one of the most efficient pathways for decarbonising several sectors, including parts of transport, heating and industry [9]. However, some sectors require specific chemical feedstocks, high temperature heat, or energy carriers that are difficult to provide directly with electricity such as aviation, shipping, long-distance transport, and parts of the steel, cement and chemical industries [10],[11].

Hydrogen is therefore expected to play a complementary role in the energy transition for some sectors that are difficult to electrify directly, such as heavy industry, shipping, aviation and seasonal energy storage [12]. Today, global hydrogen production is still largely based on fossil fuels, mainly natural gas and coal, while low carbon hydrogen represents only a small fraction of total production [13]. Replacing conventional hydrogen by hydrogen produced through water electrolysis supplied by renewable electricity is one possible route to reduce emissions in existing hydrogen uses [12]. Hydrogen is already used in several industrial processes, notably in refining, ammonia production and the chemical industry, and it is also considered for future applications such as low-carbon steel production, synthetic fuels and some transport applications [12], [13]. In addition, hydrogen derivatives such as ammonia may facilitate the transport and export of renewable energy from regions with abundant renewable resources to regions with high industrial demand [14].

Large scale wind to hydrogen projects are directly connected to this perspective. They aim to convert renewable electricity into hydrogen or hydrogen derived products, thereby linking renewable power generation with industrial decarbonisation needs. A representative example is the H2 Magallanes project in southern Chile, where strong and regular wind resources are intended to supply electrolysis units producing green hydrogen and green ammonia for export [15]. Such projects differ from conventional renewable power plants connected to a strong transmission grid. Indeed, the balance between production and consumption must be maintained internally.

1.2 Scope of this work

The objective of this thesis is to analyse the dynamic response and stability margins of a simplified wind to hydrogen system. The study focuses on a representative hub of in which flows 750 MW of production and consumption. In the reduced dynamic model, the AC network includes converter interfaced wind generation and electrolyser demand, a synchronous condenser support device and an external synchronous source representing the balancing capability of the surrounding system.

The network is modelled in the RMS phasor domain and simulated with RAMSES. This approach is suited to the analysis of electromechanical dynamics, voltage control behaviour and slow converter-control interactions over time scales ranging from a few seconds to several tens of seconds. It also remains computationally efficient for parametric studies.

The work first defines a reference operating point, including the active and reactive power dispatch, voltage control assumptions and the role of the synchronous support devices. Dynamic simulations are then performed by imposing wind power ramps followed by delayed electrolyser power adjustments. The system response is assessed through frequency deviations, rate of change of frequency (RoCoF), bus voltage excursions, reactive power support and power exchanges with the synchronous machines.

A parametric sensitivity analysis is carried out to identify the most influential parameters, including the wind power variation, the electrolyser reaction delay and ramp rate, the inertia of the synchronous machines, the strength of the external source and the voltage support strategy of the converters. The aim is to identify the main dynamic trends, highlight potentially critical operating conditions and provide preliminary recommendations for the design of the industrial project.

The study is limited to RMS phasor simulations. As a result, very fast electromagnetic phenomena, converter switching dynamics, harmonic interactions and detailed DC side electrolyser dynamics are not represented. Moreover, the electrolyser active power response is imposed through predefined setpoint changes rather than generated by a detailed feedback controller. The results should therefore be interpreted as a first dynamic assessment of the reduced AC system and as a basis for further model refinements.

1.3 Structure of the report

The remainder of the report is organised as follows. Section 2 introduces the industrial project context and describes the electrical architecture considered for the wind to hydrogen hub. Section 3 recalls the main power system stability concepts relevant to converter dominated and weak networks, with emphasis on frequency stability, voltage stability, rotor angle stability and converter-driven interactions. Section 4 presents the RMS phasor approach, the simulation tools, including the RAMSES workflow, but also the wind and electrolyser converter models, the synchronous condenser and the external synchronous generator models.

Section 5 defines the initial steady state operating point and the dynamic study framework. It presents the balancing assumptions, the reference operating point, the disturbance sequence and the performance indicators used to assess the simulations. Section 6 analyses base case simulations with selected time domain responses in order to interpret the main physical mechanisms observed under some typical wind power variations. Section 7 extends the analysis through parametric sensitivity studies and compares the influence of the main system and control parameters, and discusses the design implications of the results. Finally, Section 8 summarises the main conclusions, the limitations and identifies possible directions for future work.

2 Project and system description

2.1 Industrial reference project and simplification

The case study considered in this master's thesis is inspired by large scale wind to hydrogen projects planned in the Magallanes region, in southern Chile. This region is characterized by strong and regular wind resources, the average wind speed at an altitude of 100 meters is [10 - 12] m/s, and it can reach 15 m/s in certain areas [15]. It makes attractive the development of renewable electricity production sites dedicated to green hydrogen (GH_2) and hydrogen derived products. In such projects, wind power is intended to supply electrolysis units, with the produced hydrogen or ammonia being stored and exported.

The idea of this work comes from Elia who is currently working with Total Energies on one of these project : the H_2 Magallanes project. The project is about to install 5000 MW of wind turbines supplying 3500 MW of electrolysers in 4 hubs. They plan to produce 400,000 tons of GH_2 and 2,260,000 tons of green ammonia per year. Allowing to avoid 4 million tons of CO2 emissions per year [15].

However, the system studied here is not intended to reproduce the detailed electrical architecture of Total Energie's project. Instead, it is used as an industrial reference to define realistic orders of magnitude in terms of wind potential, installed power and geographical scale. The electrical network analysed in the following sections is therefore a simplified and fictitious representative system, designed to investigate the dynamic behaviour of an islanded wind to hydrogen network.

2.2 From the 3-GW site to a representative 750-MW hub

In this work, the total system is reduced to one representative hub of 750 MW, corresponding to one quarter of the overall project. The hub is modelled as an AC system including an aggregated wind generation unit, a single electrolyser load, a synchronous condenser and an external synchronous source. The wind plant is represented by a grid following (GFL) voltage source converter (VSC) connected to a 66 kV collection bus. The electrolyser is also represented through a VSC, but with a negative active power injection, corresponding to a controllable electrical load. A synchronous condenser is connected close to the electrolyser bus in order to provide local voltage support and rotating inertia. Finally, an external synchronous generator is connected at the remote end of the network. This generator does not represent a specific physical unit of the industrial project, but the remaining network with the 3 other hubs. It is also introduced to provide a voltage angle reference, active power balancing capability, and additional synchronous dynamics in the reduced islanded system.

2.3 Electrical architecture of the studied hub

The electrical architecture of the reduced hub is shown in Figure 1. The high voltage backbone of the system is operated at 220 kV. The external synchronous generator is connected to bus 1 at 15 kV and stepped up to the 220 kV network through the transformer between buses 1 and 11. The main 220 kV connection between buses 11 and 2 represents the electrical distance between the external

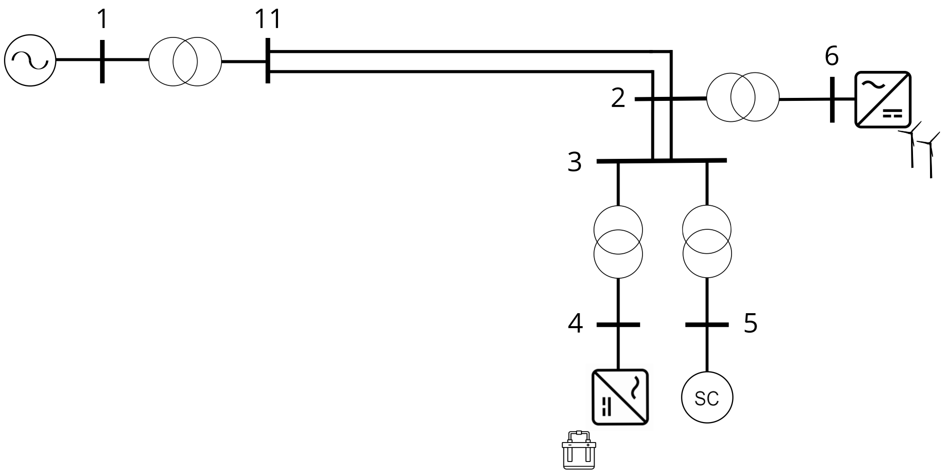

Figure 1: Electrical architecture of the reduced 750 MW wind to hydrogen hub.

source and the wind to hydrogen hub. Two parallel circuits are used for this connection.

The wind generation unit is connected at bus 6, at a voltage level of 66 kV, and is connected to the 220 kV backbone through a 66/220 kV transformer. The electrolyser converter is connected at bus 4, at 20 kV, through a 220/20 kV transformer. The synchronous condenser is connected at bus 5, at 15 kV, through a 220/15 kV transformer. Buses 2 and 3 form the local 220 kV connection between the wind generation area, the electrolyser load and the synchronous condenser. The recapitulatif of the main buses is given in Table 1.

Table 1: Main buses of the reduced 750-MW hub.

Bus	Voltage level	Role
1	15 kV	External synchronous generator terminal bus
11	220 kV	Highv oltage side of the external generator transformer
2	220 kV	Local high voltage bus for wind VSC connection
3	220 kV	Local high voltage bus for electrolyser and synchronous condenser connection
4	20 kV	Electrolyser converter bus
5	15 kV	Synchronous condenser bus
6	66 kV	Aggregated wind converter bus

The distances used in the reduced network are not intended to reproduce an exact geographical layout. They are derived from a simplified spatial interpretation of the reference project area. Since the Mangallanese H2 project is assumed to be composed of four hubs, the total area displayed in Figure 2 is divided into four sub areas. The electrolyser station and the synchronous condenser are placed near the centre of the studied suba rea, while the wind converter point of connection is located electrically close to this load centre. The external synchronous source is placed at the boundary of the suba rea, leading to an equivalent transmission distance of approximately 15 km. Based on this simplified layout, the main connection between the external source and the hub is therefore represented by two parallel lines of 15.7 km. A short 220 kV local connection of approximately 0.33 km is used between buses 2 and 3 in order to separate the wind transformer

Figure 2: Area of the Mangallanese H2 project for the 4 hubs in green.

connection from the electrolyser and synchronous condenser connection, while keeping the hub compact. The parameters of the lines are gathered in Table 2

Table 2: Transmission lines parameter values in the single hub model.

Element	From bus	To bus	Length (km)	R (Ω)	X (Ω)	$\frac{\omega C}{2}$ (μS)
Line 11-2	11	2	15.7	0.78	5.64	26.411
Line 11-2	11	2	15.7	0.78	5.64	26.411
Line 2-3	2	3	0.3	0.02	0.12	0.556
Line 2-3	2	3	0.3	0.02	0.12	0.556

As mentionned the 220 kV level is selected for the high voltage backbone of the hub. This choice is motivated by the power level considered in the study and by the need to keep the current in the main transfer paths within a realistic order of magnitude. For a three phase active power transfer of 750 MW, assuming a power factor close to unity, the current can be approximated by

$$I \approx \frac{P}{\sqrt{3}V}. \tag{1}$$

At 66 kV, this gives a current of approximately 6.6 kA, whereas at 220 kV the current is reduced to approximately 2.0 kA. Since current dependent losses scale with I^2R, using 220 kV instead of 66 kV reduces the order of magnitude of Joule losses by a factor of about 11 for the same transferred power and line resistance. This is also relevant from a thermal point of view, since the current flowing through overhead line conductors is a major contributor to conductor heating under high loading conditions, and thermal ratings are constrained by the maximum admissible conductor temperature and sag [16]. The line parameters are therefore based on typical 220 kV overhead line data [17], and scaled according to the line lengths.

The wind generation unit is connected at 66 kV. This voltage does not represent the low voltage terminals of individual wind turbines, which are typically at 690 V for the Siemens Gamesa SG 6.0-145 turbine considered in the similar Cabo Negro project in Chile [15], [18]. Instead, it represents the AC collection level of the aggregated wind plant. The selected value is consistent with the development of higher voltage collection systems for large wind power plants, especially offshore wind farms, for which 66 kV inter array systems have been increasingly considered and commercialized as a way to reduce overall cable length and losses of the collection grid [19]. The wind plant is then connected to the 220 kV backbone through an 850 MVA transformer, whose rating is chosen slightly above the nominal hub power.

The electrolyser converter is connected at 20 kV through a 220/20 kV transformer. This value is retained as a representative medium voltage (MV) connection level for a large power to hydrogen conversion system, which are typically in the range [6.6 - 35]kV according to recent literature on grid connected electrolysis converters [20], with a step down transformer between the grid and the converter. In the present RMS model, this bus represents the aggregated AC point of connection of the electrolyser conversion system; the internal AC/DC conversion stages and the low voltage DC electrolyser stacks are not explicitly represented.

The external synchronous generator and the synchronous condenser are both connected at 15 kV. The voltage level is inspired by the synchronous machine terminal voltages used in the Nordic transmission test system [21]. Both machines are connected to the 220 kV backbone through step up transformers. The external generator transformer is rated at 800 MVA, in the same order of magnitude as the hub power, while the synchronous condenser transformer is rated at 300 MVA.

The transformer series impedances are represented by their leakage reactance, expressed in percent on the transformer nominal power. The transformer resistance is neglected in the reduced RMS model, since the study does not focus on transformer loss evaluation.

The retained leakage reactances are representative values for large power transformers. In practice, transformer leakage impedance is a design parameter selected according to system requirements and manufacturer specifications, and it affects the voltage drop across the transformer under load. IEC 60076-5 gives minimum impedance values of 12% and above for large two winding transformers [22]. Consequently, a value of 12% is retained for the wind, electrolyser and synchronous condenser transformers. A slightly higher value of 15% is used for the transformer of the external synchronous generator in the reference case. The transformers parameters are gathered in Table 3.

Table 3: Transformers retained in the reduced hub model.

Element	From bus	To bus	Voltage levels	Rating (MVA)	R_{tr} (%)	X_{tr} (%)
Wind transformer	6	2	66/220 kV	850	0.0	12.0
Electrolyser transformer	3	4	220/20 kV	800	0.0	12.0
Synchronous condenser transformer	3	5	220/15 kV	300	0.0	12.0
External generator transformer	1	11	15/220 kV	800	0.0	15.0

3 Power system stability in converter dominated grids

3.1 Classical stability concepts

The concept of stability in power systems was defined in [23] as *the ability of an electric power system, for a given initial operating condition, to regain a state of operating equilibrium after being subjected to a physical disturbance, with most system variables bounded so that practically the entire system remains intact.* Historically, stability studies mainly focused on power systems dominated by synchronous machines, where the most important dynamic phenomena were slow electromechanical responses involving generators, their control systems, and loads.

With the increasing penetration of power electronic converters, this classical view has changed. Converter interfaced generation (CIG) and loads introduce control driven dynamics over a wider range of time scales, making some fast phenomena more relevant for system stability than in traditional synchronous machine based systems. This section therefore reviews the main stability concepts presented in [24], with the additional context of converter dominated grids, and discusses their relevance for the present work. The different stability phenomena are illustrated in Figure 3.

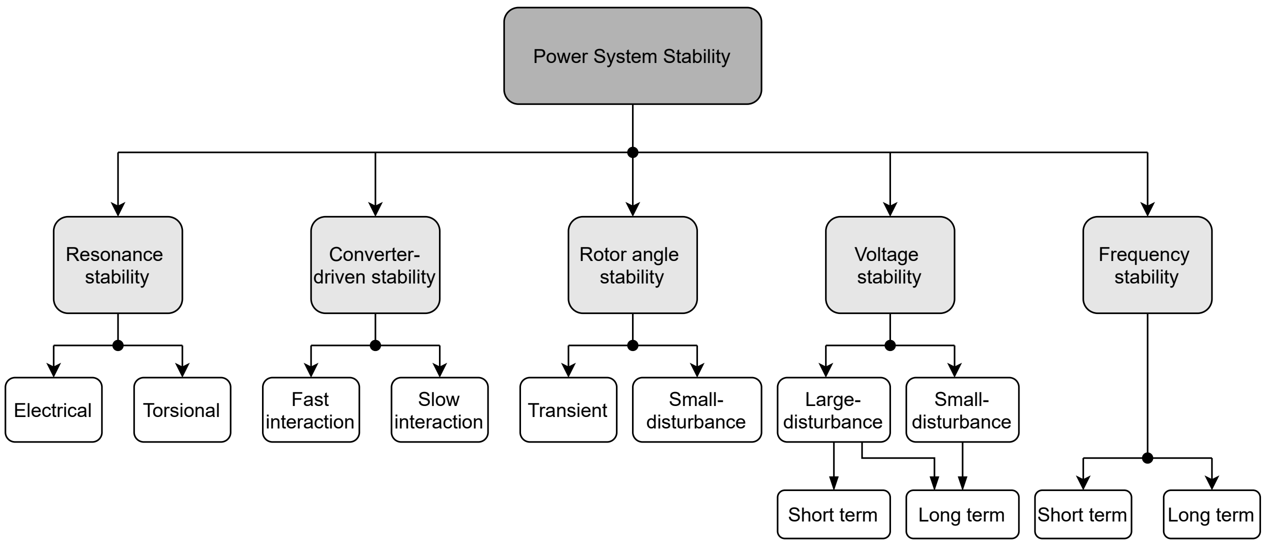

Figure 3: Different stability classes in power systems with high penetration of converter interfaced devices [24].

3.2 Frequency stability

Frequency stability refers to the ability of a power system to maintain the system frequency within acceptable limits following a disturbance that creates an imbalance between active power generation and load demand. Such disturbances may include the loss of a generating unit, a sudden variation of renewable production or a load change. Since frequency is directly linked to the active power balance of the system, frequency stability is mainly governed by the available kinetic energy, the speed of active power control actions, and the amount of reserve that can be mobilized after the disturbance [23], [24].

In conventional power systems dominated by synchronous machines, the first response to an active power imbalance is provided by the stored kinetic energy of rotating masses. Immediately after a sudden loss of generation, the electrical demand cannot change instantaneously. The missing power is therefore temporarily supplied by the deceleration of synchronous machines. This physical response is not the result of a control action, but follows directly from the electromechanical dynamics of synchronous generators. The imbalance between mechanical and electrical power causes the rotor speeds to decrease, which leads to an initial decline of the system frequency. The initial slope of this frequency deviation is commonly characterized by the RoCoF, which is strongly influenced by the total inertia connected to the system.

After this initial inertial phase, primary frequency control acts to arrest the frequency deviation. In synchronous generation units, this response is generally provided by turbine governors through droop control. Generators operating below their maximum active power capability can increase their mechanical power output and compensate part of the initial imbalance. Load damping may also contribute to the frequency response, since some loads naturally consume less active power when the frequency decreases. However, this contribution is usually limited compared with the response provided by generation reserves. The combined effect of inertia, primary control, and load damping determines the frequency nadir and the ability of the system to settle to a stable post disturbance operating point.

At a slower time scale, secondary frequency control, often implemented through automatic generation control, restores the frequency towards its nominal value. This action modifies the active power set points of selected generating units in order to remove the steady-state frequency error left by primary control. Therefore, the overall frequency response of a power system can be interpreted as a sequence of mechanisms acting over different time scales: an immediate inertial response, a primary response that limits and stabilizes the frequency excursion, and a secondary response that restores the nominal frequency.

The stability and quality of the frequency response depend on several factors. The most important are the total inertia of the system, the available active power reserves, the dynamic performance of primary frequency controllers, and the amount of frequency-dependent load damping. Systems with large inertia generally exhibit slower frequency variations and lower RoCoF after a disturbance. Conversely, smaller or weakly interconnected systems, or systems with reduced synchronous generation, may experience faster frequency deviations and more oscillatory responses. In such systems, the design and tuning of active power controls become particularly important.

The increasing penetration of CIG changes the nature of the frequency response. Unlike synchronous machines, these units are not directly coupled to the grid through electromechanical dynamics. In Type-4 wind turbines, the generator is connected to the AC system through a full scale converter, so the kinetic energy stored in the rotating parts is not automatically released during frequency transients. Unless specific frequency support loops are implemented, a GFL converter mainly tracks its active power reference and synchronizes with the grid through a phase-locked loop (PLL).

Fast frequency support can nevertheless be implemented through converter control. In wind turbines, synthetic inertia consists in temporarily increasing the active power reference in response to a frequency deviation or RoCoF, thereby extracting kinetic energy from the rotating masses, i.e. from the blades and the hub[25]. Primary frequency response can also be provided when active power margin is available[26],[27]. Such services can be faster than conventional turbine-governor responses, but they remain constrained by converter current limits, available energy, and the operating point of the renewable source. In wind power plants, upward active power reserve generally requires operating below the maximum power point, which introduces an economic trade-off.

Consequently, frequency stability in systems with high CIG cannot be assessed only from the renewable penetration level. It also depends on the remaining synchronous inertia, the available active power reserves, and the frequency-support functions implemented in the converters. A reduction in synchronous inertia generally increases RoCoF and may lead to deeper frequency nadirs if no fast active power support is available.

In the present work, the wind turbines are represented as full converter units operated in GFL mode, without explicit synthetic inertia or primary frequency response. Their active power behaviour is therefore determined by the imposed active power reference and its associated control dynamics. The electrolyser is also a full converter device modelled as a negative load with no frequency dependent response. As a result, the inertial response of the system is provided by the external synchronous generator and the synchronous condenser, while sustained primary frequency control is provided only by the synchronous generator. The synchronous condenser does not provide sustained active power reserve.

In the following dynamic simulations, the frequency response will be compared with broad frequency withstand limits of 47.5 and 51.5 Hz. These values are based on the European Network Code on Requirements for Grid Connection of Generators [28], which specifies that, in the Continental Europe synchronous area, power-generating modules must be capable of remaining connected and operating for at least 30 min in the 47.5–48.5 Hz range and for 30 min in the 51.0–51.5 Hz range, while operation in the 49.0–51.0 Hz range is required without time limitation. These limits are therefore used here as broad admissible bounds for assessing the simulated frequency excursions, rather than as normal operating frequency-quality limits.

3.3 Voltage stability

Voltage stability is defined as the ability of a power system to maintain bus voltages within acceptable limits, both in normal operating conditions and following a disturbance. This requires the generation units and the transmission network to supply the demanded active and reactive power without causing excessive voltage drops across the network impedances[23],[24].

Unlike frequency stability, which is linked to the overall active power balance of the system, voltage stability has a more local character. Voltage conditions may therefore differ significantly from one area of the network to another. They are influenced by the electrical distance between generation and load centres, the strength of the transmission network, the availability and location of reactive power support, and the dynamic behaviour of the connected loads.

The underlying mechanism of voltage instability is not simply the occurrence of low voltage magnitudes, but rather the inability of the system to recover a stable voltage operating point after a disturbance. In some cases, load-restoration mechanisms or control actions may try to maintain the consumed power despite a reduction in voltage. This increases the current drawn from the network and may raise the reactive power demand, which further aggravates the voltage depression. If the available reactive power reserves from generators, synchronous condensers, capacitor banks, or converter interfaced devices become insufficient, the voltage decline may become progressive and eventually lead to voltage collapse.

Nowadays, GFL and grid forming (GFM) converters are both popular technologies for interfacing renewable energy sources in the energy industry. GFL technology is currently the main source of connection in the industry, due to its maturity, low cost and its numerous different models[29],[30]. Hybrid operation of renewable energy stations combining GFL and GFM converters has also been proposed in the literature to improve voltage and frequency support under weak grid conditions. In particular, such strategies can adapt the converter control mode and support actions according to the grid strength, which is assessed through the short circuit ratio (SCR)[31]. In this thesis, however, only Type 4 wind turbines operated in GFL mode are considered, and GFM control is not further investigated. The complete model the VSC used is developped in the next section.

Voltage stability is usually divided into short-term and long-term voltage stability, according to the dynamics involved.

3.3.1 Short-term voltage stability

Short-term voltage stability concerns voltage dynamics over a time frame of a few seconds. It involves fast acting components such as induction motors, electronically controlled loads, HVDC links, and inverter based resources [24]. In this time range, dynamic models of loads and converter controls are required. Typical mechanisms include the stalling of induction motors after faults, the response of power electronic loads, or the interaction between converter controls and weak network conditions.

In systems with a high share of VSCs, short-term voltage stability can also be influenced by the current limits and control strategies of the converters. Although VSCs can provide fast reactive power and voltage support, their capability remains limited by their maximum current. This constraint can be written as:

$$i_d^2 + i_q^2 \leq I_{\max}^2, \tag{2}$$

where i_d and i_q are respectively the active and reactive current components. Therefore, when a large active current is required, the remaining margin for reactive current injection is reduced. During voltage disturbances, the converter control strategy and current-priority logic directly affect the amount of voltage support that can be provided. Moreover, in weak grids, the PLL and inner current control loops can interact with the network dynamics, especially when the short-circuit strength is low[32].

3.3.2 Long-term voltage stability

Long-term voltage stability is related to slower mechanisms, with time scales ranging from several tens of seconds to several minutes. It is associated with devices such as load tap-changing transformers, thermostatically controlled loads, generator field current limiters, and other protection or restoration mechanisms [17],[24]. Unlike short-term phenomena, long-term voltage instability is often not caused directly by the initiating disturbance itself, such as the outage of a transmission line, generator, or reactive power source. The post disturbance system may initially remain stable, but subsequent slow control actions can progressively reduce the voltage stability margin. For example, load tap-changing transformers may attempt to restore distribution side voltages after a disturbance. This action tends to restore the load demand seen from the transmission system, thereby increasing the power that must be supplied through an already weakened network and worsening the voltage depression. Similarly, when synchronous machines reach their excitation or armature current limits, their ability to provide reactive power and voltage support is reduced, which can further contribute to voltage degradation.

In the system studied in this work, classical long-term voltage collapse mechanisms such as distribution load tap changers are not the main focus. However, voltage stability remains important because the network contains large converter interfaced wind generation and electrolyser load. The voltage response is therefore strongly influenced by the network strength, transformer and line impedances, the reactive power capability of the synchronous condenser and the external generator, and the voltage or reactive power control strategy of the VSCs. The current limits of the converters are also essential, since they constrain the amount of reactive current that can be injected during voltage disturbances.

3.4 Rotor angle stability

Rotor angle stability refers to the ability of synchronous machines to remain in synchronism under normal operating conditions and to return to a stable equilibrium following a small or large disturbance [23]. This phenomenon concerns the synchronous generators and motors that remain connected to the power system. It is governed by the electromechanical motion of their rotors, which can be described by the swing equation:

$$2H\frac{d\omega}{dt} = T_m - T_e - D(\omega - \omega_{\mathrm{ref}}), \tag{3}$$

where H is the inertia constant, ω is the rotor speed, ω_{ref} is the angular speed of the reference frame, T_m is the mechanical torque, T_e is the electromagnetic torque, and D represents damping. The latter will not be used in this work. The rotor angle evolves according to the speed difference between the rotor and the reference frame:

$$\frac{1}{\omega_N}\frac{d\delta}{dt} = \omega - \omega_{\mathrm{ref}}, \tag{4}$$

where ω_N is the nominal angular frequency.

The mechanical torque is determined by the turbine and its speed governor, while the electromagnetic torque represents the electrical torque exerted by the stator currents and the network on the rotor. In generator operation, this electromagnetic torque opposes the mechanical torque and extracts energy from the rotating mass. The electromagnetic torque is related to the electrical power through the rotor speed. In physical units, this relation can be written as

$$P_e = T_e \omega \tag{5}$$

A useful physical interpretation is that the electromagnetic torque tends to reduce the angular displacement between the rotor magnetic field and the magnetic field created by the stator currents. This interpretation is consistent with the simplified power-angle relation commonly used in classical transient-stability analysis:

$$P_e \approx \frac{E'V}{X} \sin(\delta), \tag{6}$$

where E' is an internal voltage, V is the terminal voltage, X is an equivalent reactance, and δ is the rotor angle. This relation illustrates the influence of the rotor angle on active power transfer and the synchronizing effect of the electromagnetic torque.

However, this expression relies on simplifying assumptions and should not be interpreted as the equation used to compute the electromagnetic torque in STEPSS. In the synchronous-machine model used in STEPSS, the electromagnetic torque is computed from the Park variables as

$$T_e = \psi_d i_q - \psi_q i_d. \tag{7}$$

Using the flux-current relationships and the transformation between the machine d-q axes and the network reference frame, STEPSS rewrites this expression as

$$T_e = \psi_{ad}(\cos\delta\, i_x + \sin\delta\, i_y) - \psi_{aq}(-\sin\delta\, i_x + \cos\delta\, i_y). \tag{8}$$

Thus, although the rotor angle δ appears explicitly in the torque expression, the electromagnetic torque is not determined by this angle alone. It is computed from the machine fluxes and currents, and it then acts on the mechanical motion of the rotor through the swing equation.

Following a disturbance, any imbalance between mechanical and electromagnetic torque causes an acceleration or deceleration of the rotor, according to Eq. 3. A larger inertia constant H reduces the rate of variation of the rotor speed, which explains why inertia is a central concept in power-system stability studies. The resulting speed deviation changes the rotor angle through Eq. 4. This modifies the electrical conditions seen by the machine and therefore changes the electromagnetic torque, which may either restore synchronism or amplify the deviation. Around an operating point, the incremental electromagnetic torque can be decomposed into synchronizing and damping components:

$$\Delta T_e = T_s \Delta\delta + T_d \Delta\omega. \tag{9}$$

The synchronizing torque component is associated with rotor-angle deviations, while the damping torque component is associated with speed deviations [17]. Insufficient synchronizing torque leads to aperiodic instability, whereas insufficient damping torque leads to oscillatory instability.

In this work, the total inertia of the system is low. The electromechanical inertia available in the RMS model is provided only by the synchronous machines explicitly represented, namely the external synchronous generator and the synchronous condenser. Consequently, rotor angle and frequency dynamics are strongly influenced by the inertia constants, excitation systems and damping properties of these machines. The rotor angle stability of these remaining synchronous machines are affected by the penetration of CIG and load, since these units do not increase the amount of synchronous inertia and modify the electromechanical dynamics of the system [33].

3.4.1 Small-disturbance rotor angle stability

It is the ability to remain in synchronism after small disturbances. Power systems are continually subjected to small variations of loads and generation. Instabilities resulting from these can be of two forms :

- Aperiodic instability : due to a lack of synchronizing torque.
- Oscillatory instability : due to a lack of damping torque.

On one hand, with constant field voltage generator, i.e without AVR, small-disturbance instability is classically associated with insufficient synchronizing torque, leading to a non-oscillatory divergence of the rotor angle. On the other hand, with an AVR as excitation control, the synchronizing torque is generally improved, but the excitation control may reduce the damping of electromechanical modes, or even introduce negative damping [34]. In that case, instability takes the form of poorly damped or growing oscillations [17]. For this reason, power system stabilizers (PSSs) are added to excitation systems in order to provide supplementary damping torque.

3.4.2 Transient rotor angle stability

Transient rotor angle stability is the ability to remain in synchronism after a large disturbance: like the short circuit of a line or the disconnection of large loads or generation devices. In transient stability studies, the rotor-angle deviations may be large, so the nonlinear power-angle relation in Eq. 6 must be considered rather than only its linearized form around the operating point. Usually, the system is different post disturbance because the fault is cleared by the protection system. In stable situations, the rotor angle will reach a maximum and then oscillate back down until steady state is reached. In unstable situations, rotor angle can either continuously increase and lose synchronism, it is called first swing instability. It is caused by unsufficient synchronizing torque. Or it can also have growing oscillations, which will cause the generator to lose synchronism after a few swings because the system is not "small disturbance stable". It can be due to unsufficient damping and or synchronizing torques, but also with conflicting control interactions between the different controllers of the network [35].

3.5 Converter-driven stability

Converter-driven stability refers to stability phenomena that arise from the dynamic interaction between power electronic converters, their control systems, and the surrounding AC network. This category becomes increasingly relevant in systems with a high share of CIGs, since the behaviour of these devices is mainly determined by control loops rather than by the electromechanical laws governing synchronous machines[36],[24]. In GFL converters, important control components include the PLL, the inner current controller, and the outer active/reactive power or voltage control loops. The different time scales of converter control systems, ranging from very fast inner current control dynamics to intermediate PLL dynamics and slower outer power or voltage control loops, can give rise to stability phenomena over a broad frequency range [37]. Converter-driven stability issues are therefore commonly distinguished between fast and slow interaction phenomena.

3.5.1 Fast interactions

Fast interaction phenomena involve relatively high frequency dynamics, typically from several tens or hundreds of hertz up to the kilohertz range. They are mainly associated with the fast control dynamics of power electronic converters, including the inner current control loop, control delays, PWM and switching actions, and their interaction with fast responding parts of the power system or with other nearby converters. These interactions may result in high frequency oscillations or harmonic instability. Their analysis generally requires detailed electromagnetic transient models or frequency domain impedance based methods. Since the present work relies on the RMS phasor approximation, fast electromagnetic dynamics are not explicitly represented and these fast interaction phenomena are outside the scope of the simulations [24],[38].

3.5.2 Slow interactions

Slow interaction converter-driven stability refers to low frequency or subsynchronous phenomena caused by the coupling between converter control loops and the slower dynamics of the AC system. In GFL converters, the most relevant control components are the PLL and the outer active/reactive power or voltage control loops. These controls interact with the voltage magnitude and phase angle at the point of connection, with the power transfer capability of the network, and with the electromechanical dynamics and controllers of nearby synchronous machines. These interactions become more critical in weak grids, where the synchronization and control action of GFL converters are more sensitive to the voltage magnitude and phase angle at the point of connection. In this context, the PLL response, the outer loop parameters, the converter power setpoints, and the operating point can significantly influence the damping of low frequency modes. Poorly damped interactions may then lead to sustained or growing low frequency oscillations, particularly under low grid strength or high power transfer conditions. Although such phenomena may resemble voltage instability when power transfer limits are involved, they differ from classical voltage instability because the underlying mechanism is mainly driven by converter controls rather than by load restoration dynamics [24],[38].

In the present system, both the wind generation and the electrolyser are represented by GFL VSC models connected to the AC network. The wind converter injects active power into the system, whereas the electrolyser is modelled as a converter-interfaced controllable load, represented by a negative active power injection. Since the VSC models include PLL synchronization, inner and outer control loops, and either reactive power or voltage control capability, the RMS phasor model can capture part of the slow converter-grid interactions associated with these controls.

3.6 Resonance stability

Resonance stability refers to the ability of a power system to avoid poorly damped or growing oscillations caused by the interaction between electrical network dynamics, mechanical shaft dynamics, and fast control devices. In classical power systems, this topic is mainly associated with subsynchronous resonance (SSR), where an electrical resonance of the network interacts with a turbine-generator at frequencies below the fundamental frequency. Such interactions may involve the torsional modes of a synchronous generator shaft, or may be purely electrical, for example when series compensation interacts with the electrical characteristics of a generator.

A first form of resonance instability is torsional resonance. In this case, the electrical network exchanges energy with the mechanical shaft of a turbine-generator at one of its natural torsional frequencies. If the damping of this interaction is insufficient, the oscillation may grow and lead to mechanical stress on the shaft. This phenomenon is mainly relevant for conventional turbine-generator units connected to networks with series-compensated lines or with fast acting power electronic devices interacting with their torsional modes.

A second form is electrical resonance, where the instability is mainly associated with the electrical characteristics of the network and the connected devices. This includes, for example, interactions between series capacitors and induction generators, or control interactions involving CIG. In wind power systems, this topic has been particularly discussed for DFIG based wind turbines connected near series-compensated lines, where the rotor side converter control can contribute to negative damping at subsynchronous frequencies [24].

Resonance stability is not investigated in this work. The RMS phasor approximation represents the AC system through fundamental frequency phasors and does not explicitly model the frequency components associated with subsynchronous or high frequency resonances. Therefore, SSR, subsynchronous control interactions phenomena, and other converter-network resonance phenomena are outside the scope of the simulations.

4 Modelling and simulation tools

In this section is presented the simulation environment and the dynamic models used in the study. The objective is not to derive each controller in detail, but rather to describe the main control loops and the role of the different components in the dynamic response of the system. The system considered includes two GFL voltage source converters, representing the wind generation unit and the electrolyser load, one synchronous condenser and one external synchronous generator, as already enumerated earlier.

4.1 RMS phasor simulation

The dynamic simulations are performed in the RMS phasor domain. In this approach, the fast sinusoidal variation of the AC voltages and currents at the fundamental frequency is not simulated explicitly. Instead of computing the instantaneous waveforms, the model follows the evolution of their fundamental-frequency phasors. For a bus voltage, this means that the instantaneous quantity

$$v_i(t) = \sqrt{2}V_i(t)\cos(\omega_{\text{ref}}t + \phi_i(t)) \tag{10}$$

is instead represented by the slowly varying phasor

$$\overline{V}_i(t) = v_{x,i}(t) + jv_{y,i}(t), \tag{11}$$

expressed in a common rotating reference frame. The quantities $v_{x,i}$ and $v_{y,i}$ are the rectangular components of the voltage phasor. Similar phasor representations are used for currents flowing in the network.

With this representation, the network itself is described by algebraic equations rather than by differential equations. In compact complex form, the network equations can be written as

$$\overline{I} = Y\overline{V}, \tag{12}$$

where $\overline{I}$ is the vector of complex current injections into the network, $\overline{V}$ is the vector of complex bus voltages and Y is the bus admittance matrix. By separating real and imaginary parts, this relation becomes

$$\begin{bmatrix} i_x \\ i_y \end{bmatrix} = \begin{bmatrix} G & -B \\ B & G \end{bmatrix} \begin{bmatrix} v_x \\ v_y \end{bmatrix}, \tag{13}$$

where G and B are respectively the conductance and susceptance matrices of the network. This equation links the voltage phasor components at all buses to the current phasor components injected by the connected devices.

However, the dynamic behaviour of the system is not described by the network equations alone. As explained the network imposes algebraic constraints between bus voltages and injected currents, but the components connected to the buses introduce the dynamic states of the system. Excitation systems and torque controllers of the synchronous machines, VSCs contribute through their own dynamic models, and their outputs must remain consistent with the algebraic network equations. The complete RMS model is therefore formulated as a set of differential-algebraic equations. At each simulation time step, the differential equations of the dynamic components are algebraized in a first place and then solved together with the algebraic network constraints.

With this approximation, the study focuses on electromechanical dynamics, voltage control behaviour, frequency response and slow converter-grid interactions over time scales ranging from a few seconds to several tens of seconds. Compared with electromagnetic transient simulations, the RMS phasor approach is computationally more efficient because it avoids the explicit simulation of the fundamental-frequency sinusoidal waveforms and of the fast switching dynamics. Since the next sections involve parametric sensitivity studies, it is therefore more appropriate to use a lighter computational approach.

However, this modelling choice also defines the limits of the study. The model cannot capture PWM effects, harmonics, high-frequency resonances, very fast electromagnetic transients, etc. The results must therefore be interpreted only as a dynamic assessment of the fundamental-frequency behaviour, rather than as a detailed electromagnetic transient analysis.

4.2 STEPSS and RAMSES workflow

The simulations are carried out with STEPSS, which includes three main modules: PFC for power-flow computation, RAMSES for time-domain dynamic simulation, and CODEGEN for the integration of user-defined dynamic models. The role of PFC is to compute the initial operating point of the network. This includes the bus voltage magnitudes and phase angles, as well as the initial active and reactive power flows. This operating point is then used as the initial condition for RAMSES.

RAMSES solves the dynamic response of the system after the application of disturbances or control actions specified by the user. The complete model is formulated as a set of differential-algebraic equations.

In the present work, the input data are organised into separate files containing the network and power flow data, the dynamic models and the disturbance sequence. The network data define the buses, lines and transformers. The dynamic data define the synchronous machines, their controllers and the VSC models. Disturbances are imposed through scenario files, which are for instance used to modify active power setpoints of the VSCs during the simulation. Python scripts are then used to automate the simulation campaign, generate the different cases, run PFC and RAMSES and post process the output trajectories.

4.3 Implementation of the network model

The electrical network described in Section 2 is implemented using bus, line, transformer and injection data. The transmission lines are represented by their positive-sequence π-equivalent parameters, including series resistance, series reactance and shunt susceptance. The transformers are represented by their leakage reactance, nominal apparent power and transformation ratio.

The sign convention used in the dynamic data is based on power injections into the AC network. Therefore, a positive active power corresponds to a component injecting power into the system, while a negative active power corresponds to a component consuming power from the system. This convention is used for the electrolyser model, which is represented as a converter-interfaced controllable load with a negative active power injection.

The numerical data of the network models are reported in Appendix C.

4.4 Wind generation model

The wind generation unit is represented as an aggregated Type-IV wind power plant. The aerodynamic part of the wind turbine, the mechanical shaft dynamics and the generator side converter are not represented. Instead, the model focuses on the AC side behaviour of the VSC connected to the network.

This simplification is consistent with the objective of the study, which is to analyse the dynamic response of the reduced AC system rather than the internal behaviour of individual wind turbines. The active power of the wind plant is determined by an imposed active power reference and by the dynamics of the converter control loops. No synthetic inertia or primary frequency support loop are included in the wind converter model.

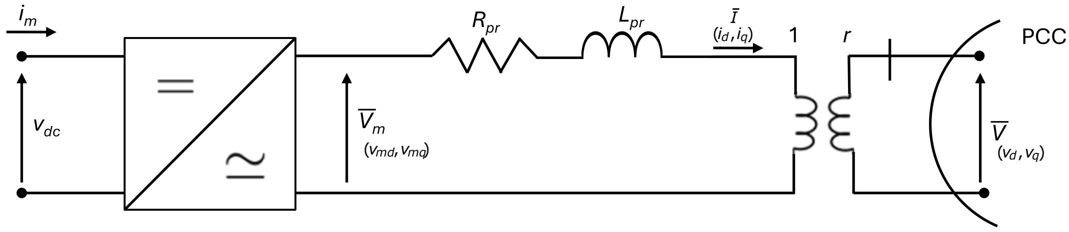

Figure 4: Main view of the VSC model of the wind generation unit.

As shown in Figure 4, the converter is connected to the point of common coupling (PCC) through an equivalent resistance, an equivalent inductance and a transformer. The converter controls the voltage components at its AC terminal in order to regulate the current injected into the network.

4.4.1 Reference frame and PLL

The converter operates in GFL mode. It therefore does not impose its own voltage angle on the network, but synchronises with the local AC voltage through a PLL. The PLL estimates the phase angle of the PCC voltage and defines the rotating dq reference frame used by the current and power controllers.

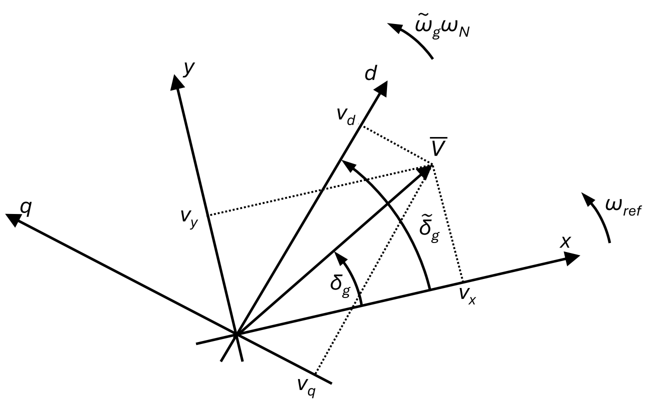

Figure 5: Reference frames used for the VSC control.

The network voltage is first expressed in the fixed xy reference frame used by the RMS simulation. The PLL then computes the angle $\tilde{\delta}_g$ between this fixed frame and the converter dq frame as shown on Figure 5. The goal of the PLL is to align the d-axis with the voltage phasor, which means that the q-axis voltage component should be driven towards zero. The q-axis voltage component can be written as

$$v_q = v_y \cos(\tilde{\delta}_g) - v_x \sin(\tilde{\delta}_g). \tag{14}$$

Figure 6 shows that the PLL acts on this signal through a proportional-integral (PI) control to update the speed of the rotating dq frame to reduce v_q and achieve synchronization.

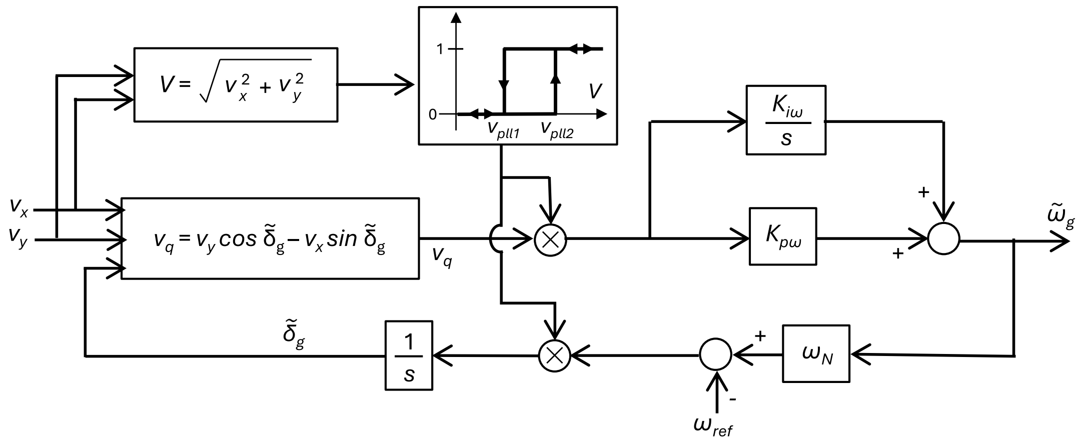

Figure 6: Phase-locked loop of the grid-following VSC from [39].

This synchronisation mechanism is central for GFL converters. Under strong grid conditions, the PCC voltage angle is well defined and the PLL can track it without difficulty. In weak grid conditions, however, the voltage angle becomes more sensitive to converter current injections and network impedance. The PLL can then interact with the surrounding AC system and influence the damping of low frequency modes. In addition, the PLL includes a voltage dependent blocking logic. Indeed, when the PCC voltage falls below a specified threshold, the PLL response can be blocked to avoid unreliable angle tracking. In such severe voltage dip conditions, the converter therefore loses part of its ability to synchronise properly and to provide controlled support to the system.

4.4.2 Inner current control loops

The inner current controller regulates the converter current components i_d and i_q in the dq rotating reference frame. The d-axis current is mainly associated with active power exchange, while the q-axis current is mainly associated with reactive power exchange and voltage support.

As shown in Figure 7, both current components are regulated by PI controllers. The inputs of these controllers are the errors between the reference currents i_d^{ref} and i_q^{ref} and the measured currents i_d and i_q injected by the VSC at the previous iteration. The outputs are the converter voltages v_{md} and v_{mq}.

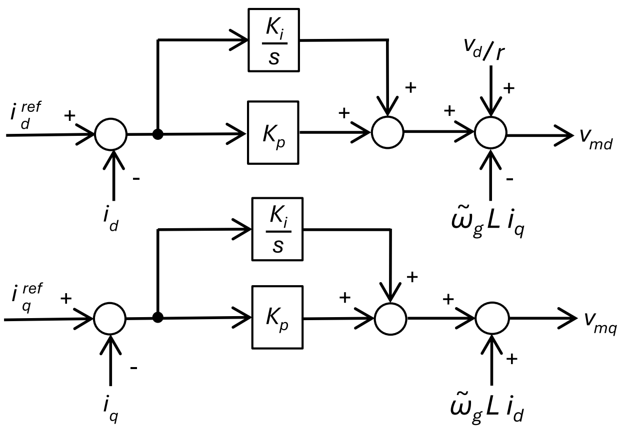

Figure 7: Inner current control loops of the VSC [39].

The controller also includes feedforward and decoupling terms. The voltage term v_d/r accounts for the voltage at the point of connection across the transformer, while the terms involving $\tilde{\omega}_g L i_q$ and $\tilde{\omega}_g L i_d$ compensate the cross-coupling between the two axes introduced by the converter filter inductance. This allows the d- and q-axis current loops to be treated approximately as two independent control channels.

4.4.3 Active power control

The active power outer loop in Figure 8 generates the d-axis current reference used in previous loops. To do so, it measures active power and filters it in order to avoid excessive sensitivity to fast variations. The filtered value is then compared with the active power reference $P^\star$ which is imposed or modified with the disturbance file. The resulting error is processed by a PI controller, whose output gives the preliminary d-axis current reference.

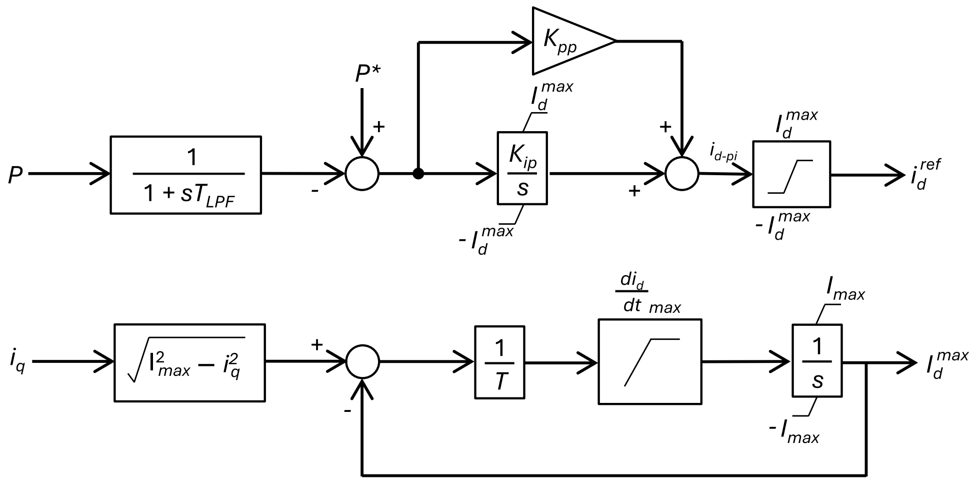

Figure 8: Active power outer control loop of the VSC [39].

The active current reference is limited by the converter current capability. Since the total current is constrained by

$$i_d^2 + i_q^2 \leq I_{\max}^2, \tag{15}$$

the available margin for active current depends on the reactive current already required by the q-axis control. The lower branch of Figure 8 computes the maximum admissible active current I_d^{max} based on Equation 15, from the instantaneous value of i_q. A rate limiter is applied to the recovery of this limit, so that the active current capability is not restored instantaneously after being reduced by an increase in reactive current. This avoids a sudden recovery of active power and reflects the priority given to reactive current when voltage support is required.

4.4.4 Reactive power and voltage control

The q-axis current reference used in the inner loops is generated by the reactive power or voltage control loop shown on Figure 9. The converter can operate either in reactive power control or in voltage control mode. In reactive power control, the measured reactive power is compared with a reference value Q^0. In voltage control mode, a compensated voltage magnitude V_{comp} is compared with a voltage reference V^0_{comp}. The compensated voltage is reconstructed from the PCC voltage and the converter current as

$$\overline{V}_{comp} = \frac{\overline{V}}{r} + k\left(R_c + jX_c\right)\overline{I}_{xy}, \tag{16}$$

where $\overline{V}$ is the PCC voltage phasor, r is the transformer ratio, $\overline{I}_{xy} = i_x + ji_y$ is the current phasor built from the x- and y-axis current components, and

$$k = r\frac{S_{base}}{S_{nom}}$$

is the current conversion factor used to express the current on the appropriate base for the voltage drop compensation. In this work, the compensation impedance is chosen equal to the physical series impedance of the converter interface:

$$R_c = R_{pr}, \qquad X_c = X_{pr}.$$

Therefore,

$$\overline{V}_{comp} = \frac{\overline{V}}{r} + k\left(R_{pr} + jX_{pr}\right)\overline{I}_{xy} \simeq \overline{V}_m. \tag{17}$$

Thus, $|\overline{V}_{comp}|$ corresponds to the reconstructed converter-side voltage magnitude $|\overline{V}_m|$ shown in Figure 4.

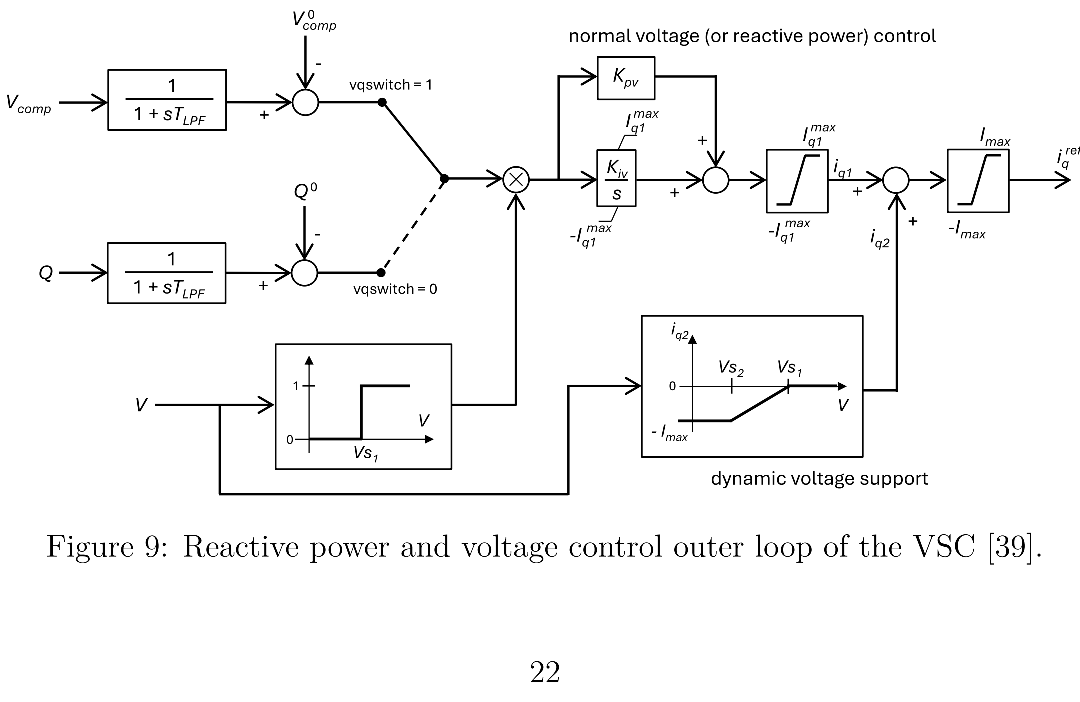

Figure 9: Reactive power and voltage control outer loop of the VSC [39].

Then, the selected error is processed by a PI controller to obtain the main reactive current contribution i_{q1} during normal operation. The model also includes a dynamic voltage support branch, which is activated when the PCC voltage falls below a specified threshold. With the sign convention used in the model, the reactive power is given by

$$Q = v_q i_d - v_d i_q \simeq -v_d i_q, \tag{18}$$

since the PLL aligns the d-axis with the voltage phasor and therefore $v_q \simeq 0$. As a result, for positive v_d, a negative value of i_q corresponds to positive reactive power injection into the network.

When the PCC voltage remains above V_{S1}, the dynamic voltage support signal is zero and the q-axis current reference is determined by the normal reactive power or voltage control loop. When the voltage drops below V_{S1}, the normal PI controller is inhibited and the dynamic voltage support characteristic imposes a negative i_{q2} contribution, thereby increasing the reactive power injected by the converter. For very low voltages, below V_{S2}, this contribution is saturated at its maximum value. The final q-axis current reference is then limited according to the converter current capability, which is important because reactive voltage support competes with active current for the same converter current margin, as already explained with Equation (15).

In the reference operating point used in this work, the wind converter is initially operated in PQ mode with a prescribed active power and zero reactive power setpoint. Alternative voltage support strategies are investigated later in the sensitivity analyses.

4.5 Electrolyser model

The electrolyser is represented using the same GFL VSC structure as the wind generation unit. This choice reflects the fact that large electrolysis plants are connected to the AC network through power electronic conversion systems. In the RMS model used here, as already mentionned earlier, the detailed internal structure of the electrolyser is also not represented. The AC/DC conversion stages, the DC bus, the electrochemical stack dynamics, the hydrogen production process and the auxiliary systems are therefore neglected.

From the point of view of the AC network, the electrolyser is modelled as a controllable converter interfaced load. The same power sign convention is used as for the wind converter: a positive active power corresponds to an injection into the AC network, while a negative active power corresponds to power consumption from the network. Therefore, the active power setpoint of the electrolyser is negative, since the electrolyser consumes power from the network.

The active power behaviour of the electrolyser is not generated by a detailed process level controller. Instead, it is imposed mannually through predefined changes of the active power setpoint. These changes are introduced in the disturbance file and are used to emulate the delayed adaptation of the electrolyser consumption following a wind power variation. The delay and the ramp rate of this adaptation are key parameters of the dynamic study and are studied in Section 7.

The reactive power and voltage control capabilities of the electrolyser converter are modelled in the same way as for the wind converter. In the reference case, the electrolyser is initially operated in PQ mode with zero reactive power setpoint. Additional cases with voltage control or voltage support operation are considered in order to evaluate the influence of the converter voltage support strategy on the system response.

4.6 Synchronous condenser model

A synchronous condenser is connected close to the electrolyser bus in order to provide local voltage support and rotating inertia. It is represented by a synchronous machine model including the electrical dynamics of the machine and the associated excitation system. Since a synchronous condenser is not driven by a prime mover, it does not provide sustained active power in steady state. However, it can temporarily exchange active power with the network through the acceleration or deceleration of its rotor during transients.

The main role of the synchronous condenser in this study is to regulate voltage and provide reactive power support. Its excitation system includes an AVR, an exciter, a PSS (which is not activited in this work) and an over-excitation limiter (OEL) displayed in Figure 10.

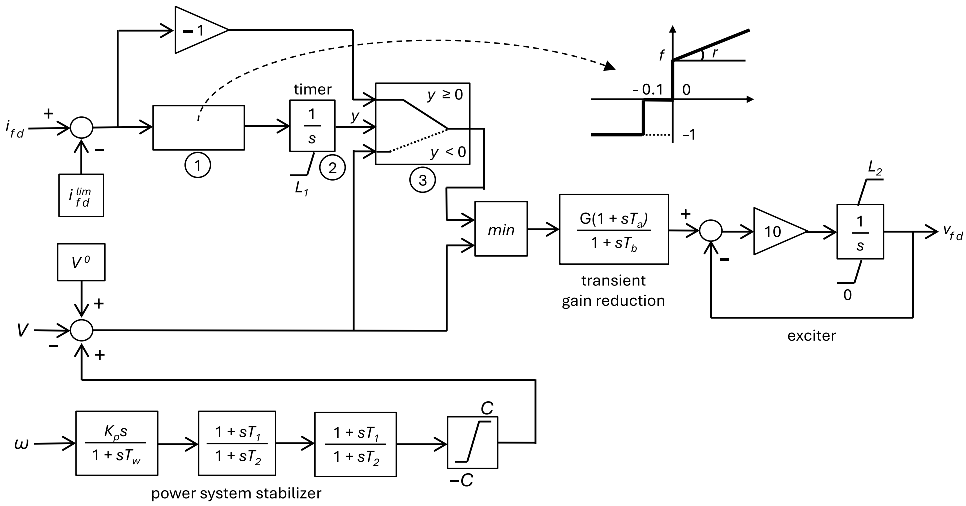

Figure 10: Excitation system, OEL, PSS and AVR of the synchronous condenser from [21]

The AVR compares the measured voltage at its PCC with its imposed voltage reference and acts on the field voltage v_{fd} of the machine. An increase in excitation increases the internal electromotive force and therefore improves the ability of the condenser to inject reactive power into the network. The exciter represents the dynamics between the AVR output and the field voltage applied to the synchronous machine.

In contrast, the OEL is a protection oriented controller. It monitors the field current and limits the excitation when the admissible field current is exceeded. If the OEL becomes active, the reactive power capability of the machine is reduced, which can affect the voltage profile of the system.

In the reference operating point, the synchronous condenser is operated in voltage control mode. Its voltage reference is chosen slightly above the nominal value in order to improve the local voltage profile and to make the condenser the main source of local reactive support, as explained in the next section.

4.7 Synchronous generator model

The external source is represented by a synchronous generator connected at the remote end of the network. This generator does not correspond to a specific physical unit of the industrial project. It is introduced in the reduced model to provide a voltage angle reference, active power balancing capability, rotating inertia and primary frequency support. It allows to have a more realistic representation of the frequency response of the system, which is important for the evaluation of the impact of different converter control strategies on frequency stability, because without it, the frequency depends only on the kinetic energy of the synchronous condenser and on the active power balance of GFL VSCs.

The synchronous generator is represented by almost the same type of synchronous machine model as the synchronous condenser, but it is also equipped with a torque controller. Despite its excitation system also includes an AVR, an exciter, a PSS (turned off aswell) and an OEL, the configuration is slightly different from the synchronous condenser's one, as shown in Figure 11.

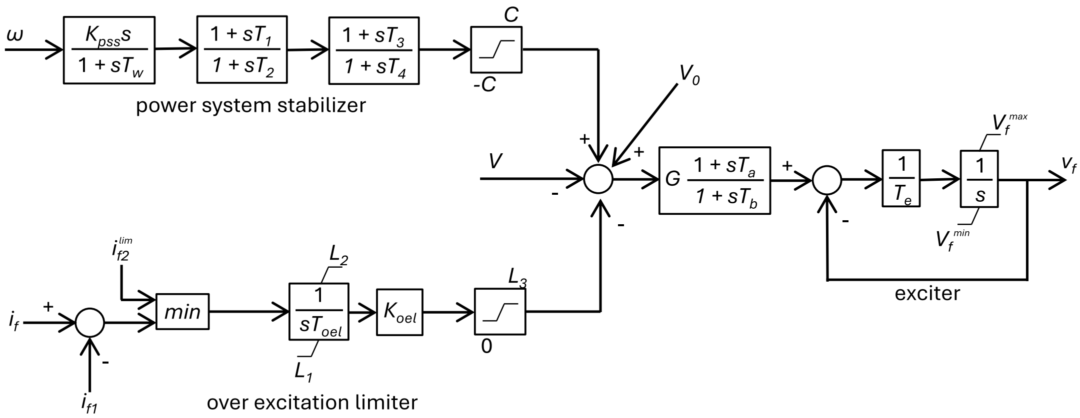

Figure 11: Excitation system, AVR, PSS and OEL of the external synchronous generator from [40].

The AVR regulates the generator terminal voltage by modifying the field voltage. The OEL limits the excitation when the field current becomes too high, while the PSS can be used to improve the damping of electromechanical oscillations. The same comments as for the synchronous condenser apply here, but the impact of the generator excitation system is more global because the generator also contributes to the active power balance of the islanded system.

The torque controller is shown in Figure 12. It represents the governor and turbine dynamics of the external synchronous source. Its input is related to the rotor speed deviation, and its output is the mechanical torque applied to the generator shaft. When a temporary active power imbalance occurs, the rotor speed changes and the torque controller adjusts the mechanical power in order to oppose the frequency deviation.

This model is therefore responsible for the sustained active power response of the

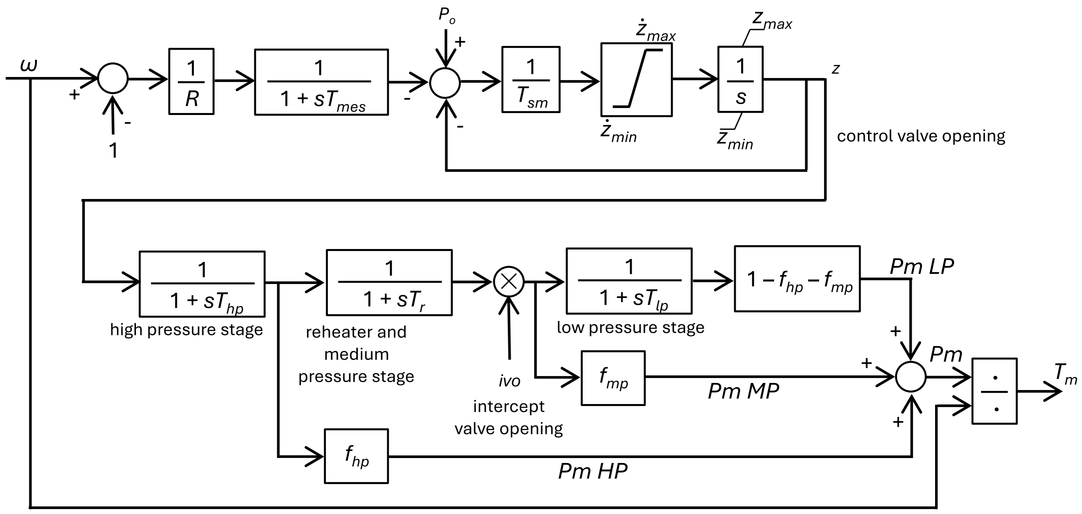

Figure 12: Torque controller of the external synchronous generator from [40].

reduced system. During the first instants following a disturbance, the imbalance is mainly absorbed by the kinetic energy of the synchronous machines. At a slower time scale, the torque controller modifies the mechanical torque of the external generator and contributes to frequency stabilisation.

5 Inital steady state operating point and dynamic study framework

To initiate the dynamic simulations of the power system, a PFC must first be performed. As noted earlier, the powerflow is solved automatically by STEPPS. The result of the PFC is then used by the solver RAMSES for the dynamic simulation as a first operating point. During dynamic simulations, the steady state operating point corresponds to a network operating without discrete events or disturbances, when all variables converge to constant values. However, the powerflow solution is not necessarily the same as the steady state solution, since it includes excitation systems, limiters and converter control loops.

5.1 Definition of the reference operating point

5.1.1 Powerflow assumptions and balancing principle

For the PFC, the generator is defined as the slack bus. It sets the voltage angle reference and compensates for the active power mismatch between losses, production, and consumption. The VSCs are operated in reactive power control mode and are therefore represented as PQ buses. At this stage, they do not provide any reactive power support, since their reactive power setpoints are set to zero. Their active powers are set to 500 MW and -500 MW. The synchronous condenser is operated in voltage control mode, with its active power set to zero since it cannot provide active power. It is therefore represented as a PV bus. The reactive power supply is mainly ensured by the synchronous condenser and, if necessary, by the slack generator.

5.1.2 Refinement of the reference operating point

Initially, the network design choices did not lead to a satisfactory normal operating point. Indeed, as seen in the Figure 13 the external synchronous generator connected to the slack bus was too weak to provide the reactive support required by the network at nominal conditions. As a result, although the PFC converged, the following no disturbance dynamic simulation showed an activation of the OEL of the synchronous generator. This activation led to a redistribution of reactive power, mainly toward the synchronous condenser, and to a new long term equilibrium. The system remained synchronized, with bounded relative angles and rotor speeds converging close to nominal frequency, but this operating point was not retained as reference since a limiter was already active in normal operation. The rating of this external synchronous generator was increased so that its excitation system remained within admissible limits at nominal operating conditions.

After the increase of generator rating, the resulting bus voltages remained within acceptable operating ranges, but were still slightly below the nominal 1 per unit profile at several buses. In order to define a more robust reference operating point before the dynamic simulations, the voltage setpoint of the synchronous condenser was increased from 1.00 to 1.01 pu. This adjustment brought the bus voltages closer to nominal values and improved the sharing of reactive power support. The corresponding voltage magnitudes are reported in Table 4.

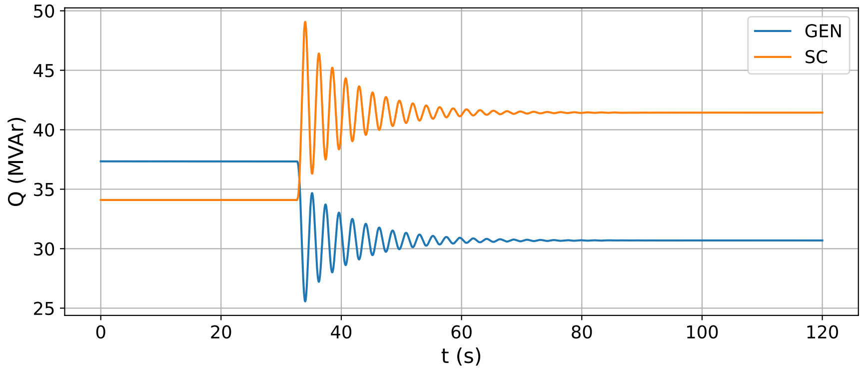

Figure 13: Reactive powers of the synchronous generator and synchronous condenser during a no disturbance simulation.

Table 4: Comparison of bus voltage magnitudes for two synchronous condenser voltage setpoints.

Bus	$\lvert V \rvert$ **for** $V_{\text{imp}} = 1.00$ **pu**	$\lvert V \rvert$ **for** $V_{\text{imp}} = 1.01$ **pu**
1	1.000	1.000
2	0.987	0.991
4	0.983	0.988
5	1.000	1.010
6	0.984	0.989

5.1.3 Active and reactive power dispatchs at PFC and initial steady state

The results of the PFC are presented in the Figure 14. The synchronous machines provides reactive power support, and also a small amount of active power in the case of the generator. The results of voltage magnitudes and angles are given in the Table 5. As expected, the angles are larger at buses for which the active power is produced and consumed.

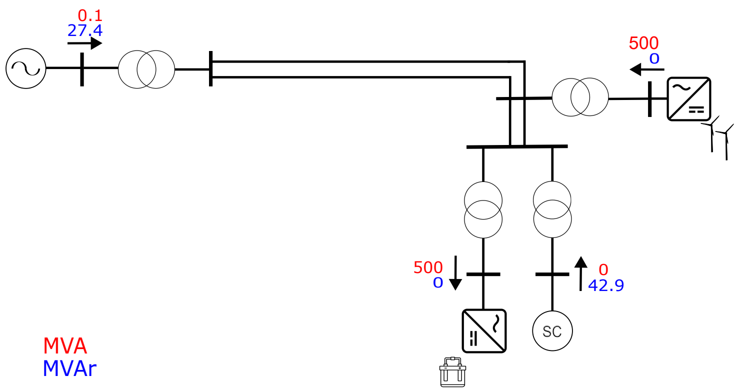

Figure 14: PFC results: active and reactive powers dispatch at each bus.

5.2 Dynamic scenario considered for the main study

The main dynamic scenario considered in this work is based on a temporary mismatch between wind generation and electrolyzer demand. A variation of wind power is first imposed on the system, and the electrolyzer consumption is then

Bus	$|V|$ (pu)	$\angle V$ (deg)
1	1.000	0.0000
11	0.993	-0.0010
2	0.991	0.0110
3	0.991	-0.0253
4	0.988	-4.4152
5	1.010	-0.0253
6	0.989	4.1400

Table 5: PFC results : Bus voltage magnitudes and angles

adjusted after a certain delay in order to restore the power balance. This sequence is used as the reference dynamic pattern for the simulations presented in the following chapters.

5.2.1 Initial equilibrium between wind production and electrolyzer demand

At the start of each simulation, the system is in a balanced operating condition as detailed in the previous sections, in which wind generation and electrolyzer demand are of comparable magnitude. This reference pre disturbance state is chosen so that the transient response mainly reflects the temporary mismatch created by the wind power change and the delayed load adaptation.

5.2.2 Wind power variation as the initiating event

The objective of this network is to produce hydrogen by converting wind energy. To maximise hydrogen production, the electrical consumption of the electrolyser should follow the available electrical power generation. However, wind is an inherently variable resource, leading to fluctuations in the power produced by the wind generation unit. Consequently, apart from faults or other grid related incidents, wind power variations constitute the main source of disturbances in the considered network. These variations may result from changes in wind speed or wind direction.

5.2.3 Delayed adaptation of electrolyzer consumption

To follow the variations of wind power, the electrolyser needs to adapt its consumption. However, this adaptation is not instantaneous, it is subject to a delay due to the control system and the physical processes involved in the electrolysis. This delay leads to transient imbalances between production and consumption, which can affect the stability of the network. However, in STEPPS, the VSC model doesn't have an active power control loop that would adjust its active power setpoint in function of the frequency deviation. It is a fixed parameter imposed at the beginning of the simulation. Indeed, a disturbance file must be provided as an input to STEPSS, allowing the active power setpoints of both VSCs to be manually modified. The modification is defined by three parameters:

- The variation of the setpoint in percentage of the VSC nominal power ΔP_{H_2} : it gives the amplitude of the ramp, i.e the difference between the initial setpoint and the new one after the ramp.

- The time t_{H_2} at which begins the variation, it gives the delay of reaction of the electrolyser : $\Delta T = t_w - t_{H_2}$, with t_w the time at which the wind power variation begins.

- The duration of the ramp t_{s,H_2}, which is linked to the slope of the ramp: $\alpha_{H_2} = \frac{\Delta P_{H_2}}{t_{s,H_2}}$ in $[\frac{\text{MW}}{\text{s}}]$.

The goal is to simulate the role of a controller which adjusts its active power setpoint of the electrolyser to follow the production. It is done by modifying manually the setpoints of the wind and electrolyser converters beforehand.

5.2.4 Sequence of events and main simulation parameters

The simulated sequence contains three successive phases: an initial steady period, a wind power ramp (up or down), and a delayed adaptation of the electrolyzer demand. The case is fully characterised by the initial power, the size of the ramp, the wind ramp slope, the electrolyzer reaction delay, and the slope of the electrolyzer demand variation. A schematic illustration of the two active power trajectories is provided in Figure 15. These quantities are later varied in the sensitivity analysis.

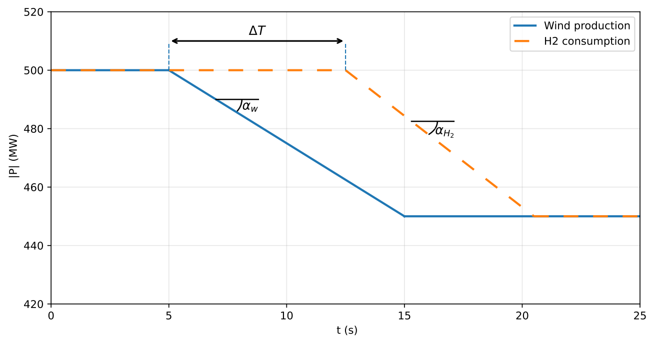

Figure 15: Exemple of active power trajectories : wind power ramp down followed by a delayed ramp down of the electrolyzer demand.

5.3 Performance indicators and assessment criteria

In this section, the main indicators used to assess the dynamic response of the system throughout the simulations are presented.

5.3.1 Frequency related indicators

The frequency analysis provides a global view of the active power imbalances in the system. The rotor speeds of the synchronous machines are available as output data. Therefore, the analysis focuses on the speed responses of the synchronous generator and the synchronous condenser. The indicators used for this assessment are:

- Frequency nadir: to quantify the minimum frequency reached during the transient. It allows to compare the severity of the different simulations.

- Frequency peak: to quantify the maximum frequency reached during the transient.

- RoCoF: related to the frequency nadir and peak, it gives the speed at which the frequency deviates.

- Final frequency deviation: to assess at which frequency the system stabilises after the transient.

- Times of occurrence of the frequency extrema and of the maximum RoCoF: to identify when the most critical deviations occur. The convergence time is also used to assess how quickly the frequency stabilises.

5.3.2 Voltage related indicators

Voltage indicators are used to assess the adequacy of reactive power support during and after the transient. It allows to quantify the severity of a transient. A case is considered more severe when it produces deeper voltage dips, larger post disturbance voltage deviations, or slower voltage recovery. They are measured at each bus. The indicators that will be used are :

- Voltage nadir : to quantify the amplitude of the voltage deviation.

- Voltage peak : to quantify the amplitude of the voltage deviation.

- Voltage deviation at the end of the transient.

- Times of occurrence of the voltage extrema: to identify when the most critical deviations occur. The convergence time is also used to assess how quickly the voltage stabilises.

5.3.3 Additional indicators

Other relevant parameters are also considered, as they provide insight into the contribution of each supporting component of the system during the transient:

- Mean active and reactive powers of the synchronous machines during the simulation: to represent the net energy contribution of each machine over the whole simulation.

- Maximum apparent power reached by the synchronous machines during the simulation: to provide a first indication of the minimum rating required for the machines to support the system without reaching their limits.

- Extrema and final values of the relative rotor angle between the two synchronous machines.

5.4 Sensitivity analysis methodology

In Section 7, the results of several sensitivity analyses are presented. These analyses are performed by varying one parameter at a time among the following: the wind ramp size, the response delay of the electrolyser, the slope of the electrolyser ramp, the transformer reactance in front of the generator, and the inertia of the synchronous machines.

The impact of these parameters on the dynamic response of the system is assessed using the indicators presented in the previous section. These indicators are then plotted as a function of the varied parameter.

An additional parametric study is also carried out by repeating the wind ramp size sensitivity analysis, in order to compare four different cases corresponding to different control modes of the wind and electrolyser VSCs.

6 Time-domain analysis of dynamic simulations

6.1 Response in an instable situation after power ramp

Starting from the PFC and initial steady state described in sections 5.1, a downward ramp of the wind power is simulated, without any adaptation of the electrolyzer demand in a first place. The parameters of the simulated event are given in Table 6, $t_w(s)$ is the starting time of the wind ramp, ΔT is the delay between the start of the wind ramp and the start of the electrolyzer ramp which will be used in the next sections only, α_w and α_{H_2} are the slopes of the wind and electrolyzer ramps respectively (in percent of the nominal power of the VSC per second), and t_{end} is the end time of the simulation. The system response after a 20% reduction of wind production in two seconds is shown on Figure 16.

Table 6: Parameters of the simulated downward wind power variation

$\Delta P_w(\%)$	$\Delta P_{H_2}(\%)$	$t_w(s)$	$\Delta T(s)$	$\alpha_w(\%/s)$	$\alpha_{H_2}(\%/s)$	$t_{end}(s)$
-20.0	0.0	5.0	/	-10.0	/	65.0

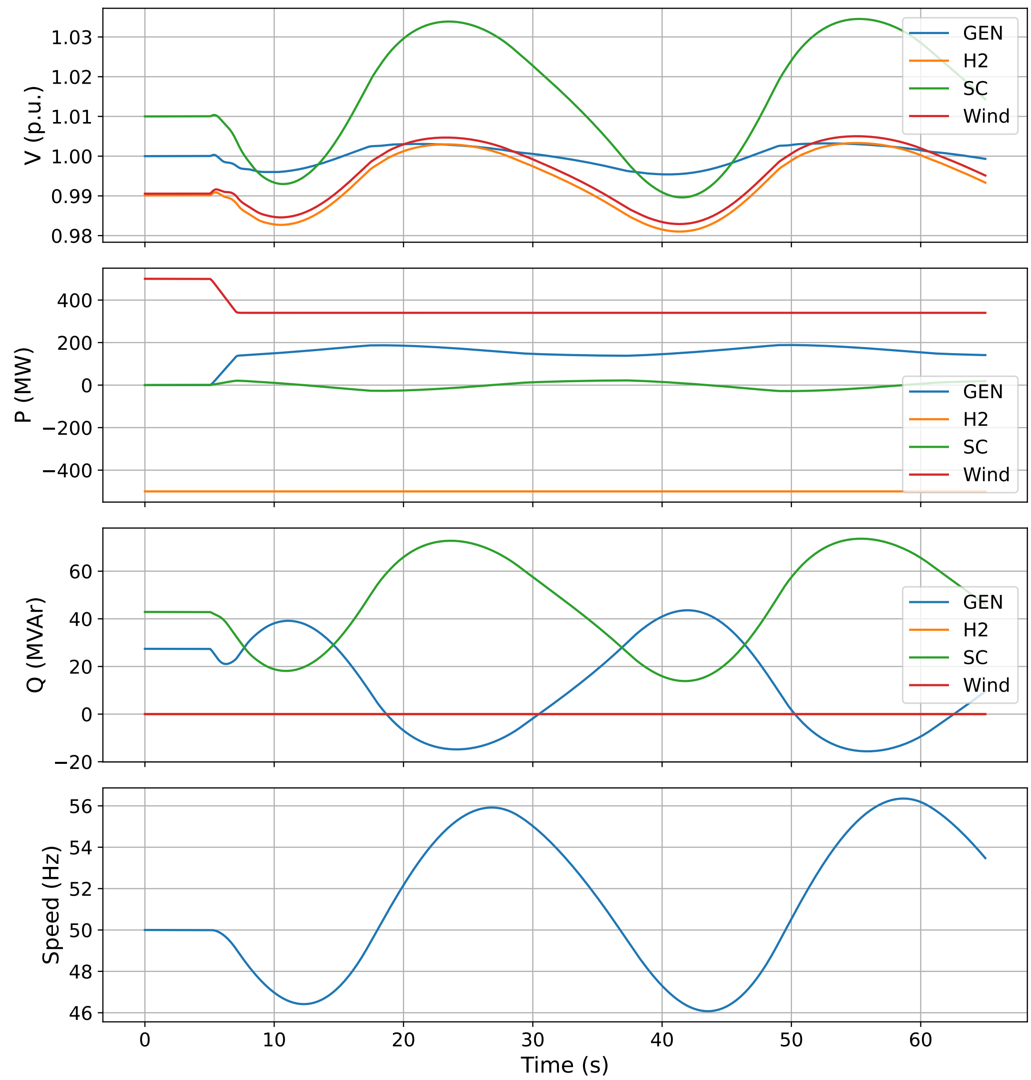

Figure 16: Responses of the main system parameters when subjected to a -20% wind power ramp without any adaptation of the electrolyzer demand.

An unbalance is created because the load consumes constant active power whereas the wind decreases. The only devices able to manage the mismatch of active power are the synchronous machines present in the system. Their first automatic response is to release the kinetic energy stored in their rotors to generate more active power. Consequently, their rotor speed decreases and the mechanical torque controller of the synchronous generator sees in input the frequency deviation. This frequency decrease can be observed on the last subfigure of Figure 16 at the fifth second. This makes the generator increase its mechanical torque to try to restore the frequency. But it does not happen correctly, instead, an oscillation of the frequency is observed with an amplitude of 10%, which is not acceptable. In a real system, this would lead to the activation of protection devices and to a blackout. In this work, the simulations were forced to continue allowing the observation of the behaviour of the instable system.

The oscillations in frequency are not damped and according to the swing equation 3, the generator needs either to adjust its electrical torque with the PSS, or to adjust mechanical torque with the turbine and governor controls. In this case, the PSS was not adapted to such a large disturbance, trying to tune it didn't lead to any results in active power adaptation. Therefore, the only way for the system to try to restore its frequency was to improve the adjustment of the mechanical torque with the turbine and governor control.

On Figure 17, it is observed that the mechanical torque control of the generator is way to slow to react to the frequency deviation. Indeed, it can be seen on precise points of the trajectory, for instance when the torque increases back the frequency to 1 pu at the 18th second, it takes then 10 seconds to decreases its torque at the same value of the electrical torque. It is because of the turbine and governor large time constants, making the mechanical torque response very slow, but also because of the rate limiters of the valve.

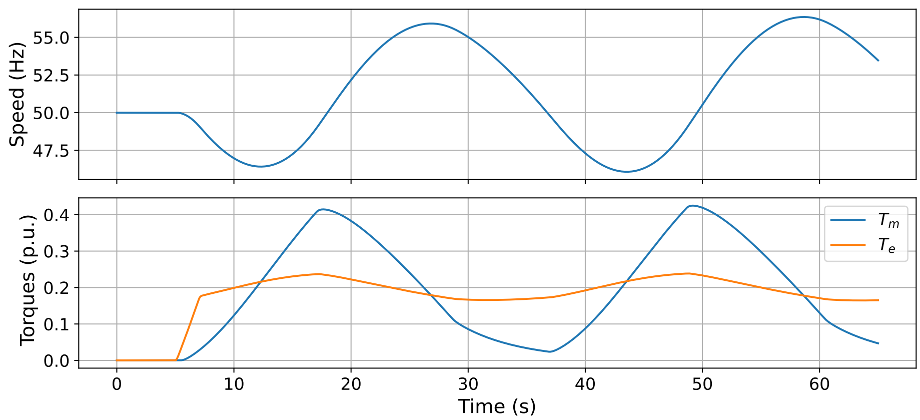

Figure 17: Mechanical and electrical torques trajectory of the synchronous generator compared to frequency during the instable ramp down scenario.

Indeed, the governor was reaching its limit with the minimum and maximum rate limiters of the valv opening, so being permanently saturated and leading to unsufficient mechanical torque adaptation. Figure 18 reveals this saturation with the constant slope variations of the valve opening, which are indeed the limits set in the torque controller : $\dot{z}_{max} = 0.05$(p.u./s) and $\dot{z}_{min} = -0.05$(p.u./s). These parameters are changed in the next sections.

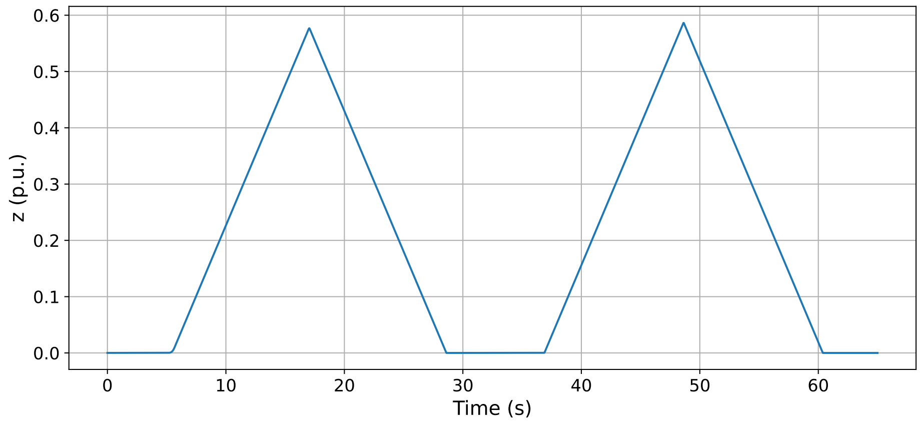

Figure 18: Valve opening trajectory during the instable ramp down scenario.

Concerning active power, its variations led to fluctuations in the voltage profile, which are observed on the first subfigure of Figure 16. It is due to the voltage drops that depends on power flows. This is why on the third subfigure of Figure 16, the reactive powers of the synchronous machines are also oscillating, trying to support the voltages at their PCCs. It is a consequence of the frequency instability.

6.1.1 Impact of increasing the rate limiter of the valv on the system response

The same simulation is performed, but now a larger rate limiter of the valve opening is chosen, i.e. $\dot{z}_{max} = 0.2$(p.u./s) and $\dot{z}_{min} = -0.2$(p.u./s). This allows the turbine/governor to react faster to the frequency deviation and therefore to restore the stability of the system. The results are shown on Figure 19. The frequency nadir is now 48.75 Hz, which is still large but acceptable, and the frequency oscillations are damped in 20 seconds. The voltage variations are also less important than in the previous case, and they are also damped in 20 seconds.

However, the frequency converges to a value slightly below the nominal one, it is inevitable as the torque controller has not secondary control to restore the frequency to its nominal value.

On Figure 20, it can be observed that the mechanical torque of the generator is now able to follow the electrical torque much closer. Figure 21 confirms that the valv opening trajectory is still close or at saturation at the beginning of the perturbation, confirming it was a limiting factor in the previous case, and allowing now a faster response of the turbine and governor.

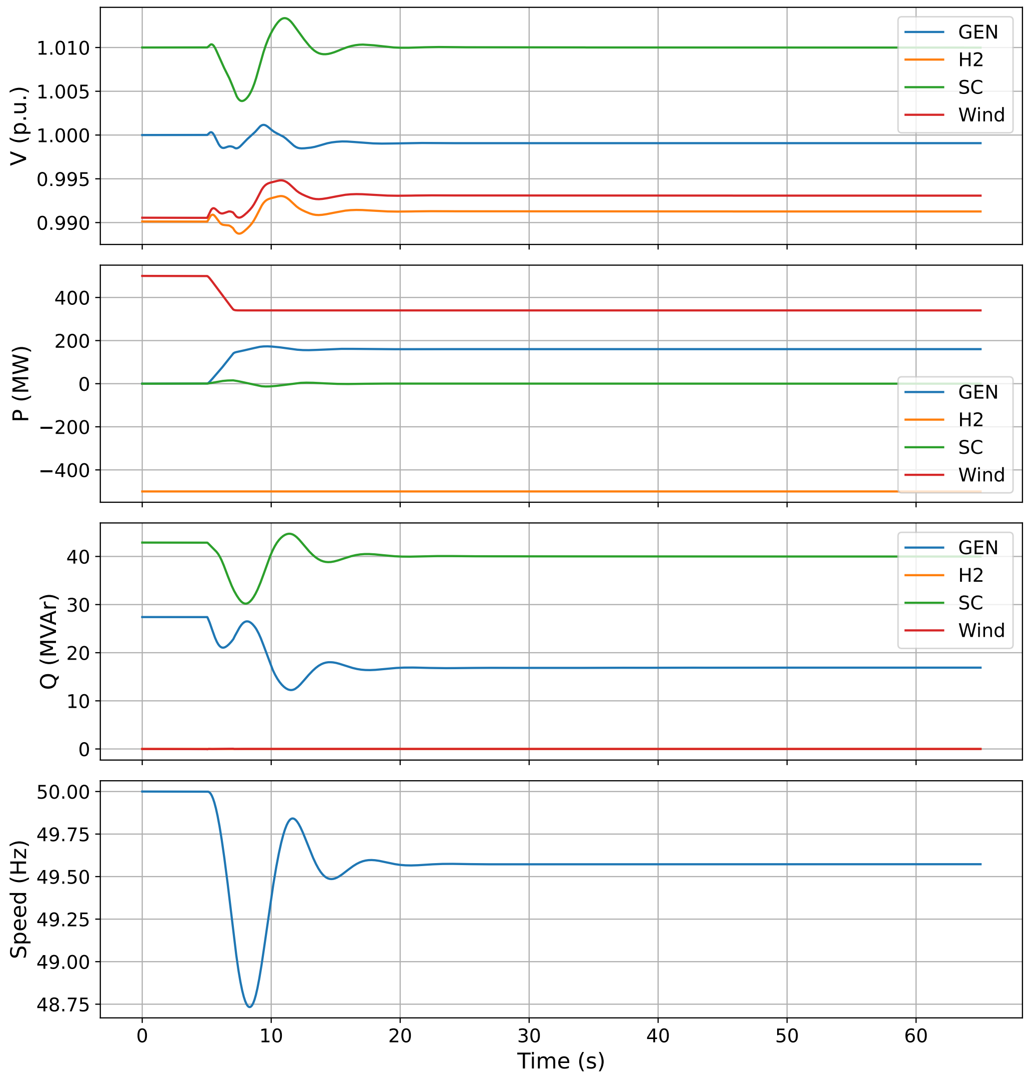

Figure 19: Responses of the main system parameters when subjected to a -20% wind power ramp without any adaptation of the electrolyzer demand, with increased rate limiter of the valve opening.

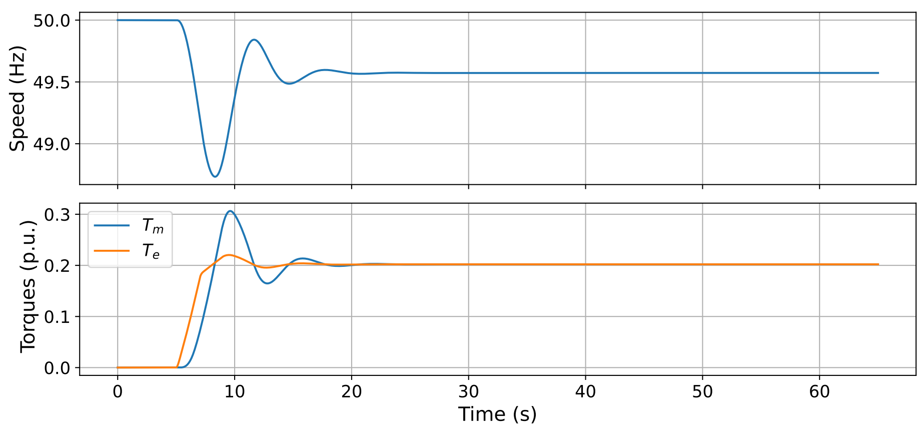

Figure 20: Mechanical and electrical torques trajectory of the synchronous generator compared to frequency during the stable ramp down scenario.

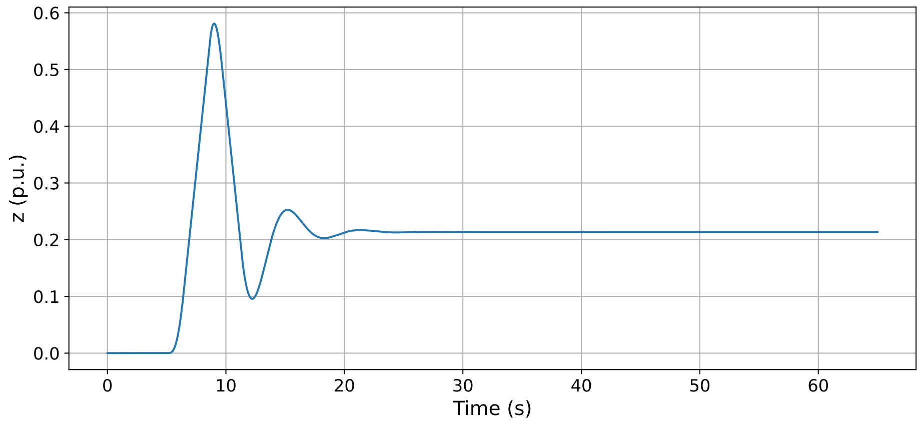

Figure 21: Valve opening trajectory during the stable ramp down scenario.

6.2 Response to a downward wind power variation with electrolyzer reaction

6.2.1 Description of the simulated event

Another dynamic simulation is performed, starting from the same PFC and initial steady state. A downward ramp of the wind power is still applied, but now followed with a delayed adaptation of the electrolyzer demand as explained in section 5.2. The parameters of the simulated event are given in Table 7. The system is subjected to a loss of 13% of wind production in five seconds, and the electrolyzer reacts within one second at the same speed.

Table 7: Parameters of the simulated downward wind power variation

$\Delta P_w(\%)$	$\Delta P_{H_2}(\%)$	$t_w(s)$	$\Delta T(s)$	$\alpha_w(\%/s)$	$\alpha_{H_2}(\%/s)$	$t_{end}(s)$
-13.0	13.0	10.0	1.0	-2.6	2.6	65.0

6.2.2 Time domain interpretation from the plots

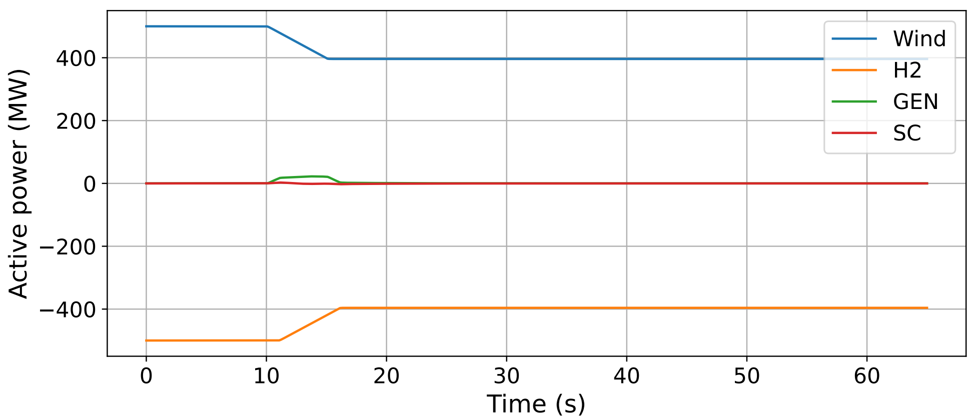

Figure 22: Productions and consumptions trajectories of active power.

As seen in Figure 22, the active power mismatch caused by the delayed reaction of the electrolyzer is mainly compensated by a temporary production of the external generator. As in the previous section, this mismatch is initially supported by the inertia of the rotating masses, causing the rotors to decelerate, as observed in Figure 23. The governor then increases the valve opening in response to the decrease in rotor speed below its nominal value, which increases the mechanical power delivered by the turbine. While the generator is still increasing its mechanical input power, the VSC of the electrolyzer starts reducing its active power consumption with the same slope as the wind power decrease, thereby also contributing to the recovery of the frequency drop. When the electrolyzer has completed its active power reduction, the generator takes some time to react to this second abrupt change in active power balance and temporarily produces a surplus of mechanical power, see Figure 24. This accelerates the rotor and the frequency reaches a maximum value slightly below 1.01 p.u.

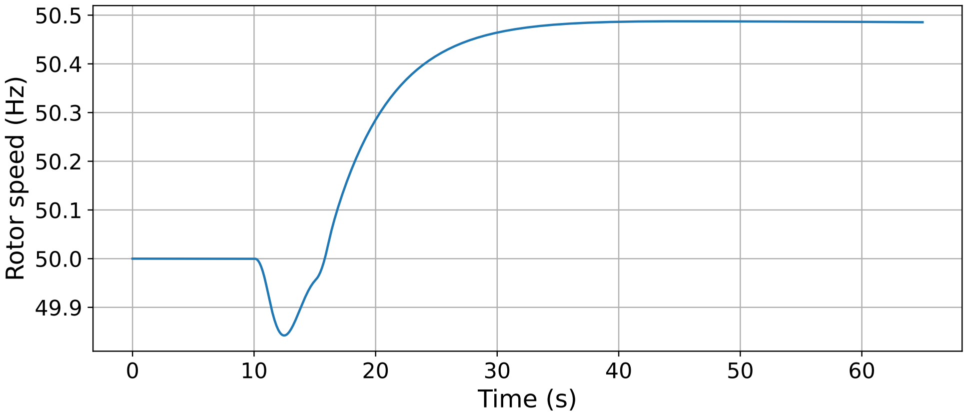

Figure 23: Rotor speed of the synchronous generator.

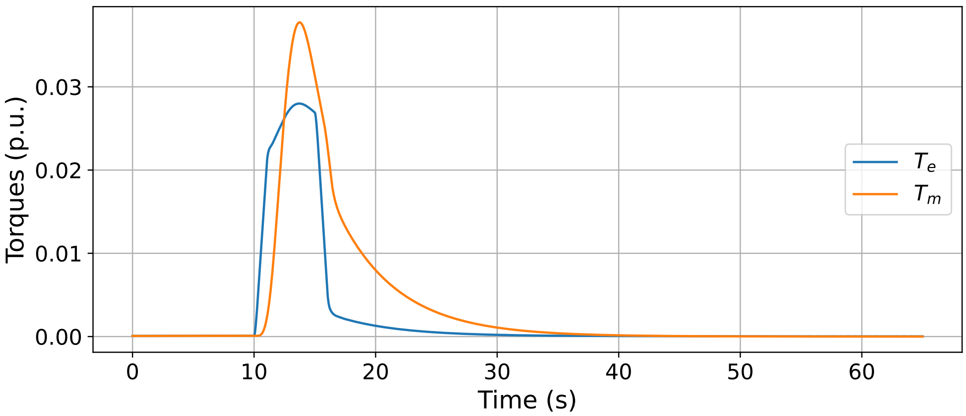

Figure 24: Electromecanical torque and mechanical torque of the synchronous generator.

Once both VSCs have completed their active power variations, the post ramp active power imbalance is almost removed, since the reduction in electrolyzer consumption nearly compensates the wind power decrease. The synchronous generator is therefore no longer required to provide a significant active power support. Nevertheless, a very small residual imbalance remains after the electrolyzer ramp: the generator electrical power is slightly larger than the mechanical power delivered by the turbine, both being only of the order of a few kW. This weak decelerating torque slowly dissipates the excess kinetic energy stored during the frequency overshoot, over a very large period. Then, as the rotor speed reaches 1 p.u., the governor action decreases and the mechanical power slightly increases until it balances the its electrical output power again.

Concerning the synchronous condenser, as mentionned its active power does not stay at zero during the transient, it first gives and then absorbs active power thanks to its inertia with power magnitude in the range of 2.5 MW.

Regarding the voltage response and reactive power support, the decrease in active power transfer through the network reduces the currents flowing through the lines and transformers. As a result, the voltage drops across the series impedances decrease, together with the active power losses and the reactive power absorbed by the network impedances. The voltage profile therefore rises after the disturbance, as shown in Figure 25. This effect is visible at most buses. It is less pronounced at Bus 1, which is the terminal bus of the external synchronous generator and is therefore directly affected by its voltage regulation.

The synchronous machines react to this voltage increase through their excitation systems. Since the terminal voltages tend to rise, the AVRs reduce the excitation and, consequently, the reactive power injected by the machines. This is clearly visible for the external generator, whose reactive power decreases strongly and becomes close to zero after the disturbance. The synchronous condenser also reduces its reactive power injection, but it remains the main source of reactive support in the final operating point. This is consistent with the voltage control settings of the two machines: the generator is regulated around $V_{\mathrm{imp}} = 1.00$ p.u., whereas the synchronous condenser is regulated around $V_{\mathrm{imp}} = 1.01$ p.u. Because of this higher voltage target, the synchronous condenser naturally maintains a larger reactive power contribution.

The synchronous machines react to this voltage increase through their excitation systems. Since the terminal voltages tend to rise, the AVRs reduce the excitation and, consequently, the reactive power injected by the machines. This effect is particularly pronounced for the external generator, whose reactive power decreases strongly and becomes close to zero after the disturbance. The synchronous condenser also reduces its reactive power injection, but remains the main source of reactive support in the final operating point. This behaviour is not only determined by the voltage references, but also by the electrical location of the machines and by the network impedances and the gain of the excitation. Nevertheless, the higher voltage reference of the synchronous condenser, $V_{\mathrm{imp}} = 1.01$ p.u. compared with 1.00 p.u. for the generator, contributes to maintaining a larger reactive power contribution from the condenser.

The final controlled voltages do not exactly return to their imposed reference values. This behaviour is not necessarily a numerical issue. It results from the finite-gain structure of the AVR/exciter model used for the synchronous machines (see Appendix A). In steady state, a change in field voltage can be associated with a small residual voltage error, because the voltage error is not eliminated by a pure integral action in the AVR loop. The machines therefore reduce their excitation after the voltage rise, but the reduction is not sufficient to force the terminal voltages exactly back to their reference values. The system consequently settles to a new steady-state voltage profile, slightly different from the initial one.

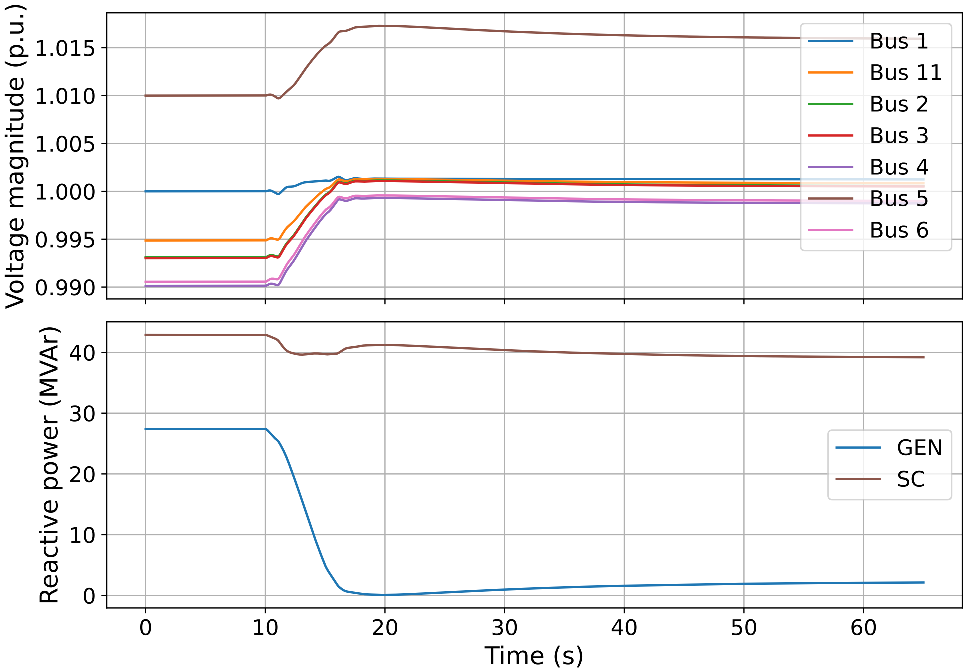

Figure 25: Comparison of the voltages at each bus and the reactive power responses of both synchronous machines during the ramp down scenario.

6.2.3 Indicators analysis

The main indicators extracted for this case are summarised in Table 8. Concerning the frequency response, the rotor speed of the external generator reaches a nadir of 49.84 Hz at 12.47 s, confirming that the temporary active power deficit created by the wind ramp down is initially absorbed by the synchronous inertia of the system. The RoCoF reaches a minimum value of -0.119 Hz/s at 11.12 s and a maximum value of 0.111 Hz/s at 16.09 s. Later on, the frequency overshoots above nominal value and reaches a zenith of 50.49 Hz at 46.24 s. Over the simulated time window, the estimated final frequency remains to this value, at 50.49 Hz

Regarding the voltage response, the deepest voltage dip is observed at bus 4, at the load, where the voltage reaches 0.990 p.u. at 10.02 s. The highest voltage peak is observed at the bus of the synchronous condenser, bus 5, with a value of 1.017 p.u. at 20.13 s. Although the transient leads to visible voltage variations, all bus voltages remain within the admissible [0.95–1.05] p.u. range during the whole simulation. The slowest voltage settling behaviour is also observed at bus 5, with a settling time of 52.83 s.

The power exchange indicators confirm that the temporary active power mismatch is mainly compensated by the external generator, whose active power output reaches 22.35 MW during the transient. The synchronous condenser also contributes through its stored kinetic energy, with a short active power excursion between +2.85 MW and -2.71 MW. The maximum apparent powers reached by the external generator and the synchronous condenser are 27.82 MVA and 47.18 MVA, respectively. The relative rotor angle between the two synchronous machines remains bounded, with a maximum value of 3.17° and a final estimated value close to its initial value. Overall, the extracted indicators show that the system remains dynamically stable for the considered operating conditions.

These indicators are used in the next section to evaluate the impact of sensitivity parameters on the system response and stability.

Table 8: Main performance indicators for the reference ramp down case.

Category	**Indicator**	**Value**	**Time / Location**
Freq	Frequency nadir (gen)	49.84 Hz	12.47 s
Freq	Frequency zenith (gen)	50.49 Hz.	46.24 s
Freq	Final estimated frequency (gen)	50.49 Hz	/
Freq	Min RoCoF (gen)	-0.119 Hz/s	11.12 s
Freq	Max RoCoF (gen)	0.111 Hz/s	16.09 s
V	Lowest voltage nadir	0.990 p.u.	Bus 4, 10.02 s
V	Highest voltage peak	1.017 p.u.	Bus 5, 20.13 s
V	Longest settling time	52.83 s	Bus 5
V	Time outside 0.95–1.05 p.u.	0.00 s	All buses
P	Peak active power of external generator	22.35 MW	13.76 s
P	Max. active power of SC	+2.85 MW	11.04 s
P	Min. active power of SC	-2.71 MW	16.02 s
Q	Max. reactive power of generator	23.57 MVAr	10.02 s
Q	Min. reactive power of generator	3.77 MVAr	16.42 s
Q	Max. reactive power of SC	47.18 MVAr	10.02 s
Q	Min. reactive power of SC	34.35 MVAr	64.94 s
S	Max. apparent power of generator	27.82 MVA	11.19 s
S	Max. apparent power of SC	47.18 MVA	10.02 s
Angle	Min relative rotor angle	0.028°	65.00 s
Angle	Max relative rotor angle	3.169°	14.42 s
Angle	Final relative rotor angle	0.028°	/

7 Parametric sensitivity analysis of the wind electrolyser system

7.1 Sensitivity to the wind power variation

In this section, a simulation similar to the one presented in the previous section is repeated several times for different values of the wind ramp size ΔP_w. The wind ramp size is varied from -5% to -60% of the nominal wind power of 750 MW, with a step of 5%. The initial operating point always corresponds to 500 MW of wind production and electrolyser consumption. The electrolyser ramp size is adapted accordingly to maintain the same relative variation, i.e. $\Delta P_{H_2} = -\Delta P_w$. The other parameters are kept constant throughout this section and are given in Table 9.

Table 9: Constant parameters of the simulated downward wind power variation.

$t_w(s)$	$\Delta T(s)$	$\alpha_w(\%/s)$	$\alpha_{H_2}(\%/s)$	$t_{end}(s)$
5.0	1.0	-10.0	10.0	65.0

The most relevant indicators for this analysis are extracted and plotted as a function of the wind ramp size. The final voltage magnitudes at the end of the simulation are shown in Figure 26, while the voltage peaks during the transient are shown in Figure 27. As expected, the voltage magnitudes increase with the magnitude of the negative wind ramp, due to the reduction of active power transfer through the lines and transformers, and the associated losses. No unacceptable voltage excursions are observed, even for large ramp sizes.

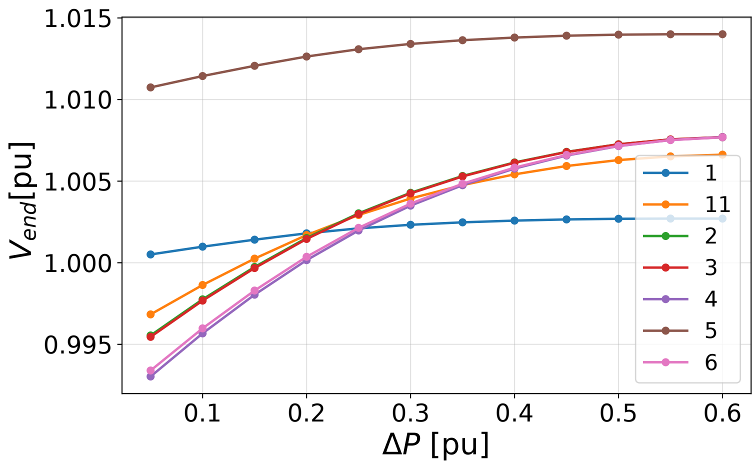

Figure 26: Final voltage magnitudes at each bus of the network in function of the downward wind ramp size ΔP_w.

Additionaly on Figure 27, it can be observed that the voltage peaks at buses 1 and 5 do not keep increasing for wind ramp sizes larger than approximately -30%, unlike the other buses. This can be explained by the fact that these buses are directly connected to the synchronous machines, whose excitation systems regulate the local voltage through reactive power adjustments. As a result, the changes in active and reactive power flows caused by larger wind ramps are partly compensated at these buses. Beyond this point, increasing the wind ramp size mainly leads to larger reactive power adjustments by the synchronous machines, rather than to a further increase of the local voltage peak. This also mitigates the increase in voltage peaks at the other buses, as reflected by the reduced slope of their curves for larger wind ramp sizes.

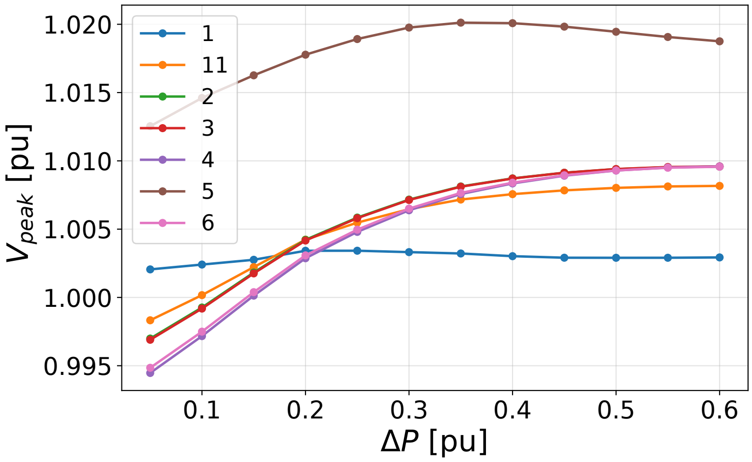

Figure 27: Voltage peaks at each bus of the network during the simulation in function of the downward wind ramp size ΔP_w.

The plot of the voltage nadirs is not shown here, see Annexe B. Indeed, it does not vary with the ramp size because the same initial dynamic response is observed at each iteration. For all ramp sizes, the minimum voltage at bus 1 occurs at the onset of the electrolyser VSC active power setpoint adjustment. Since this adjustment is performed with the same ramp rate in all cases, the mismatch of active power and the associated voltage transient are identical across the simulations. The synchronous machine controllers are therefore subjected to the same variations in frequency and voltage at this point and exhibit the same response time. As a result, the voltage nadir remains unchanged.

Figure 28 shows that the mean reactive power supplied by the synchronous machines decreases while the absolute ramp variation increases. This is due to the AVR of the synchronous machines. Indeed as the voltages at bus 1 and 5 are higher than the setpoint of the machines (1 p.u. for the generator and 1.01 for the synchronous condenser) as seen on Figures 26,27, the control loop of the AVR and exciter tends to decrease the voltage field setpoint of the machines, which reduces their reactive power injection. However, the voltage setpoints are not achieved, a steady state error is still present, it is due to the AVR and exciter structure of the synchronous machines, as explained earlier in section 6.2.2. It can be observed on Figure 28 that the mean reactive power supplied by the synchronous generator becomes negative for large ramp sizes. Indeed, the generator starts absorbing reactive power from the grid instead of supplying it, which is a consequence of the voltage increase at bus 1, but also caused by the synchronous condenser still generating reactive power.

Figure 29 shows that the mean active power supplied by the synchronous generator increases approximately linearly with the magnitude of the downward wind ramp. Since the ramp rates and the electrolyser response delay are kept constant in all simulations, increasing the downward ramp size mainly increases the duration

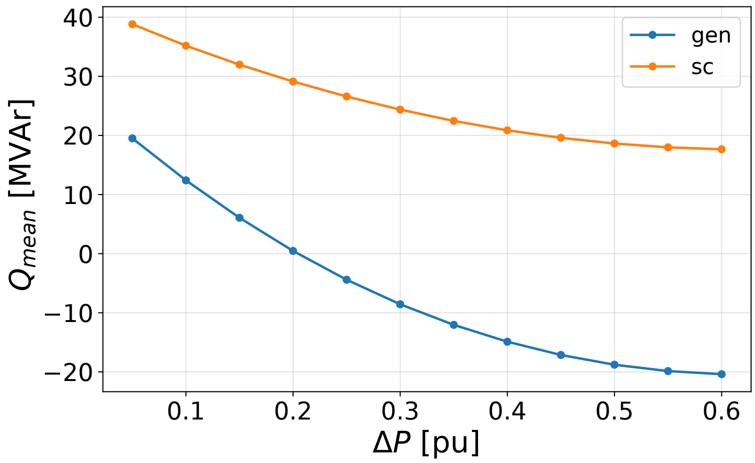

Figure 28: Mean reactive power exchanged by the synchronous machines as a function of the downward wind ramp size ΔP_w.

of the active power mismatch between wind generation and electrolyser demand. This mismatch is mainly compensated by the synchronous generator, and its corresponding compensation energy can be approximated as :

$$\begin{aligned} \Delta E_{\text{sync,gen}} &\approx \int_{t_0}^{t_{\text{end}}} \Big[|P_{H_2}(t)| - |P_w(t)| \Big] \, dt \\ &\approx \int_{t_w}^{t_{\text{end,ramp}}} \Big[|P_{H_2}(t)| - |P_w(t)| \Big] \, dt. \end{aligned} \tag{19}$$

This increase in compensation energy directly translates into a higher mean active power contribution of the synchronous generator.

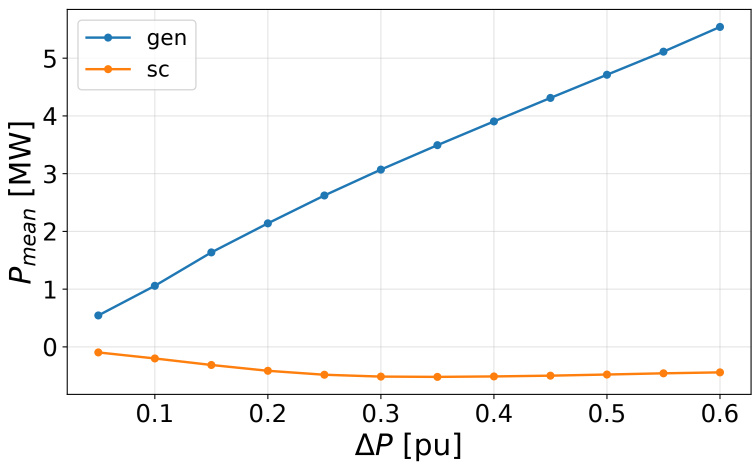

Figure 29: Mean active power exchanged by the synchronous machines as a function of the downward wind ramp size ΔP_w.

On Figures 30 and 60 in Appendix B, the main indicators of the frequency response are shown. On Figure 30, the frequency nadir decreases when the magnitude of the wind ramp increases, but this decrease remains constant for ramp sizes larger than approximately -15%. This can be explained by the fixed delay and ramp rate of the electrolyser response. For small wind ramps, such as -5% or -10%, the wind power ramp is completed before, or approximately when, the electrolyser starts to react. The resulting active power imbalance is therefore shorter and smaller. For larger ramps, the wind and electrolyser powers vary simultaneously after the electrolyser delay, with similar ramp rates and opposite signs. As a result, the maximum active power imbalance is mainly determined by the one-second delay between the two ramps, rather than by the total ramp size. Increasing the wind ramp size beyond this point mainly extends the duration of the imbalance, while the initial frequency trajectory remains almost unchanged.

The frequency zenith, which is identical to the final estimated frequency, first increases with the wind ramp size and then decreases for ramp magnitudes larger than approximately 35%. This non-linear behaviour is likely related to the interaction between the duration of the active power imbalance and the mechanical response of the synchronous generator. For moderate ramp sizes, the governor response leads to an overcompensation after the electrolyser power reduction, resulting in a higher frequency. For larger ramp sizes, the disturbance lasts longer and the governor and turbine dynamics have more time to react during the transient, so that the final frequency does not continue to increase.

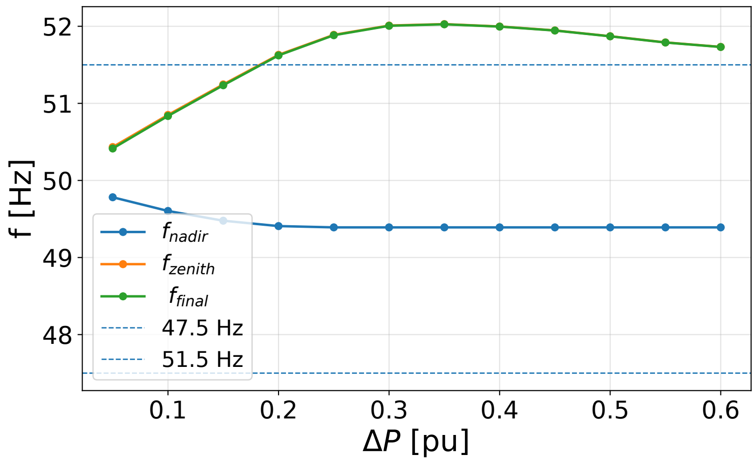

Figure 30: Final, zenith and nadir frequencies for different values of the downward wind ramp size ΔP_w.

The RoCoF results were also plotted, but they follow the same trend as the frequency nadir and zenith, for the same reasons. Therefore, the corresponding plot is shown in Appendix B.

Figure 31 shows the maximum apparent power reached by the synchronous machines during the simulation for each wind ramp size. The synchronous condenser reaches the same maximum apparent power in all cases, around 43 MVA. Since it exchanges almost no active power, its apparent power is mainly determined by its reactive power contribution. As the bus voltages increase from the beginning of the transient, the reactive power supplied by the synchronous condenser decreases. Therefore, its maximum apparent power is likely reached before the disturbance, which explains why it is almost independent of the wind ramp size.

In contrast, the maximum apparent power of the synchronous generator increases with the magnitude of the wind ramp, before reaching a plateau around 87 MVA. This apparent power depends on both active and reactive power, according to $S = \sqrt{P^2 + Q^2}$. The saturation of $S_{\max}$ is mainly due to the fact that the maximum active power mismatch is limited by the fixed delay and ramp rates of the wind and electrolyser responses, while the exact value of the peak also depends on the reactive power exchanged at that time.

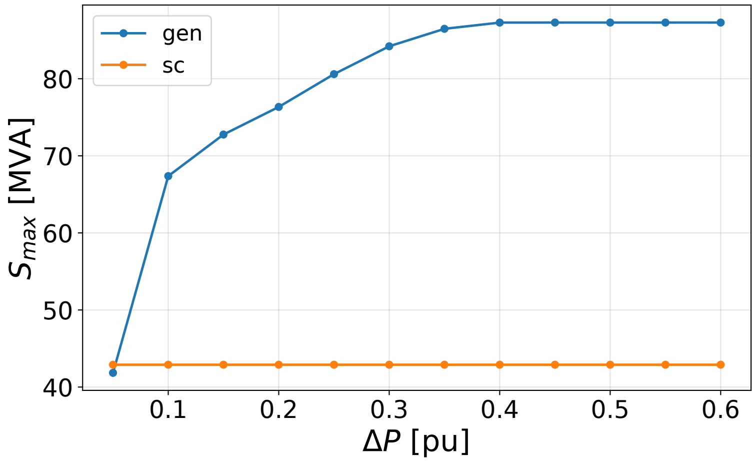

Figure 31: Maximum apparent power reached by the synchronous machines during the simulation for different values of the wind ramp size ΔP_w.

Figure 32 shows the extrema and final value of the relative rotor angle between the two synchronous machines for each wind ramp size. The final relative angle remains close to zero, which indicates that no significant permanent angular separation remains after the wind and electrolyser powers are rebalanced. The transient deviation arises because the two machines do not experience the same rotor-speed variations during the disturbance. The synchronous generator participates in compensating the temporary active power imbalance, whereas the synchronous condenser exchanges almost no active power and mainly contributes through its inertia. The resulting temporary speed difference between the machines leads to a relative angle deviation. As the wind ramp size increases, this transient angular excursion becomes larger, but it tends to saturate for the largest ramps because the maximum instantaneous active power mismatch is mainly imposed by the fixed delay and ramp rates of the wind and electrolyser responses.

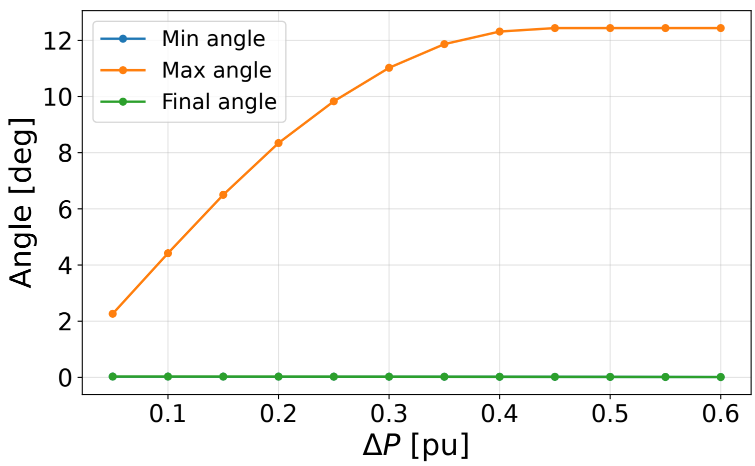

Figure 32: Max angle deviation between the rotors of the synchronous machines for different values of the downward wind ramp size ΔP_w.

7.2 Sensitivity to the electrolyser adaptation dynamics

7.2.1 Influence of the reaction delay

The same downward wind ramp is now simulated for different values of the reaction delay ΔT between the beginning of the wind power variation and the beginning of the electrolyser power variation. The delay is varied from 0 s to 14 s with a step of 1 s. The other parameters are kept unchanged throughout the simulations and are given in Table 10. The event starts at $t_w = 5$ s, with a constant wind power reduction of 20% of the nominal wind power occurring over 2 s.

Table 10: Constant parameters of the sensitivity analysis related to the electrolyser reaction delay.

$t_w(s)$	$\Delta P_w(pu)$	$\alpha_w(\%/s)$	$\alpha_{H_2}(\%/s)$	$t_{end}(s)$
5.0	-0.2	-10.0	10.0	100.0

The results shown in Figure 33 below and Figure 61 in Appendix B exhibit similar trends for the same reasons. It can be observed that the final voltage magnitudes oscillate for the lowest values of the delay. This behaviour is related to the transient response of the synchronous generator, which reacts relatively slowly to the wind power reduction. Depending on the value of ΔT, the electrolyser starts adapting its consumption at a different stage of the generator transient. As a result, the final operating point reached by the system can slightly differ for small delay values. For delays larger than approximately 8 s, the results become almost identical, since the synchronous generator has already damped most of the transient caused by the downward wind ramp before the electrolyser starts reacting.

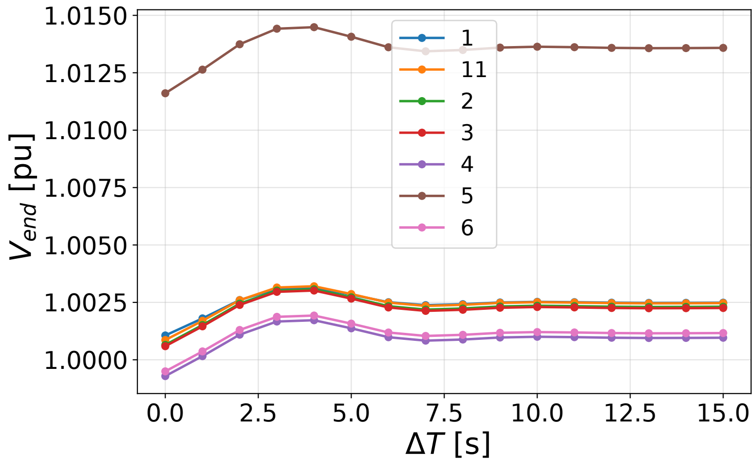

Figure 33: Final voltage magnitudes at each bus of the network for different values of the electrolyser reaction delay ΔT.

The corresponding mean reactive powers are reported in Appendix B. They confirm that the delay has only a weak influence on the reactive power sharing, which remains dominated by the synchronous condenser.

Concerning the mean active powers, Figure 34 shows that the active power supplied by the synchronous generator increases almost linearly with the electrolyser reaction delay. This result is expected, since a larger delay means that the system remains for a longer time with reduced wind generation while the electrolyser consumption has not yet been reduced. During this interval, the resulting active power deficit must be mainly supplied by the synchronous generator.

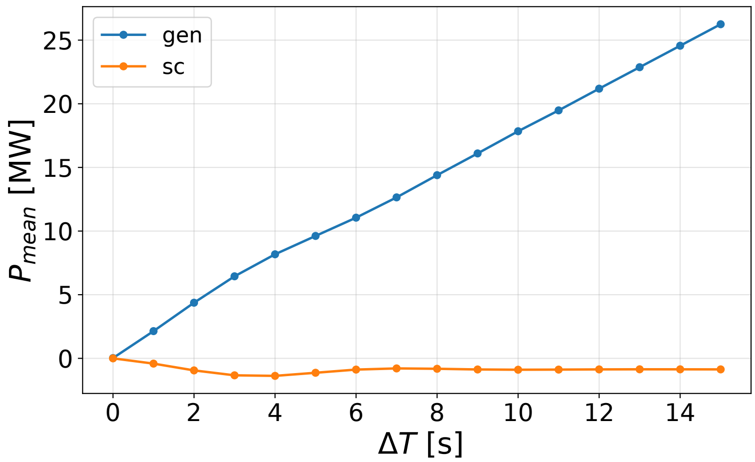

Figure 34: Mean active power exchanged by the synchronous machines for different values of the electrolyser reaction delay ΔT.

Figure 35 shows that the frequency nadir decreases when the electrolyser reaction delay increases up to about 3 s, and then remains almost constant. This is expected, since a larger delay means that the active power deficit caused by the wind power reduction is compensated later by the electrolyser load reduction. The fact that the nadir stops decreasing after approximately 3 s suggests that, in this case, the synchronous generator needs about 3 s to arrest most of the initial frequency drop.

The final estimated frequency exhibits a peak for low delay values, around 3 and 4 s. This is consistent with the transient behaviour already observed on the voltage curves: for these delay values, the electrolyser reacts while the synchronous generator is still adapting its mechanical power. This can temporarily create an active power surplus and lead to a higher final frequency. For larger delays, the final frequency decreases and becomes almost constant, indicating that the system response becomes less sensitive to the exact value of ΔT.

It should also be noted that, for delays larger than about 1 s, the final estimated frequency exceeds the 51.5 Hz threshold. This suggests that even relatively short delays in the electrolyser response can lead to significant over-frequency excursions in this scenario.

Figure 36 depicts the maximum apparent power reached by the synchronous generator increases with the electrolyser reaction delay, before stabilising for delays larger than 5 s. This behaviour reflects the longer duration of the active power imbalance when the electrolyser response is delayed, which requires a stronger transient contribution from the synchronous generator. The saturation of $S_{\max}$ for larger delays indicates that, beyond a certain delay, the maximum

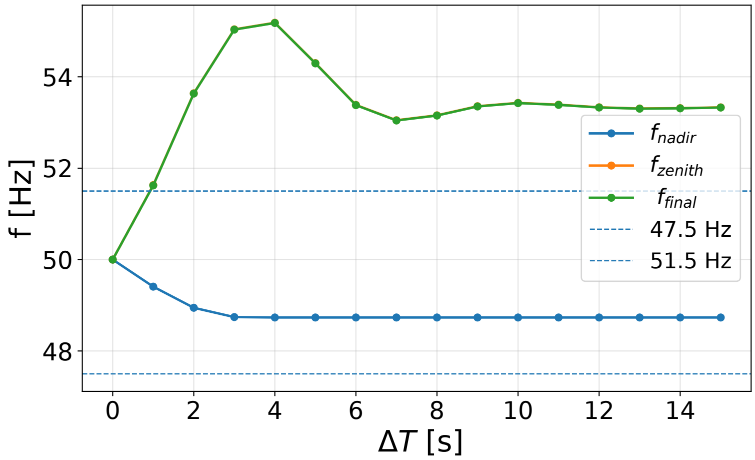

Figure 35: Final, zenith and nadir frequencies for different values of the electrolyser reaction delay ΔT.

power mismatch is mainly determined by the magnitude of the wind power ramp rather than by the exact value of ΔT. The synchronous condenser reaches a much lower maximum apparent power and is only weakly affected by the delay. The plateau value reached in this sensitivity analysis is also higher than in the previous one, about 175 MVA compared with about 87 MVA previously.

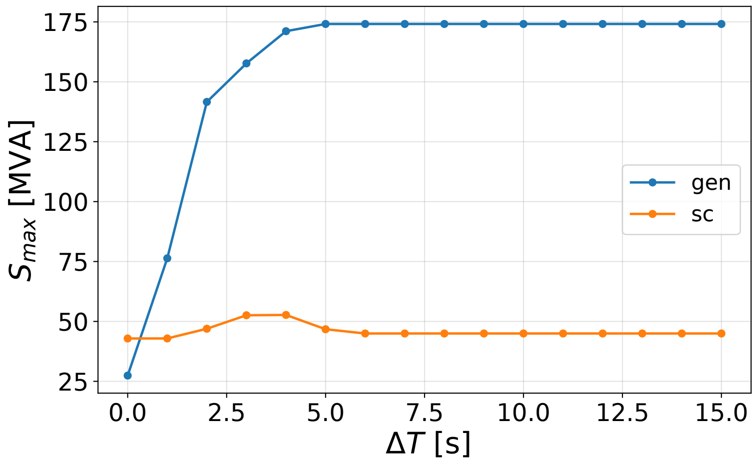

Figure 36: Maximum Apparent Power of synchronous machines reach for different values of the electrolyser reaction delay ΔT.

The extrema and final value of the relative rotor angle between the two synchronous machines for different values of the electrolyser reaction delay are shown in Figure 37. The observed trend is similar to the one obtained in the sensitivity analysis on the wind ramp size: the maximum relative angle increases with the delay, before reaching a plateau for delays larger than approximately 5 s. The underlying mechanism is the same as previously discussed. A larger electrolyser reaction delay increases the time during which the synchronous generator has to compensate the active power deficit alone, while the synchronous condenser exchanges almost no active power. This leads to a larger transient speed difference between the two machines and therefore to a larger relative rotor angle deviation. Once the delay is sufficiently large, the maximum angular excursion is no longer significantly affected by the exact value of ΔT, since it is mainly limited by the magnitude of the wind power ramp and by the transient response of the synchronous machines. The final relative angle remains also close to zero for all delay values, indicating that the angular separation is only transient and that no significant permanent angular offset remains after the system has reached its new operating point. Similarly to the maximum apparent power, the plateau value reached in this sensitivity analysis is higher than in the previous one, with a maximum relative angle of about 28° compared with about 12°.

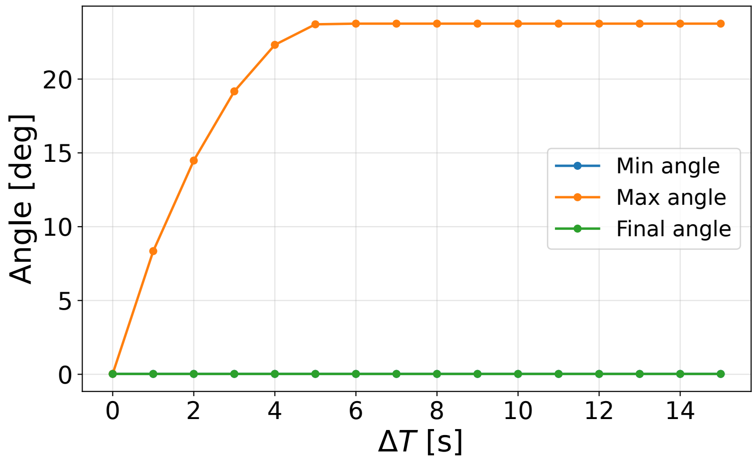

Figure 37: Max angle deviation between the rotors of the synchronous machines for different values of the electrolyser reaction delay ΔT.

7.2.2 Influence of the electrolyser ramp slope

Another parameter of the electrolyser response is now analysed. Different values of the electrolyser ramp slope α_{H_2} are tested, while the other parameters are kept constant, as shown in Table 11. The wind power reduction is the same as in the previous section, with a constant delay of 1 s before the start of the electrolyser response. The ramp slope is varied between 2.5%/s and 40%/s, respectively corresponding to ramp durations between 8 and 0.5 seconds. The objective is to assess the impact of the electrolyser capability to rapidly adapt its consumption.

Table 11: Constant parameters of the sensitivity analysis related to the electrolyser slope reaction $\alpha_{H_2}(\%/s)$

$t_w(s)$	$\Delta P_w(pu)$	$\alpha_w(\%/s)$	$\Delta T(s)$	$t_{end}(s)$
5.0	-0.2	-10.0	1.0	100.0

The final voltage magnitudes are plotted in Figure 38. They increase slightly with the electrolyser ramp duration, before stabilizing for ramp durations larger than approximately 4 s. In other words, a slower electrolyser response leads to slightly higher final voltage magnitudes. This may be related to the fact that, when the electrolyser consumption is reduced more gradually, the synchronous generator has more time to adapt its mechanical power during the transient. As a result, the transition towards the new operating point is less abrupt, and the final voltage magnitudes are not further affected once the ramp duration becomes sufficiently large.

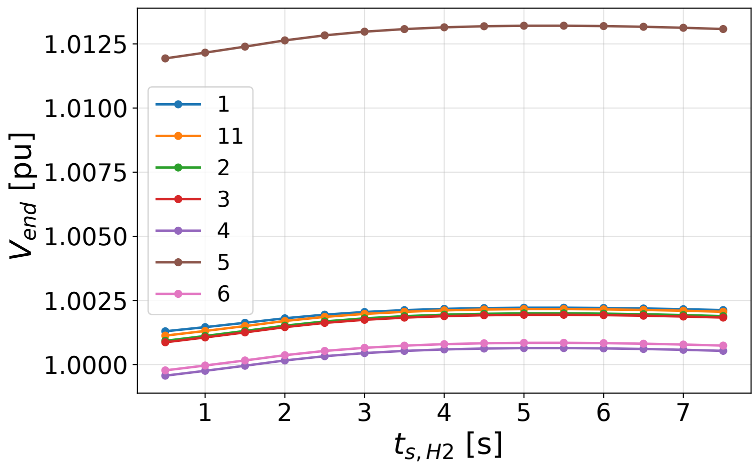

Figure 38: Final voltage magnitudes at each bus of the network for different durations of the electrolyser ramp.

Concerning the mean active power exchanges, Figure 39 shows that the active power supplied by the generator increases with the electrolyser ramp duration. This is expected, since a slower electrolyser response means that the active power deficit caused by the wind power reduction lasts longer. The mean active power of the synchronous condenser is slightly negative. The negative value can be related to the transient exchange of kinetic energy with the system, especially since the final frequency is higher than the initial one, meaning that the rotor has absorbed more active energy than it has released over the simulated period.

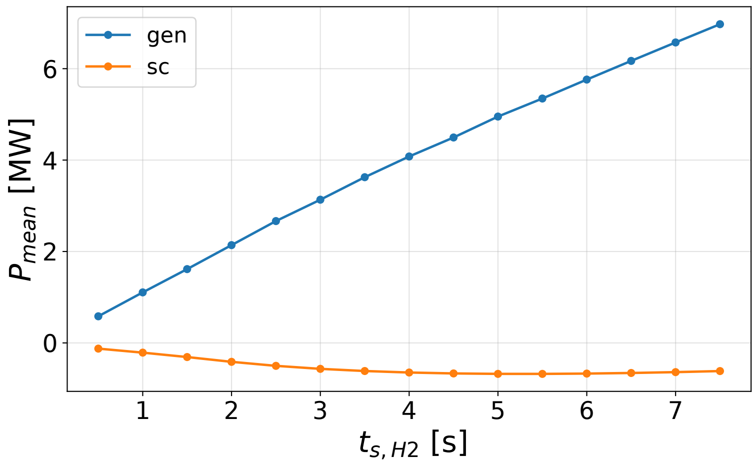

Figure 39: Mean active power exchanged by the synchronous machines for different durations of the electrolyser ramp.

For the mean reactive powers, the results are almost unaffected by the electrolyser ramp duration. The mean reactive power remains around 29 MVAr for the synchronous condenser and around 1 MVAr for the synchronous generator. The corresponding plot is shown in Appendix B.

Concerning the frequency indicators, Figure 40 shows that the final estimated frequency increases with the electrolyser ramp duration, before reaching a maximum around 5 s and then slightly decreasing. At the same time, the frequency nadir decreases when the ramp duration increases, which indicates that a slower electrolyser response delays the compensation of the active power deficit created by the wind power reduction.

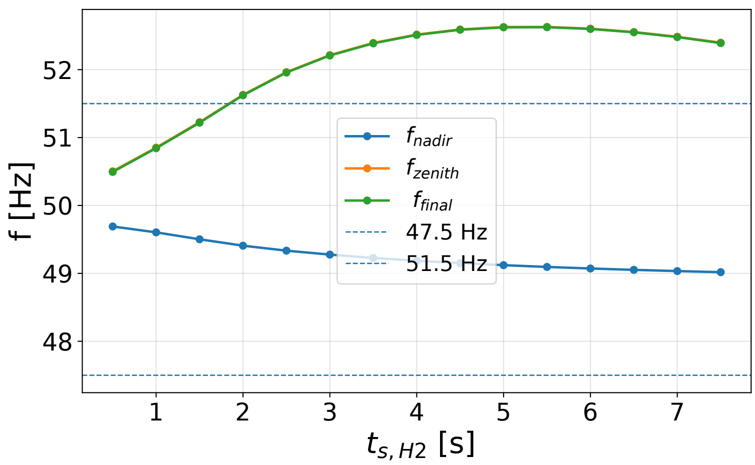

Figure 40: Final, zenith and nadir frequencies for different durations of the electrolyser ramp.

The evolution of the final frequency can be explained by the interaction between the progressive electrolyser load reduction and the mechanical response of the synchronous generator. When the electrolyser consumption is progressively reduced, this can lead to an overcompensation and therefore to a higher final frequency. However, for the longest ramp durations, the load reduction becomes sufficiently gradual for the generator response to adapt during the transient, so that the final frequency no longer increases and even slightly decreases. This behaviour is consistent with the trend observed in the sensitivity analysis with different ramp sizes, although the mechanism is not exactly the same: here, the wind power ramp is already completed while the electrolyser consumption is still changing. For ramp durations larger than approximately 2 s, the final estimated frequency exceeds the 51.5 Hz threshold, showing that the electrolyser ramp slope has a significant impact on the over frequency reached after the disturbance.

A more gentle reduction of the electrolyser consumption prolongs the active power imbalance, so the synchronous generator has to provide a larger transient contribution. This leads to an increase in the maximum apparent power reached by the synchronous generator. In contrast, the synchronous condenser is almost unaffected and remains at a nearly constant apparent power, since it mainly provides reactive support. These trends are shown in Figure 41.

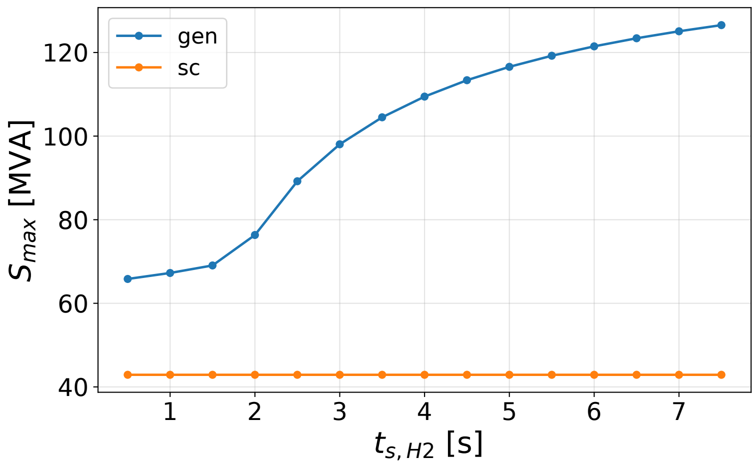

Figure 41: Maximum apparent power reached by the synchronous machines for different durations of the electrolyser ramp.

The same tendency is observed for the relative rotor angle between the two synchronous machines, shown in Figure 42. The maximum relative angle increases with the electrolyser ramp duration. The minimum and final values remain close to zero, for the same reasons as explained in the two previous sensitivity analyses. This behaviour is consistent with the previous observation on the maximum apparent power. When the electrolyser consumption is reduced more slowly, the active power deficit remains larger during the transient than with a fast electrolyser ramp. The synchronous generator therefore has to provide a larger active power contribution, which also explains the increase in its maximum apparent power. Since the synchronous condenser exchanges almost no active power, the two machines experience different rotor-speed deviations during the disturbance. This results in a larger transient relative rotor angle deviation.

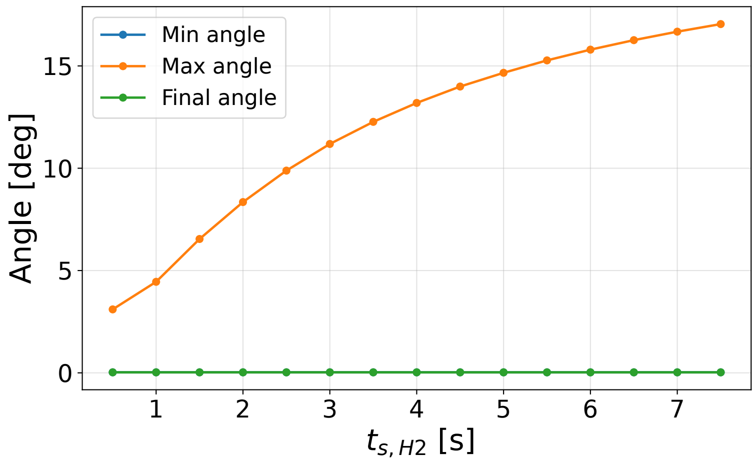

Figure 42: Extrema and final value of the relative rotor angle between the synchronous machines for different durations of the electrolyser ramp.

7.3 Sensitivity to external grid strength

The sensitivity analysis now focuses on the influence of the external grid strength on the system response to a disturbance. The parameter varied is the reactance of the transformer connecting the external generator to the system, denoted $X_{gen,trfo}$. This parameter is considered because the total impedance between the generator and the grid directly influences the short-circuit ratio, and therefore the grid strength. As usual, the other parameters are kept unchanged during the analysis and are shown in Table 12. The wind power reduction and the wind ramp slope are the same as in the previous sections, as is the response delay of the electrolyser. However, the electrolyser ramp slope is higher than in the previous analyses. This choice is based on the results of the previous section, where it was shown that the electrolyser ramp duration must remain below approximately 2 s in order to keep the final frequency within the acceptable limits.

Table 12: Constant parameters of the sensitivity analysis related to the external bus strength.

$t_w(s)$	$\Delta P_w(pu)$	$\alpha_w(\%/s)$	$\alpha_{H_2}(\%/s)$	$\Delta T(s)$	$t_{end}(s)$
5.0	-0.2	-10.0	13.3	1.0	100.0

Concerning the voltage indicators, several trends can be observed. The first ones are the voltage peaks, Figure 43 shows that the maximum voltages increase almost linearly with the transformer reactance at most buses. This is expected, since a higher transformer reactance makes the external generator more electrically distant from the network, so the system is less strongly supported during the disturbance. The voltage deviations are therefore amplified. The main exception is bus 1, which remains almost constant. This is explained by the fact that this bus is directly connected to the external generator and is therefore connected ahead of the transformer, making its voltage unsensitive to the transformer reactance.

The second ones are the final voltages, all bus voltages remain broadly similar, except for the bus connected to the synchronous condenser, whose voltage increases almost linearly with the transformer reactance. The final voltage at bus 1,

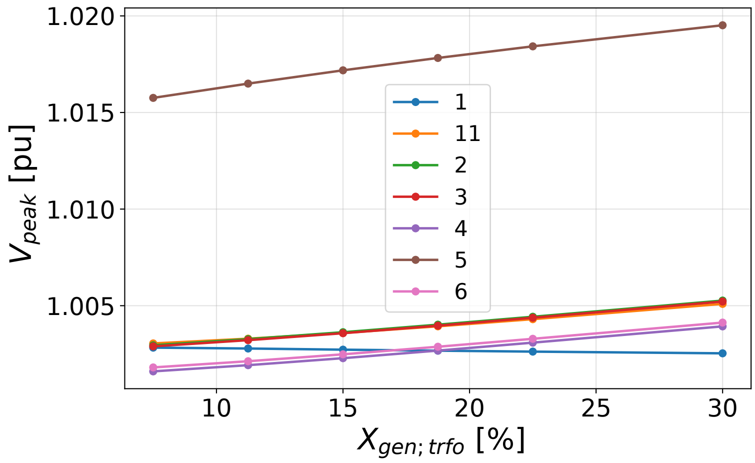

Figure 43: Voltage peaks at each bus of the network for different values of the external generator transformer reactance $X_{gen;ext}$.

connected to the external generator, slightly decreases. The corresponding graph is shown in Appendix B.

Finally, the voltage nadirs are shown in Figure 44. The nadir decreases below the nominal value with the transformer reactance at most buses, which is consistent with the weaker connection to the external generator. A higher transformer reactance reduces the ability of the external generator to support the network voltage during the disturbance, resulting in deeper voltage dips. Buses 1 and 5 are not affected, because they are directly associated with voltage controlled synchronous machines.

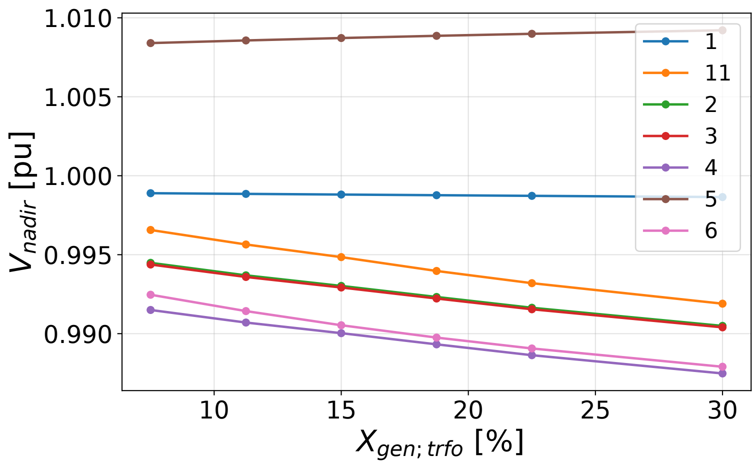

Figure 44: Voltage nadirs at each bus of the network for different values of the external generator transformer reactance $X_{gen;ext}$.

Figure 45 highlights the evolution of the mean reactive power exchanges. The synchronous condenser provides increasing reactive power support as the transformer reactance increases, while the reactive power supplied by the generator decreases. The two trends are almost linear and opposite. This is consistent with the generator electrically more distant from the rest of the network, reducing its ability to support the voltage at the other buses. As a result, the synchronous condenser has to provide a larger share of the reactive power support.

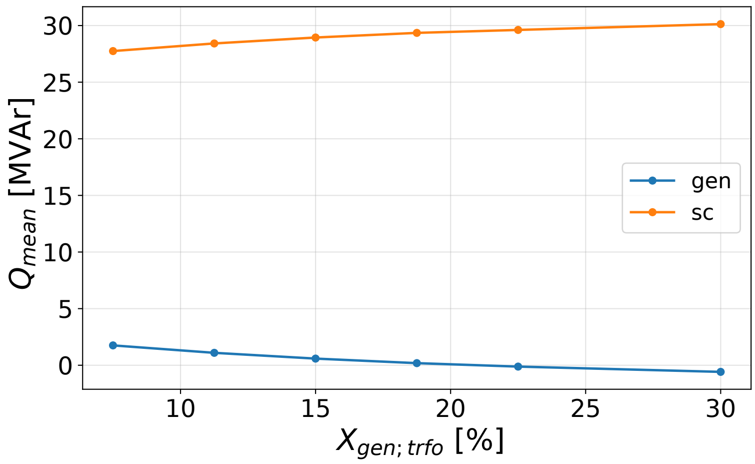

Figure 45: Mean reactive power exchanged by the synchronous machines for different values of the external generator transformer reactance $X_{gen;ext}$.

The mean active power exchanged by the synchronous machines is almost unaffected by the transformer reactance. This is expected, since the active power imbalance is imposed and remains the same in all cases. The transformer reactance mainly affects the voltage profile and the reactive power sharing. The corresponding plot is provided in Appendix B.

The frequency nadir, zenith and final frequency, as well as the maximum absolute RoCoF, remain unchanged during this sensitivity analysis. The corresponding plots are provided in Appendix B. In all cases, the final frequency is around 51.2 Hz, while the frequency nadir is around 49.5 Hz. This also confirms that the transformer reactance mainly affects the voltage profile and the reactive power sharing, while the active power imbalance governing the frequency response remains constant.

The evolution of the maximum apparent power is depicted in Figure 46. The maximum apparent power of the generator slightly decreases, while the one of the SC increases a lot linearly. And it increased more (from 38MVA to 50MVA, whereas its Mean Q was increasing from 27.5 to 30MVAr), so the sc is really more in demand during the transient (j'imagine).

The evolution of the maximum apparent power is depicted in Figure 46. The maximum apparent power reached by the synchronous generator slightly decreases as the transformer reactance increases, while that of the synchronous condenser increases significantly. This is consistent with the weakening of the connection between the external generator and the rest of the system. As the generator becomes electrically more distant, its ability to provide voltage support to the network is reduced, and a larger share of the reactive support is provided by the synchronous condenser.

It should be noted that, for the synchronous condenser, the maximum apparent power is reached before the wind power ramp. Since the downward wind ramp leads to higher voltage magnitudes after the disturbance, the reactive power requirement of the condenser is larger in the initial operating condition than during and after the transient.

This also explains why the increase in $S_{\max}$ is more pronounced than the increase in the mean reactive power. Indeed, $S_{\max}$ increases from about 38 MVA to 50 MVA, whereas the mean reactive power only increases from about 27.5 MVAr to 30 MVAr. The maximum value reflects the higher pre disturbance reactive power requirement when the transformer reactance is increased.

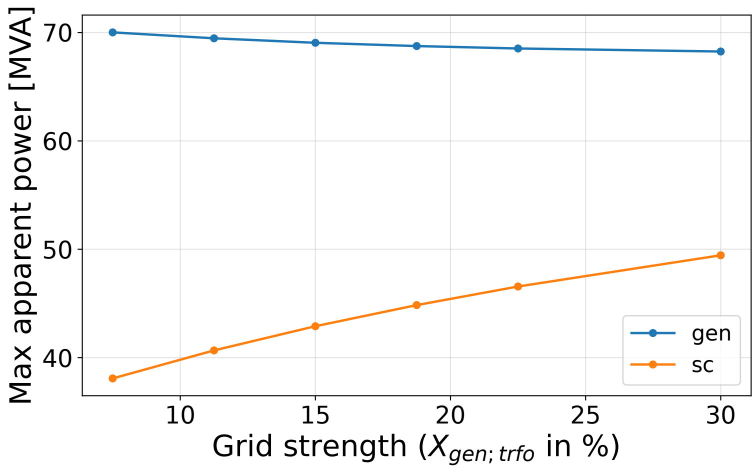

Figure 46: Maximum apparent power reached by the synchronous machines for different values of the external generator transformer reactance $X_{gen,trfo}$.

7.4 Sensitivity to inertia

This section presents a sensitivity analysis based on the total inertia available in the system. The inertia constants H of both rotors are scaled by a multiplier λ varying from 0.5 to 2, with a step of 0.25. Therefore, the analysis assesses the impact of a system with half the initial inertia up to twice the initial inertia.

The inertia constant can also be expressed in terms of stored kinetic energy. By definition,

$$H = \frac{E_{\text{kin}}}{S_N}, \tag{20}$$

where E_{kin} is the kinetic energy stored in the rotating masses and S_N is the nominal apparent power of the machine. Therefore,

$$E_{\text{kin}} = H \cdot S_N. \tag{21}$$

In the reference case, the synchronous generator has $H = 4$ s and $S_N = 800$ MVA, corresponding to 3200 MWs of stored kinetic energy. The synchronous condenser has $H = 2$ s and $S_N = 300$ MVA, corresponding to 600 MWs. The total kinetic energy of the synchronous machines is therefore 3800 MWs in the base case. With the multiplier λ, this total value varies from 1900 MWs for $\lambda = 0.5$ to 7600 MWs for $\lambda = 2$.

These values are in the range of real synchronous condenser applications equipped with flywheels. For example, Siemens Energy reports synchronous condenser solutions with additional flywheels providing kinetic energies of about 1100 MWs, and up to 4000 MWs for larger installations [41]. In the present study, the synchronous condenser alone varies from 300 MWs to 1200 MWs over the sensitivity range, which remains comparable to industrial flywheel-based solutions.

The other parameters are once again kept unchanged throughout the analysis and are detailed in Table 13.

Table 13: Constant parameters of the sensitivity analysis related to the inertia of the system.

t_w (s)	ΔP_w (pu)	α_w (%/s)	α_{H_2} (%/s)	ΔT (s)	t_{end} (s)
5.0	-0.2	-10.0	10.0	1.0	100.0

The final voltage magnitudes at each bus are depicted in Figure 47. As the inertia multiplier λ increases, the final voltages tend to move closer to their nominal or controlled operating values. The same trend is observed for the voltage peaks, which are reported in Appendix B. This suggests that a higher system inertia reduces the severity of the electromechanical transient following the active power imbalance. As a result, the power flows vary less abruptly, which also limits the associated voltage deviations.

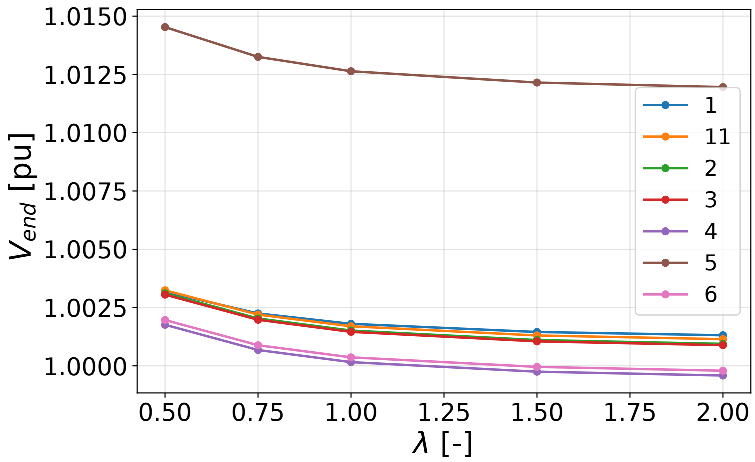

Figure 47: Final voltage magnitudes at each bus of the network for different values of the multiplier λ.

A similar improvement is observed for the voltage nadirs, shown in Figure 48. The minimum voltages increase when the inertia is increased, meaning that the voltage dips are less pronounced.

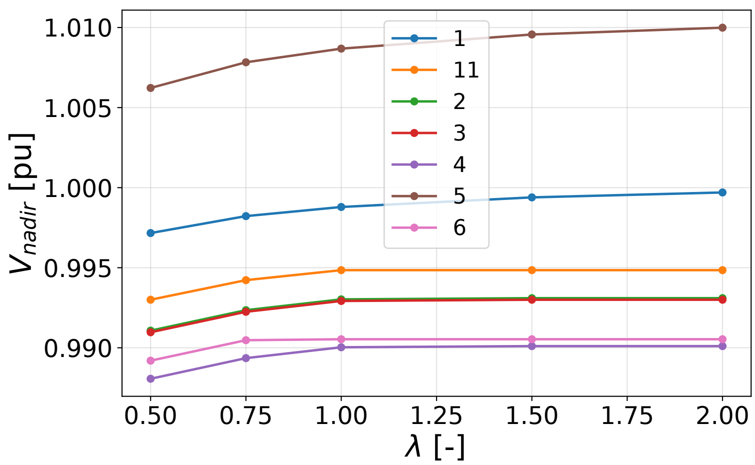

Figure 48: Voltage nadirs at each bus of the network for different values of the multiplier λ.

No significant changes are observed for the mean active and reactive powers. The graphs are therefore provided in Appendix B. The mean active and reactive powers are only weakly affected by the inertia. The corresponding plots are therefore provided in Appendix B. This is expected, since modifying the inertia mainly affects the transient electromechanical dynamics, such as the frequency excursion and the RoCoF, while the average active and reactive power exchanges remain mostly determined by the operating point and by the wind and electrolyser power variations.

In contrast, the frequency indicators are strongly affected by the inertia variation, as illustrated in Figure 49. The final estimated frequency decreases when the inertia multiplier increases. For values of λ lower than or equal to 1, the final frequency remains above the upper limit of 51.5 Hz, whereas it stays below this threshold for higher inertia values. The frequency nadir also improves with increasing inertia, although it remains within the admissible range for all cases. This behaviour is expected: for a given active power imbalance, a larger inertia means that more kinetic energy is stored in the rotating masses. As a result, the same energy exchange causes a smaller variation of rotor speed, which reduces both the frequency deviation and the RoCoF. The RoCoF follows the same trend. The maximum RoCoF decreases from about 1.7 Hz/s to about 0.23 Hz/s, while the minimum RoCoF varies from about -0.8 Hz/s to about -0.25 Hz/s. This confirms that additional inertia makes the frequency response slower and less severe, and highlights its beneficial effect on the initial dynamic response of the system after the wind power reduction. Similar non-linear relationships between system inertia, frequency deviations and RoCoF are discussed in [33].

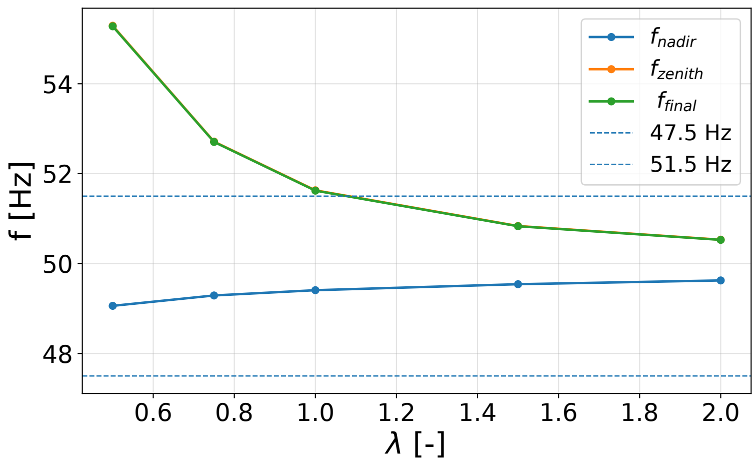

Figure 49: Final, zenith and nadir frequencies for different values of the multiplier λ.

The maximum apparent power reached by the synchronous machines decreases when the inertia multiplier increases, as shown in Figure 50. This result is predictable with the previous frequency indicators, as mentionned before, with higher inertia, the electromechanical transient is less severe. As a result, the transient contribution required from the synchronous generator is reduced, which lowers its maximum apparent power. For the synchronous condenser, the maximum apparent power decreases mainly between $\lambda = 0.5$ and $\lambda = 0.75$, and then remains almost constant. This suggests that, beyond this point, its maximum apparent power is mainly determined by the reactive power required for voltage support rather than by the inertial response itself.

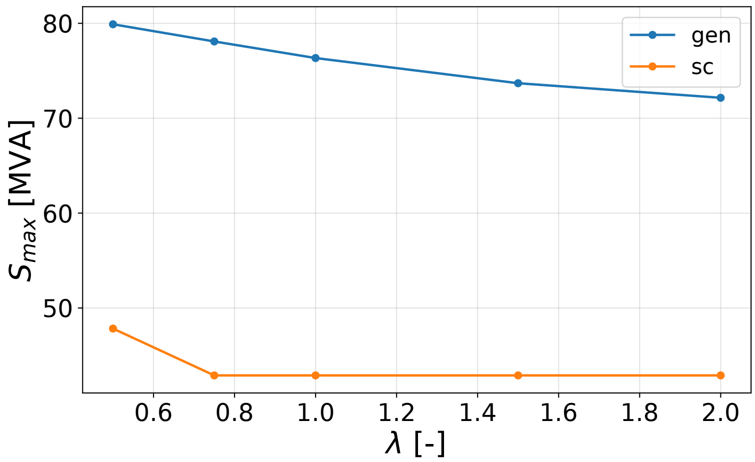

Figure 50: Maximum apparent power reached by synchronous machines for different values of the multiplier λ.

Finally, the maximum relative rotor angle between the two synchronous machines also decreases when the inertia multiplier increases, as shown in Figure 51. This is consistent with the swing dynamics: for the same active power imbalance, higher inertia reduces the rotor speed deviations of the machines. Although the speed differences between the synchronous generator and the synchronous condenser remain very small, they accumulate over time and lead to a noticeable relative rotor angle deviation. When the inertia is increased, these speed differences are reduced during the transient, and their time integral is therefore smaller. This explains the lower maximum relative rotor angle observed for larger values of λ.

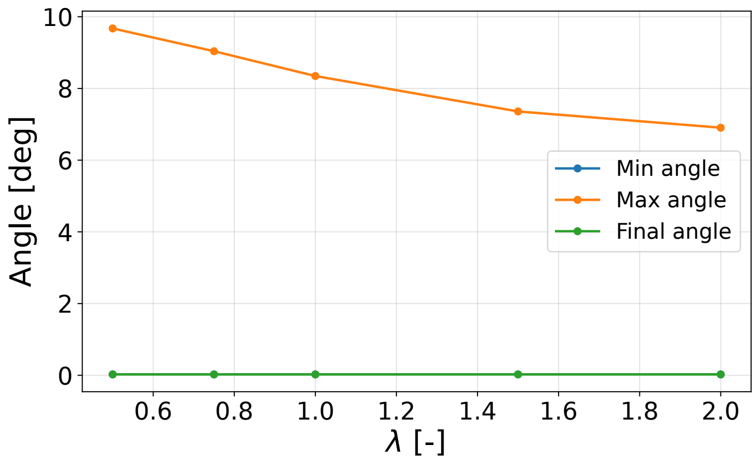

Figure 51: Extrema and final value of the relative rotor angle between the synchronous machines for different values of the multiplier λ.

7.5 Sensitivity to voltage support strategy

In the following section, four voltage support strategies are compared. In the baseline case, both VSCs operate in reactive power control (PQ) mode, with zero reactive power exchange, as in the previous sections. In the other cases, either the wind VSC, the electrolyser VSC, or both VSCs are switched to voltage control (PV) mode. This makes it possible to assess whether converter based voltage support can reduce the reactive power burden imposed on the synchronous machines.

7.5.1 Comparison under a representative disturbance

The four operating modes are first compared for a single representative downward wind power variation. The objective is to analyse the transient voltage response and the redistribution of reactive power support between the synchronous machines and the converters. The parameters of the simulation are reported in Table 14.

Table 14: Parameters of the dynamic simulation facing downward wind power reduction.

$t_w(s)$	$\Delta P_w(pu)$	$\alpha_w(\%/s)$	$\Delta P_{H_2}(pu)$	$\alpha_{H_2}(\%/s)$	$\Delta T(s)$	$t_{end}(s)$
10.0	-0.2	-10.0	0.2	10	1.0	100.0

Figure 52 compares the time-domain responses of the reactive power exchanged by the VSCs and the voltage magnitudes at their respective buses for the four operating modes. In the legend, $\mathrm{PQ_{wind}} - \mathrm{PQ_{H_2}}$ denotes the baseline case, $\mathrm{PV_{wind}} - \mathrm{PQ_{H_2}}$ the case where only the wind VSC operates in voltage control, $\mathrm{PQ_{wind}} - \mathrm{PV_{H_2}}$ the case where only the electrolyser VSC operates in voltage control, and $\mathrm{PV_{wind}} - \mathrm{PV_{H_2}}$ the case where both VSCs operate in voltage control.

Both voltage dips at buses 6 and 4 are reduced when both VSCs operate in PV mode, and the subsequent voltage peaks are also lower. This therefore leads to a smoother voltage profile.

The voltage control strategy behaves as expected: the VSCs produce more reactive power when the voltage decreases and reduce their reactive power injection when the voltage rises. In addition, the reactive power peaks are shared between the two converters when both VSCs operate in PV mode, which leads to lower individual reactive power peaks than in the cases where only one VSC operates in PV mode.

It can also be observed that operating only one VSC in PV mode already improves the voltage response at both buses, not only at the bus where voltage control is applied. This highlights the electrical coupling between the two buses and the system wide effect of converter based voltage support.

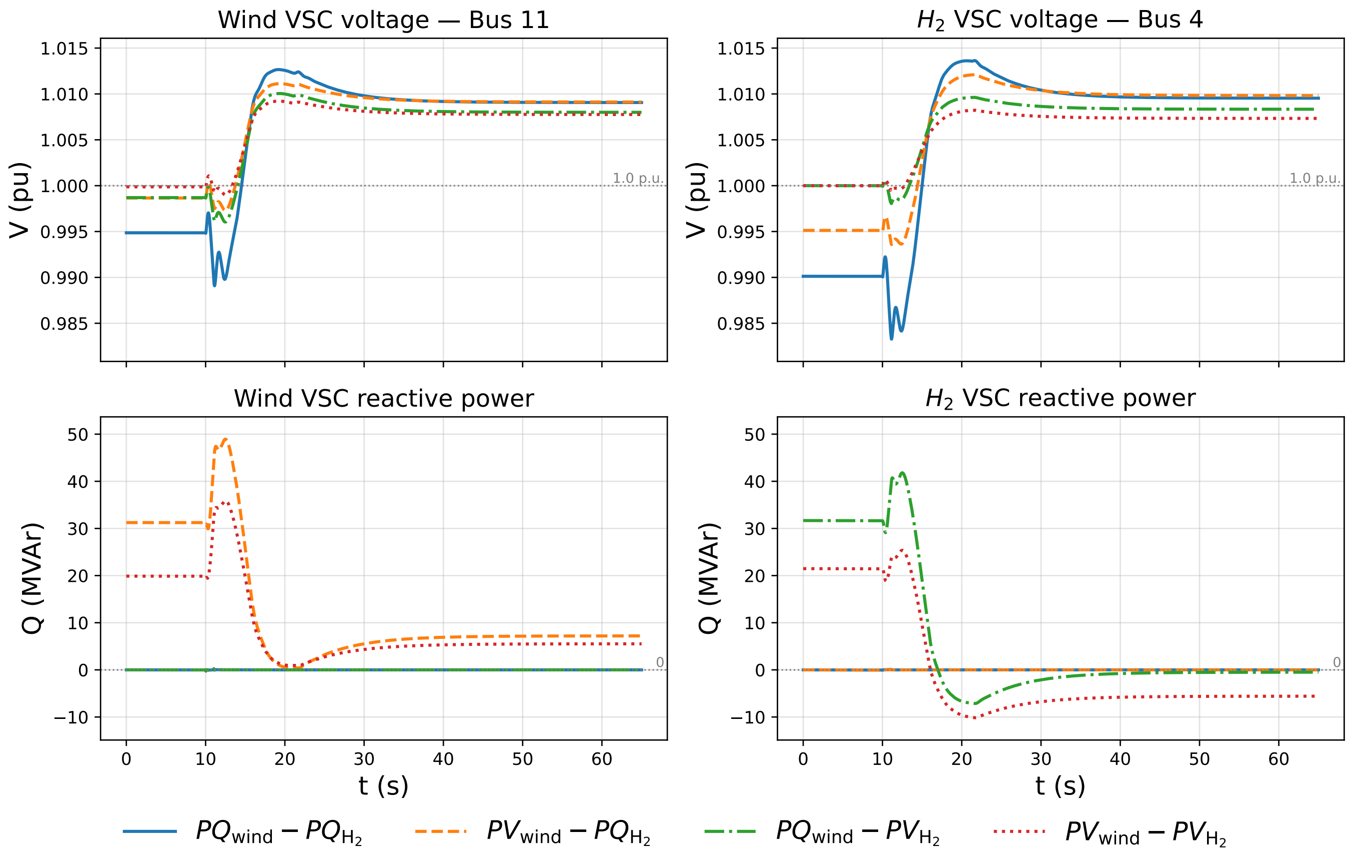

Figure 52: Comparison of the dynamic responses of the voltage magnitudes at buses 6 and 4 and of the reactive power exchanged by both VSCs for the four VSC operating modes.

Figure 53 presents the same comparison as before, but for the voltage magnitudes at the synchronous machine buses and for the reactive power exchanged by the synchronous generator and the synchronous condenser.

Concerning the voltage profiles, the impact of the VSC operating mode is more visible at bus 5, where the synchronous condenser is connected, than at bus 1, where the synchronous generator is connected. This is consistent with the fact that the voltage variations at the synchronous condenser bus are larger than those at the generator bus for all VSC operating modes. Among the four cases, the PV-PV mode provides the smoothest voltage response, with slightly reduced voltage dips and peaks compared to the other modes.

Regarding the reactive power exchanges, in the baseline PQ-PQ case, the synchronous generator initially provides a significant amount of reactive power. When more VSCs are operated in PV mode, this initial reactive power contribution decreases, reaching almost zero for the generator in the PV-PV case. During the wind reduction, the generator even absorbs reactive power instead of producing it. The same trend is observed for the synchronous condenser. In PV-PV mode, its reactive power production is reduced both during the voltage dip and during the subsequent voltage peak. This confirms that converter based voltage control reduces the reactive power burden imposed on the synchronous machines, not only in steady state but also during the transient response.

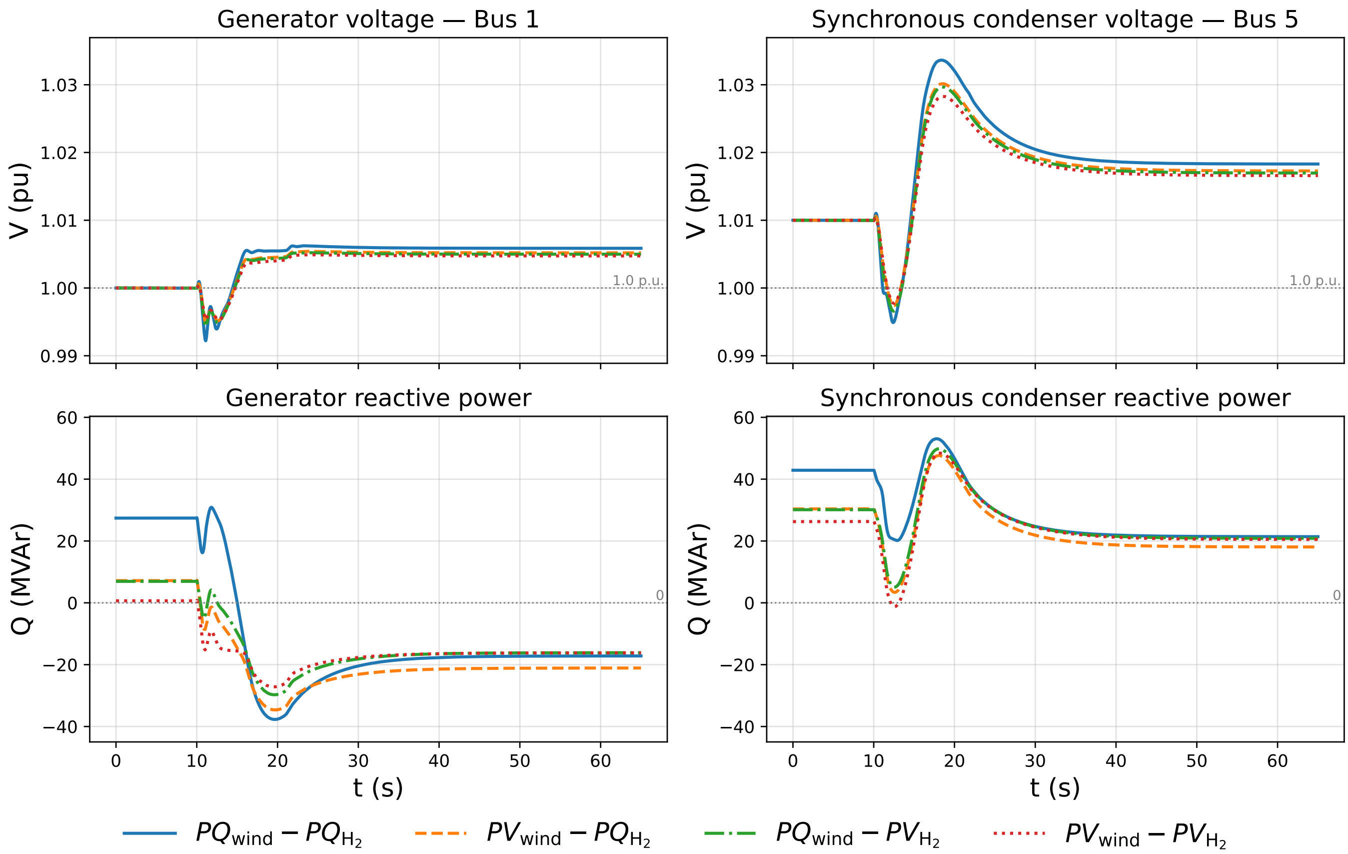

Figure 53: Comparison of the dynamic responses of the voltage magnitudes at buses 1 and 5 and of the reactive power exchanged by the synchronous generator and the synchronous condenser for the four VSC operating modes.

The last comparison focuses on the reactive-current references i_q^{ref} of the VSCs and on their total current magnitudes, as shown in Figure 54. In the PQ-PQ case, the reactive-current references remain close to zero, whereas they vary when one or both VSCs operate in PV mode. These variations are consistent with the reactive power exchanges discussed previously, taking into account the sign convention introduced in Section 4. Since the actual i_q follows i_q^{ref} rapidly, the reference signals provide a good indication of the reactive current contribution of the converters.

However, these variations in i_q^{ref} have only a limited impact on the total current magnitude. The current magnitude remains almost identical for the four operating modes and mainly follows the active power variations of the wind and electrolyser converters. This indicates that, in this case, the converter current loading is mainly determined by the active power exchange rather than by the additional reactive current required for voltage support.

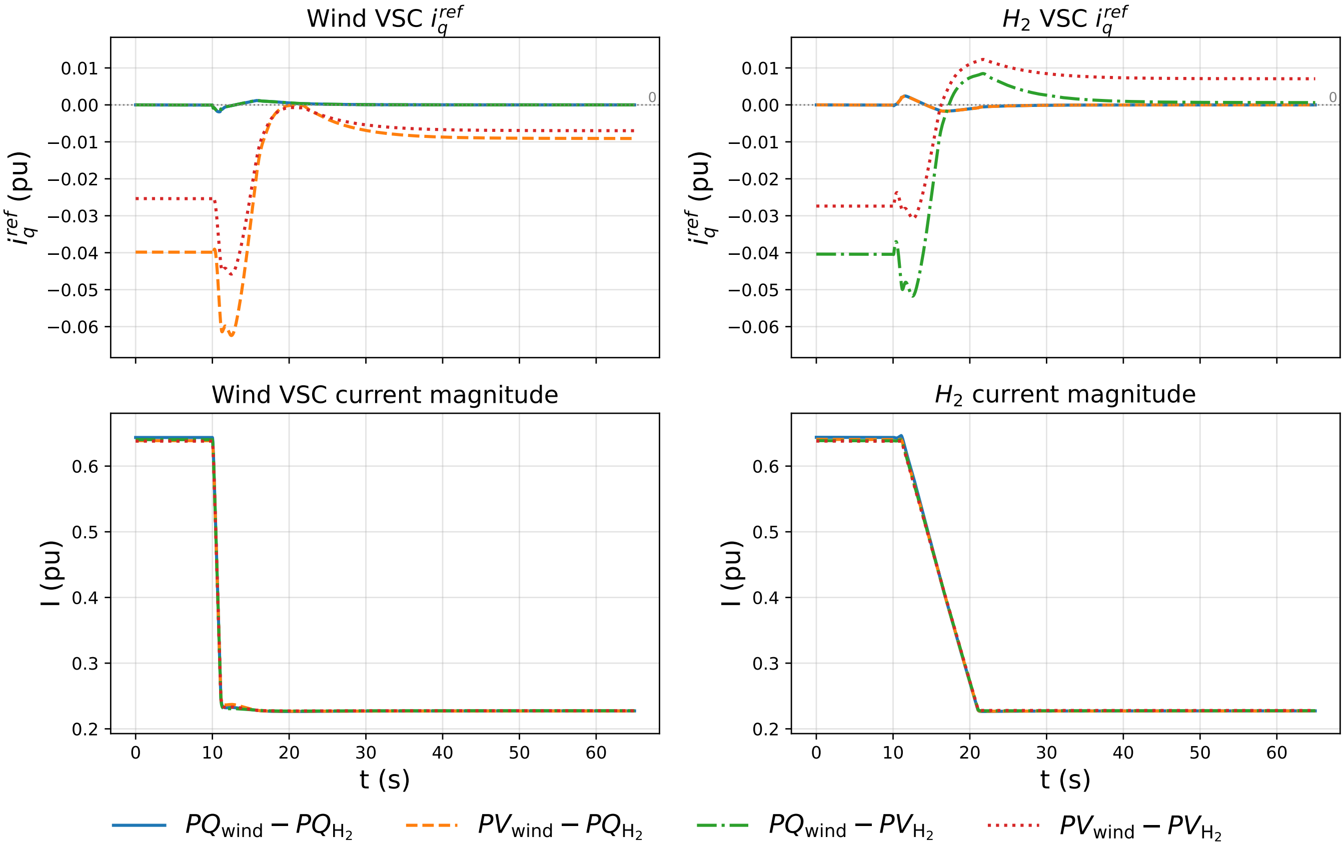

Figure 54: Comparison of the reactive-current references i_q^{ref} and total current magnitudes of both VSCs for the four VSC operating modes.

7.5.2 Influence of the wind ramp size

The comparison is then extended to a sensitivity analysis with different wind ramp sizes, as in Section 7.1. Each value of ΔP_w is simulated for the four VSC operating modes. The resulting indicators are compared in order to evaluate whether the benefits of converter based voltage control remain valid as the disturbance severity increases.

Figure 55 presents the final voltage magnitudes at the buses of the four main devices: the synchronous generator, the synchronous condenser, the wind VSC and the electrolyser VSC. Each point corresponds to one dynamic simulation with a given wind ramp size and a given VSC operating mode.

At buses 1 and 5, the final voltages increase slightly with the wind ramp size for all operating modes. However, the increase is reduced when both VSCs operate in PV mode, which indicates that converter-based voltage control helps to limit the final voltage rise at the synchronous-machine buses.

At bus 6, corresponding to the wind VSC, the final voltage is higher when the wind converter operates in PV mode. The PV-PQ case leads to the highest final voltage at this bus, since the wind VSC provides voltage support alone. When both converters operate in PV mode, the voltage support is shared between the two VSCs, resulting in a slightly lower final voltage at bus 6.

At bus 4, corresponding to the electrolyser VSC, the same behaviour is observed for small wind ramp sizes, operating the electrolyser VSC in PV mode improves the final voltage. For larger wind ramps, the differences between the operating modes become smaller, and the modes where the electrolyser VSC remains in PQ mode can lead to slightly higher final voltages. This suggests that the final voltage profile depends not only on the local voltage control mode, but also on the redistribution of reactive power support between the two converters.

Overall, the PV-PV mode appears to be the least affected by the wind ramp size. This can be seen from the smaller slopes of the corresponding curves at the four buses, indicating that using both VSCs in voltage control mode makes the final voltage profile less sensitive to the disturbance magnitude.

The maximum apparent power reached by the synchronous generator is only weakly influenced by the VSC operating mode. The left panel of Figure 56 indicates that the four curves remain close to each other for all wind ramp sizes. This is coherent with the previous observations: the generator loading is mainly driven by the transient active power imbalance, while the redistribution of reactive power support between the VSCs has only a secondary effect on its maximum apparent power.

The behaviour is different for the synchronous condenser. For a given VSC operating mode, its maximum apparent power is only moderately affected by the wind ramp size. However, the choice of the VSC control mode has a clear influence on the level reached. The PQ-PQ case leads to the highest maximum apparent power, since the synchronous condenser has to provide most of the voltage support. The PV-PV mode gives the lowest values, as both converters

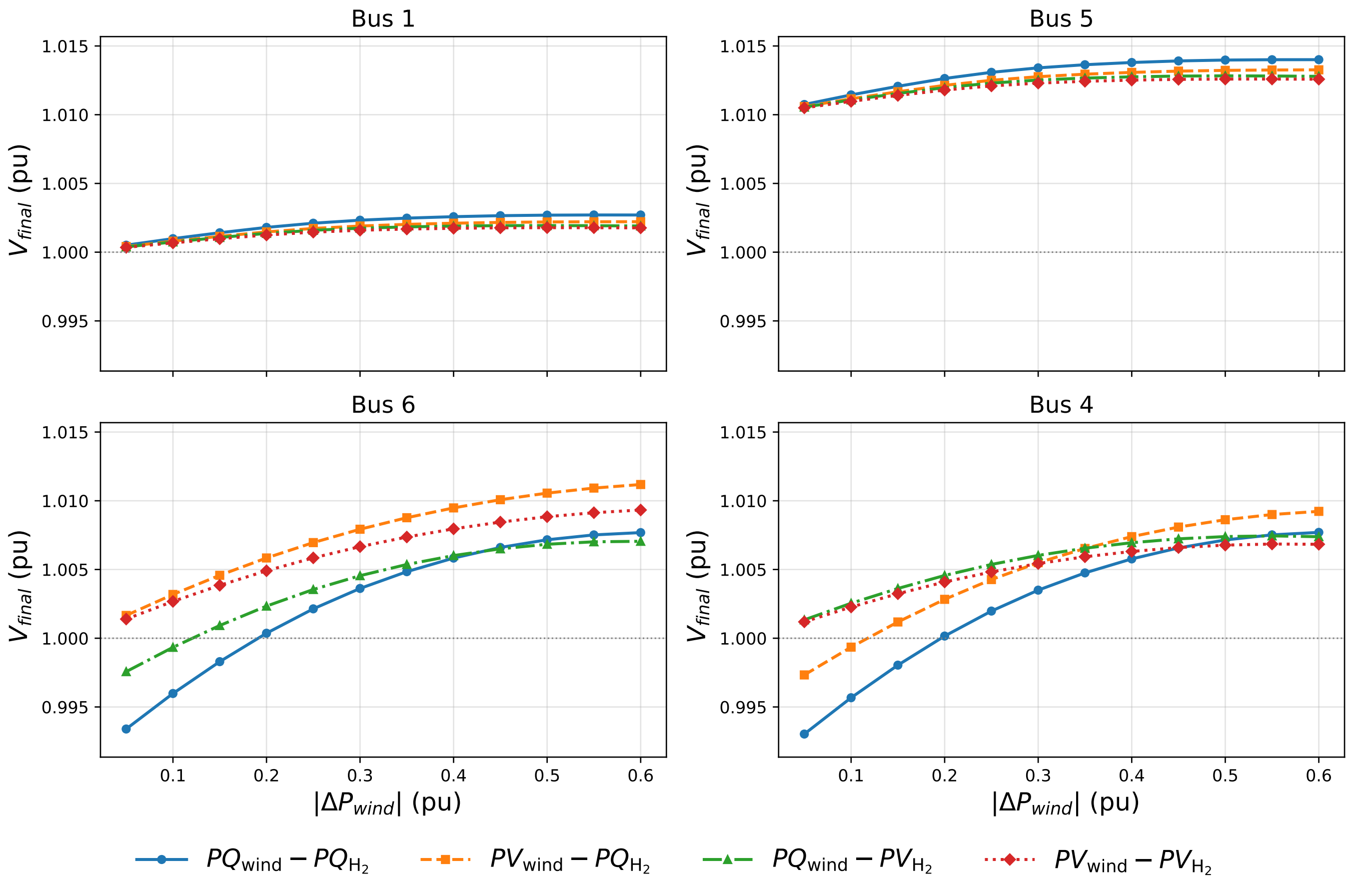

Figure 55: Final voltage magnitudes at the buses of the synchronous generator, synchronous condenser, wind VSC and electrolyser VSC for different wind ramp sizes and VSC operating modes.

contribute to voltage regulation and therefore reduce the reactive power burden on the condenser. The two mixed modes lie between these two cases, with only limited differences depending on which VSC is operated in PV mode.

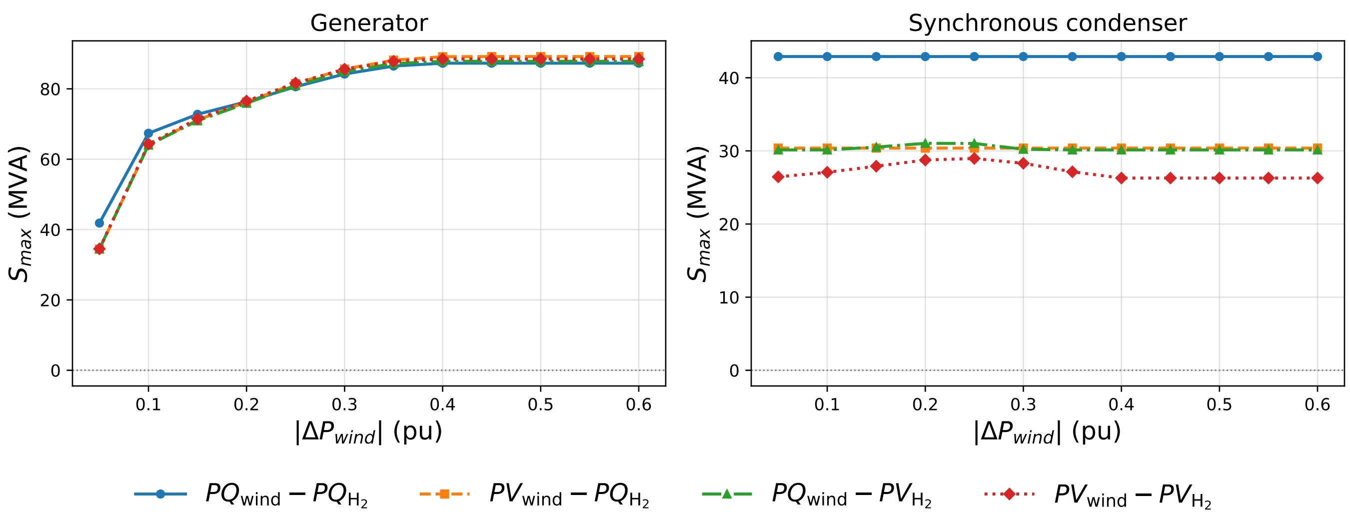

Figure 56: Maximum apparent power reached by the synchronous generator and the synchronous condenser for different wind ramp sizes and VSC operating modes.

The mean reactive power exchanged by the main devices is reported in Figure 57. Overall, the mean reactive power tends to decrease when the wind ramp size increases. This is consistent with the higher voltage levels observed for larger wind ramps: as the voltage rises, the devices providing voltage control reduce their reactive power injection, or even absorb reactive power.

For the VSCs, the mean reactive power remains to zero when they operate in PQ mode, as imposed by their control strategy. When a VSC operates in PV mode, it actively contributes to voltage regulation and therefore exchanges a non zero mean reactive power. However, the wind and electrolyser VSCs do not behave in exactly the same way, even though they use the same voltage control parameters. This difference is mainly related to their electrical location in the network. The electrolyser VSC is connected close to the synchronous condenser, through the same high voltage bus, and is therefore located in a part of the network already strongly influenced by the condenser voltage support. For large wind ramps, the local voltage tends to rise, so the electrolyser VSC reduces its reactive power injection and can even absorb reactive power when both VSCs are PV mode. In contrast, the wind VSC is connected at another bus, behind its own transformer, and remains a net provider of reactive power when operating in PV mode.

For the synchronous machines, the use of converter based voltage control clearly reduces the mean reactive power burden. The synchronous condenser provides the largest reactive support in the PQ-PQ case, whereas its mean reactive power is lower when one or both VSCs operate in PV mode. The generator reactive power also decreases when the VSCs provide voltage support, and it becomes negative for larger wind ramps. This confirms that the VSC voltage control modes redistribute the reactive power support away from the synchronous machines and towards the converters.

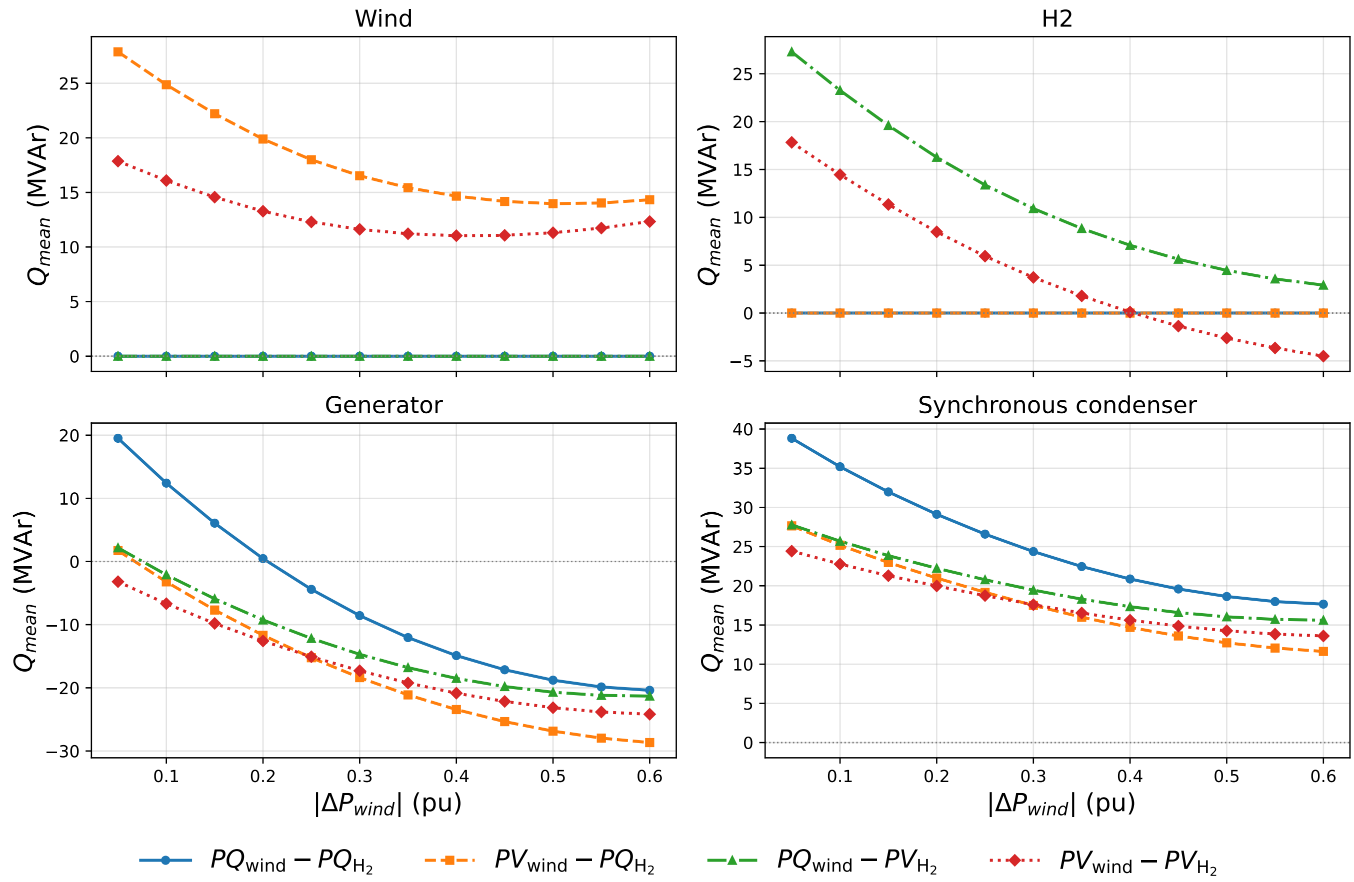

Figure 57: Mean reactive power exchanged by the wind VSC, electrolyser VSC, synchronous generator and synchronous condenser for different wind ramp sizes and VSC operating modes.

7.6 Synthesis and design implications

The sensitivity analyses carried out in this section highlight two main aspects of the system response. First, the voltage behaviour remains globally acceptable. Indeed, the voltage magnitudes stay within the admissible range for the disturbances considered. It is thanks to the voltage supports provided by the excitation system of both synchronous machines, and, in the last part, by the additionnal support introduced with the VSCs operated in voltage control mode. Second, the frequency response appears to be the bottleneck with the specific disturbances applied. Since the active power support is mainly provided by the external synchronous generator and by the predefined reduction of the electrolyser consumption, the system frequency is highly sensitive to the timing and speed of the electrolyser response.

The first sensitivity analysis, based on the wind ramp size, shows that increasing the wind power reduction mainly affects the frequency zenith and the transient loading of the synchronous generator. The frequency nadir remains within the retained limits but nonetheless low at 49.4 Hz, whereas the frequency zenith exceeds the upper threshold for wind power reductions equal or larger than 20%, going until 52 Hz. This indicates that, in this system, with the present delay and speed response of the electrolyser, the main issue is not the initial frequency drop, but rather the over frequency after the end of the wind ramp caused by the excess of mechanical torque from the generator. The generator reaches a maximum apparent power of 88 MVA for wind ramps above 35%. The synchronous condenser just decreases its reactive production during the different wind ramps, therefore its maximum apparent power is occuring before the disturbance, at 43 MVA for all cases.

The sensitivity analysis on the electrolyser reaction delay confirms the importance of the timing of the load adaptation. For a fixed wind power reduction of 20% in 2 s, the voltage indicators remain acceptable for all tested delays. However, the final frequency and the frequency zenith become unacceptable when the delay exceeds approximately 1-2 s. Also, the longer the delay, the lower the nadir, especially for delays smaller than 3s, an electrolyser able to react with 0.3 s delay leads to a nadir of 49.81 Hz, while a delay of 2 s leads already to a nadir of 48.95 Hz. This result is important from a design perspective: the electrolyser response must be sufficiently fast to avoid excessive over and under frequency after the disturbance. The analysis also shows that delays larger than 4 s increase the maximum apparent power of the generator up to 175 MVA and the relative rotor angle deviation between the synchronous machines, because the generator has to compensate the larger active power imbalance before the electrolyser reaction.

The electrolyser ramp slope is another critical parameter. For the same 20% wind power reduction and a fixed delay of 1 s, the frequency response remains acceptable only when the electrolyser ramp duration is short enough. In the simulations, ramp durations larger than approximately 2 s lead to a final frequency above the retained upper limit. This suggests that, in the present system, the electrolyser must be able to reduce its active power consumption rapidly after a wind power decrease. However, perfoming the same simulation with a electrolyser response delay of 0.2 s, allows to have larger ramp durations, up to 3.75 s to stay below the upper limit. Meaning that the choice of the delay and ramp duration are dependant. Overall, the chemical capability of the electrolyser and its power electronic interface is a key requirement for frequency stability. In practice, this raises the question of whether a real electrolyser system can repeatedly and safely follow such fast and large active power setpoint variations.

The sensitivity to the external generator transformer reactance shows a different behaviour. Increasing this reactance weakens the electrical connection between the external generator and the rest of the system. As a result, the voltage profile and the reactive power sharing are affected, while the frequency indicators remain almost unchanged. The voltage peaks and nadir are increasing with a larger reactance. The final frequency stays around 51.2 Hz and the nadir around 49.5 Hz, for all tested values with a response delay of 1 s and ramp speed of 13.3 %/s. The maximum apparent power of the synchronous condenser increases when the transformer reactance increases, from about 38 MVA to 50 MVA. This indicates that a weaker connection to the external generator increases the reactive power burden on the synchronous condenser, even if the active power balance and the frequency response remain almost unchanged.

The inertia sensitivity analysis confirms the expected beneficial effect of additional inertia on frequency dynamics. Increasing the inertia reduces the RoCoF, improves the frequency nadir, and decreases the final frequency. In the analysed case, the retained upper frequency limit is exceeded when the inertia is equal to or lower than the reference value, while higher inertia values keep the final frequency within the acceptable range. The frequency nadir improves from 49.06 to 49.62 Hz. The voltage indicators also slightly improve with increasing inertia, although this effect is indirect and results from the smoother electromechanical response. The maximum apparent power of the synchronous generator and the relative rotor angle deviation are also reduced when inertia is increased. Ranging from 80 MVA to 72 MVA. This suggests that adding inertia, for instance through flywheels coupled to the synchronous condenser, can improve the robustness of the system against active power disturbances.

Finally, the comparison between VSC operating modes shows that converter based voltage control can significantly reduce the reactive power burden on the synchronous machines. When both VSCs operate in PV mode, the voltage dips and peaks are slightly reduced, the reactive power support is shared between the converters, and the maximum apparent power of the synchronous condenser is reduced. In the wind ramp size sensitivity analysis, the maximum apparent power of the synchronous condenser decreases from 42 MVA in the PQ-PQ baseline case to 27 MVA when both VSCs operate in PV mode. The mean reactive power exchanged by the synchronous machines is also reduced.

8 Conclusions and perspectives

8.1 Main conclusions

This master's thesis investigated the dynamic response of a simplified islanded wind to hydrogen production hub. The studied system represents a 750 MW hub containing converter interfaced wind generation and electrolyser demand, a synchronous condenser and an external synchronous generator representing the balancing capability of the surrounding system.

A first part of the work consisted in becoming familiar with the STEPSS/RAMSES simulation environment and with the modelling principles used for power system dynamic simulations. Then, the development of a reduced dynamic model of the hub in this simulation environment was developped. The AC network was built from scratch, and the voltage levels, line parameters and component sizes were chosen to remain consistent with electrical constraints, literature values and industrial orders of magnitude. Existing RAMSES models, including the grid-following VSC, the synchronous condenser and the external synchronous generator models, were reused and adapted to the context of the study. This modelling step also required defining a coherent initial operating point and tuning some parameters in order to obtain a stable reference dynamic behaviour.

The second contribution was the analysis of the system response to wind power variations. Time-domain simulations were used to identify the main physical mechanisms involved after a downward wind power ramps. The results showed that the temporary active power imbalance is first absorbed by the kinetic energy of the synchronous machines and is then mainly compensated by the external synchronous generator. The simulations also showed the importance of the turbine governor dynamics of the external generator, since an excessively slow mechanical response can lead to poorly damped frequency oscillations.

The parametric sensitivity analyses then showed that the most critical aspect of the studied system is not the voltage response, but the frequency response. For the disturbances considered, the voltage magnitudes remained within the retained admissible range. In contrast, the frequency response was highly dependent on the duration of the active power imbalance between wind generation and electrolyser demand. This imbalance is governed mainly by the electrolyser reaction delay, its ramp rate, the turbine-governor response of the external generator and the available inertia.

From a design perspective, the results therefore indicate that the electrolyser cannot be considered only as a passive electrical load. Its ability to rapidly adapt its active power consumption is a key requirement for the stability of an islanded wind to hydrogen system. A delayed or slow electrolyser response increases the transient support required from the external generator and leads to larger frequency deviations. The design of the electrolyser power electronic interface and of its active power control strategy is therefore central for the dynamic performance of the hub.

The analyses also clarified the respective roles of the synchronous support devices. The external synchronous generator mainly provides active power balancing and frequency support, while the synchronous condenser contributes through its inertia during the transient, but its main role remains voltage regulation and reactive power support. Increasing the inertia improves the robustness of the frequency response, whereas a weaker electrical connection to the external generator mainly increases the reactive power burden on the synchronous condenser. Converter based voltage control can reduce this burden by transferring part of the reactive power support from the synchronous machines to the VSCs, but it does not solve the frequency issue.

Overall, this work provides a first RMS dynamic assessment of a reduced islanded wind to hydrogen hub. It shows that such a system requires a coordinated design of the electrolyser active power response, the synchronous generator reserve and governor dynamics, the synchronous condenser sizing, the available inertia and the converter voltage support strategy. The results should therefore be interpreted as preliminary design indications for the operation and further development of large scale islanded wind to hydrogen systems.

8.2 Limitations of the study

The results presented in this thesis must be interpreted while accounting for several modelling assumptions and simplifications.

A first limitation is related to the RMS phasor approximation used in the simulations. It represents the evolution of the fundamental frequency phasors of voltages and currents, but not the complete instantaneous waveforms. Therefore, harmonics and other fast electromagnetic phenomena are not captured, which limits the representation of the detailed behaviour of the VSCs. Nevertheless, the RMS approximation remains appropriate for the electromechanical dynamics, voltage control behaviour and slow converter grid interactions investigated in this work, while keeping the computational cost reasonable for parametric sensitivity analyses.

A second limitation concerns the aggregation of the wind generation unit. In this work, the wind plant is represented by a single equivalent grid following VSC connected directly to the 66 kV collection bus. This is suitable for analysing the dynamic response of the reduced AC system, but it does not explicitly represent the internal collection grid of the wind farm, nor the individual turbine transformers and converters that would be present in a real wind plant. In addition, the wind power variation is imposed as a single active power setpoint ramp at the equivalent converter level, rather than resulting from a detailed wind park control strategy.

The electrolyser model is also simplified. It is represented as a converter interfaced controllable load using the same grid following VSC structure as the wind generation unit. The internal DC electrical circuit and the limitations associated with the chemical conversion process are not explicitly represented. Moreover, the active power response of the electrolyser is imposed manually through predefined setpoint changes, with a chosen delay and ramp rate. It is therefore not generated by an internal feedback controller reacting to system variables such as frequency deviation, available wind generation or active power imbalance. It does not reproduce the full dynamic response of a real electrolyser system.

Finally, the representation of the external system, namely the synchronous generator, does not correspond to a specific physical unit of the industrial project. It is used as an equivalent source providing a voltage angle reference, inertia, active power balance and primary frequency response. This allows the reduced system to exhibit meaningful relative rotor angle dynamics between the synchronous machines, but it does not represent the detailed behaviour of the other hubs. The conclusions related to generator loading, governor response and inertia requirements are therefore dependent on the chosen equivalent model and its parameters.

8.3 Future work

Several extensions could be considered to improve the accuracy and scope of the present study. In particular, future work should further investigate how active power imbalances can be managed in an islanded system with limited external support:

1) In the present model, the equivalent synchronous generator provides a significant part of the active power balancing capability. However, in the industrial project, the neighbouring hubs would also be mainly composed of wind generation and electrolyser loads, and may therefore have limited ability to support another hub during large power imbalances. Future work could therefore analyse weaker representations of the external system, with a reduced contribution from the equivalent generator. This would reduce the dependence on external active power support and create a more demanding scenario for assessing local balancing solutions, such as those suggested in the next points.

2) Additional balancing devices could also be considered. In particular, a grid forming battery could be added to the system, since this technology is already available in real power systems and grid forming models are available in RAMSES. Such a device could provide fast active power support, improve the frequency response and reduce the dependence on the equivalent synchronous generator. This would be particularly relevant for an islanded system with a high share of CIG and load.

3) Finally, the electrolyser active power setpoint could be generated by a feedback control logic instead of being imposed through predefined ramps. For example, the electrolyser consumption could be automatically adjusted according to the frequency deviation or to an estimate of the active power imbalance. This controller should include limiters and ramp rate constraints tuned according to the realistic load variation capabilities of electrolyser systems. This would make it possible to evaluate whether the electrolyser can contribute to frequency stability while respecting its physical and operational constraints.

A Appendix A

A.1 Steady-state error introduced by the AVR & exciter structure of the synchronous machines

The existence of a residual voltage error can be shown by considering a simplified linear representation of the AVR–exciter loop as depicted in Figure 58.

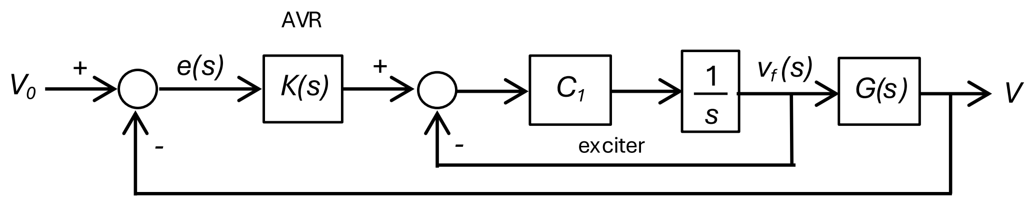

Figure 58: Closed-loop block diagram of the AVR and exciter of the synchronous machines.

Let V_0 be the imposed voltage reference, V the controlled voltage, v_f the field voltage, $K(s)$ the AVR transfer function, and $G(s)$ the unknown equivalent transfer function between the field voltage and the controlled voltage. The voltage error is defined as:

$$e(s) = V_0(s) - V(s). \tag{22}$$

The output of the AVR is therefore:

$$u(s) = K(s)e(s). \tag{23}$$

The exciter contains an integrator, but this integrator is included in a local feedback loop on the field voltage. From the block diagram, the field voltage satisfies:

$$v_f(s) = \frac{C_1}{s}\left[u(s) - v_f(s)\right]. \tag{24}$$

Multiplying both sides by s gives:

$$sv_f(s) = C_1 u(s) - C_1 v_f(s). \tag{25}$$

Hence,

$$(s + C_1)\, v_f(s) = C_1 u(s), \tag{26}$$

and the transfer function of the exciter becomes:

$$\frac{v_f(s)}{u(s)} = \frac{C_1}{s + C_1}. \tag{27}$$

Therefore, the AVR and exciter together are equivalent to:

$$v_f(s) = \frac{C_1 K(s)}{s + C_1} e(s). \tag{28}$$

Since the controlled voltage is related to the field voltage by:

$$V(s) = G(s)v_f(s), \tag{29}$$

one obtains

$$V(s) = G(s)\frac{C_1 K(s)}{s + C_1}\left[V_0(s) - V(s)\right]. \tag{30}$$

Rearranging gives:

$$V(s)\left[1 + \frac{C_1 K(s)G(s)}{s + C_1}\right] = \frac{C_1 K(s)G(s)}{s + C_1}V_0(s). \tag{31}$$

The closed-loop transfer function between the voltage reference and the controlled voltage is therefore:

$$\frac{V(s)}{V_0(s)} = \frac{\dfrac{C_1 K(s)G(s)}{s + C_1}}{1 + \dfrac{C_1 K(s)G(s)}{s + C_1}}. \tag{32}$$

Equivalently,

$$\frac{V(s)}{V_0(s)} = \frac{C_1 K(s)G(s)}{s + C_1 + C_1 K(s)G(s)}. \tag{33}$$

The steady-state gain is obtained by evaluating the closed-loop transfer function at $s = 0$, assuming a stable closed-loop system:

$$\left.\frac{V(s)}{V_0(s)}\right|_{s=0} = \frac{C_1 K(0)G(0)}{C_1 + C_1 K(0)G(0)}. \tag{34}$$

After simplification by C_1, this gives:

$$\frac{V(\infty)}{V_0} = \frac{K(0)G(0)}{1 + K(0)G(0)}. \tag{35}$$

Thus, if the static loop gain $K(0)G(0)$ is finite, the steady-state gain is different from unity:

$$\frac{V(\infty)}{V_0} \neq 1. \tag{36}$$

Consequently, the controlled voltage does not exactly recover the imposed voltage reference in steady state. The corresponding relative steady-state error is:

$$\frac{e(\infty)}{V_0} = 1 - \frac{V(\infty)}{V_0}. \tag{37}$$

Using the previous expression,

$$\frac{e(\infty)}{V_0} = 1 - \frac{K(0)G(0)}{1 + K(0)G(0)}. \tag{38}$$

Therefore,

$$\frac{e(\infty)}{V_0} = \frac{1}{1 + K(0)G(0)}. \tag{39}$$

This result shows that the AVR reduces the steady-state voltage error, but does not eliminate it completely as long as the static loop gain remains finite. Although the exciter contains an integrator, this integrator is included in a local feedback loop on v_f. The exciter therefore behaves as a first-order system with finite static gain,

$$\left.\frac{v_f(s)}{u(s)}\right|_{s=0} = 1, \tag{40}$$

rather than as a pure integrator with infinite static gain. A zero steady-state voltage error would require an infinite static loop gain, for instance through a pure integral action on the voltage error.

B Appendix B

B.1 Additional results for the sensitivity analysis

B.1.1 Sensitivity to wind ramp size variation

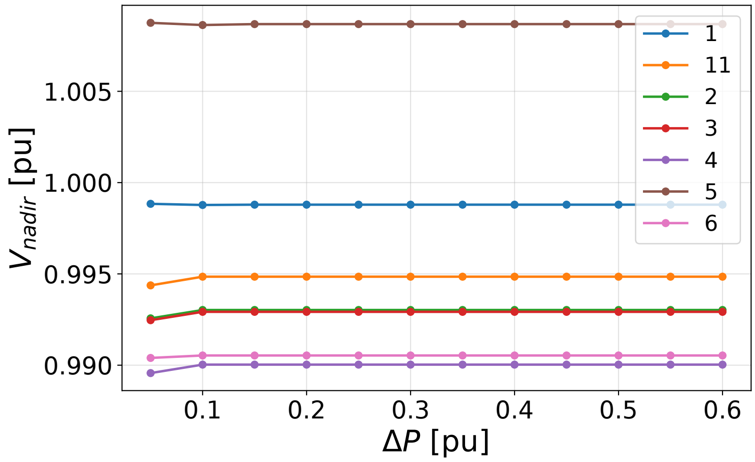

Figure 59: Voltage nadir at each bus of the network during each simulation as a function of the downward wind ramp size ΔP_{wind}.

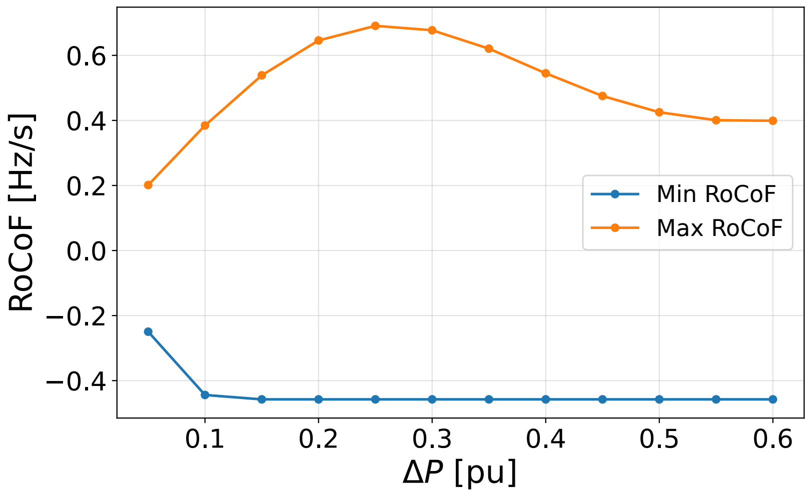

Figure 60: Min and max ROCOF as a function of the downward wind ramp size ΔP_{wind}.

B.1.2 Electrolyser reaction delay variation

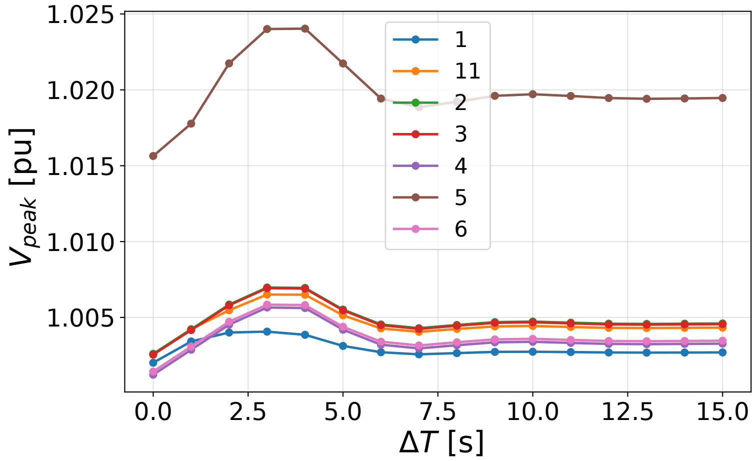

Figure 61: Voltage peaks at each bus of the network during the simulation for different values of the electrolyser reaction delay ΔT.

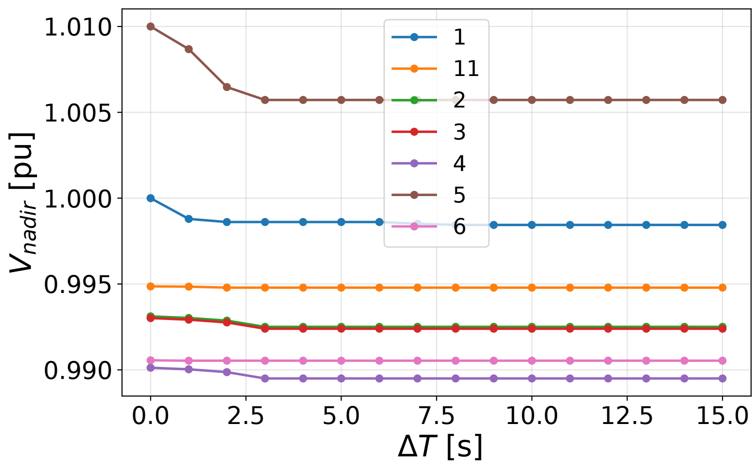

Figure 62: Voltage nadir at each bus of the network during each simulation as a function of the electrolyser reaction delay ΔT.

Figure 63 shows that the influence of the electrolyser reaction delay remains limited. The synchronous condenser provides most of the reactive power support, with a mean value around 30 MVAr, whereas the synchronous generator exchanges only a small amount of reactive power, close to zero compared with the condenser. For the synchronous condenser, the mean reactive power slightly increases when the delay ΔT becomes larger. This can be explained by the fact that, for larger delays, the system remains for a longer time in an intermediate operating condition where the wind power has already decreased while the electrolyser consumption has not yet been reduced. During this period, the voltage profile is more affected by the disturbance, which requires slightly more reactive power support from the synchronous condenser.

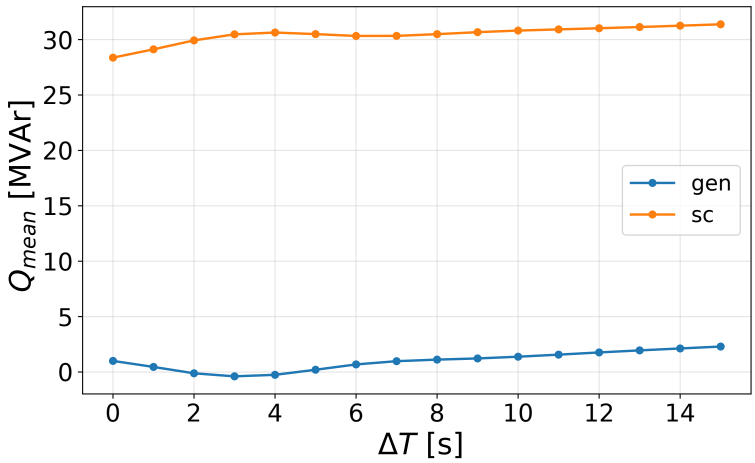

Figure 63: Mean reactive power exchanged by the synchronous machines for different values of the electrolyser reaction delay ΔT.

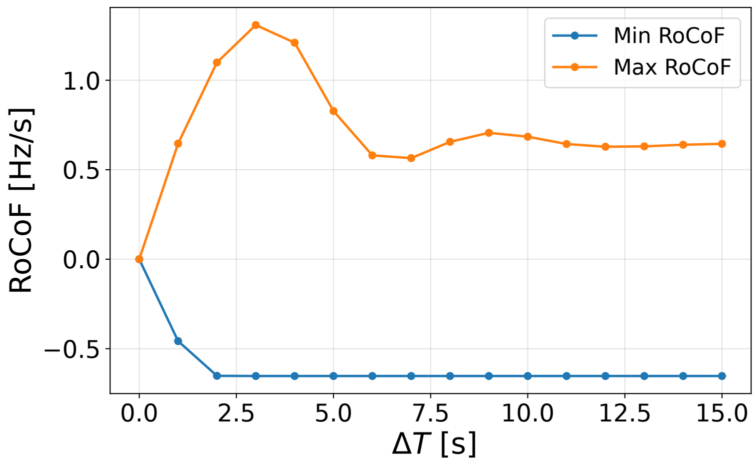

Figure 64: Min and max ROCOF for different values of the electrolyser reaction delay ΔT.

B.1.3 Influence of the electrolyser ramp slope

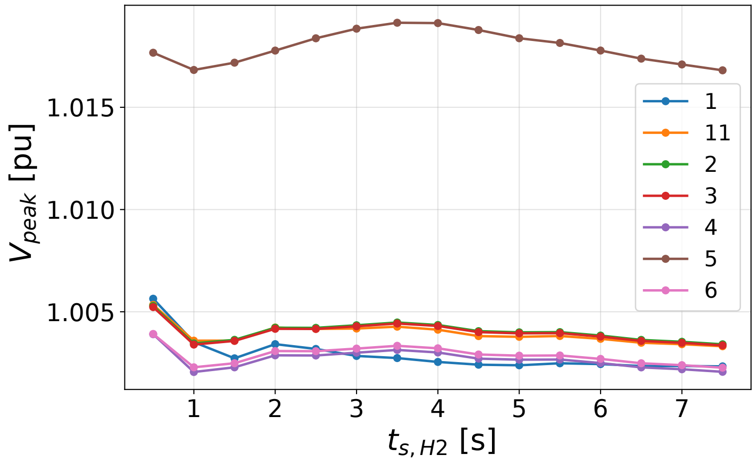

Figure 65: Voltage peaks at each bus of the network for different durations of the electrolyser ramp.

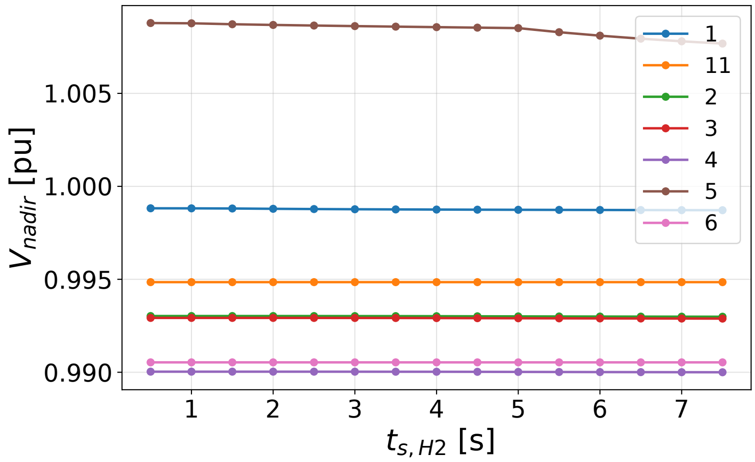

Figure 66: Voltage peaks at each bus of the network for different durations of the electrolyser ramp.

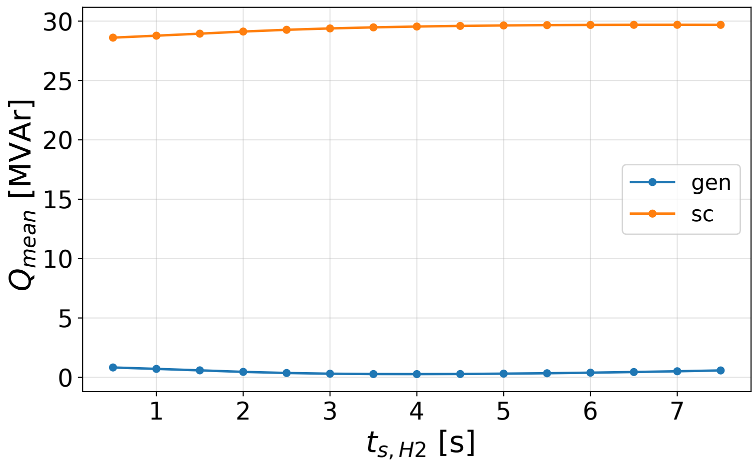

Figure 67: Mean reactive power exchanged by the synchronous machines for different durations of the electrolyser ramp.

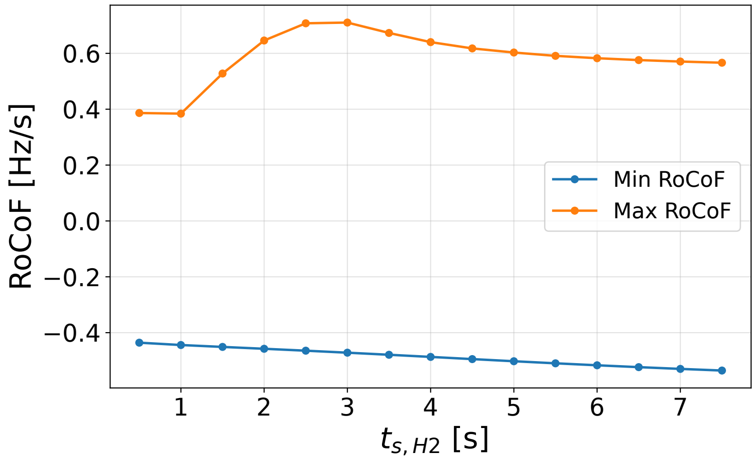

Figure 68: Min and max ROCOF for different durations of the electrolyser ramp.

B.1.4 Sensitivity to external grid strength variation

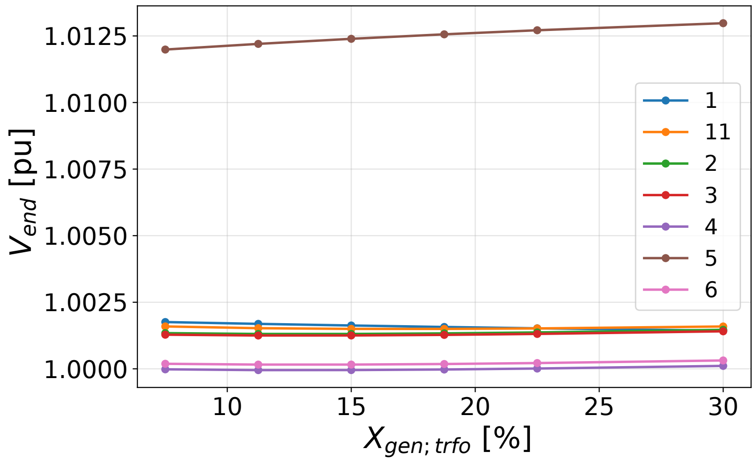

Figure 69: Final voltage magnitudes at each bus of the network for different values of the external generator transformer reactance $X_{gen;ext}$.

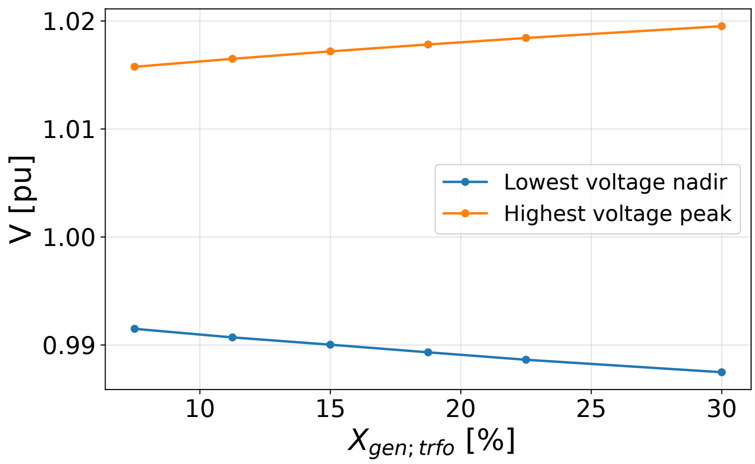

Figure 70: Highest and lowest voltage magnitudes for different values of the external generator transformer reactance $X_{gen;ext}$.

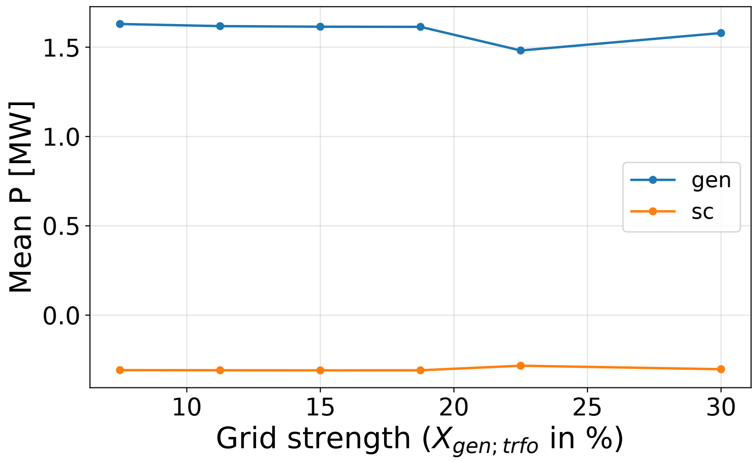

Figure 71: Mean active power exchanged by the synchronous machines for different values of the external generator transformer reactance $X_{gen;ext}$.

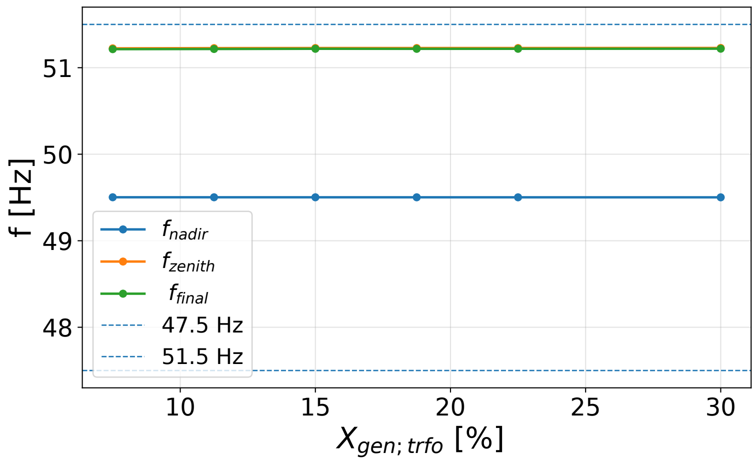

Figure 72: Final, zenith and nadir frequencies for different values of the external generator transformer reactance $X_{gen;ext}$.

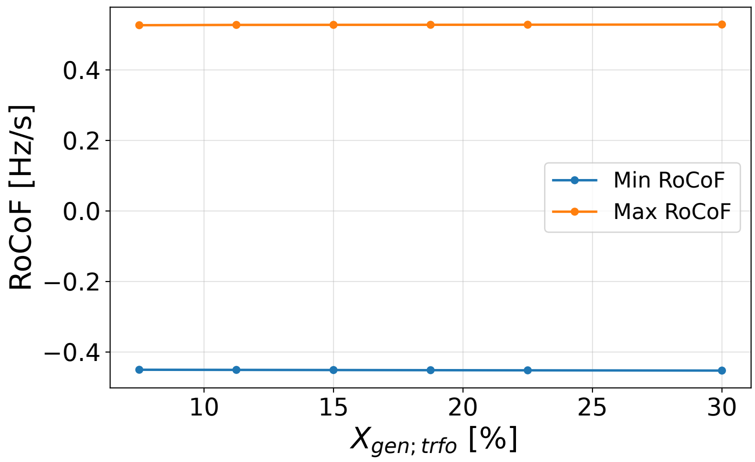

Figure 73: Min and max ROCOF for different values of the external generator transformer reactance $X_{gen;ext}$.

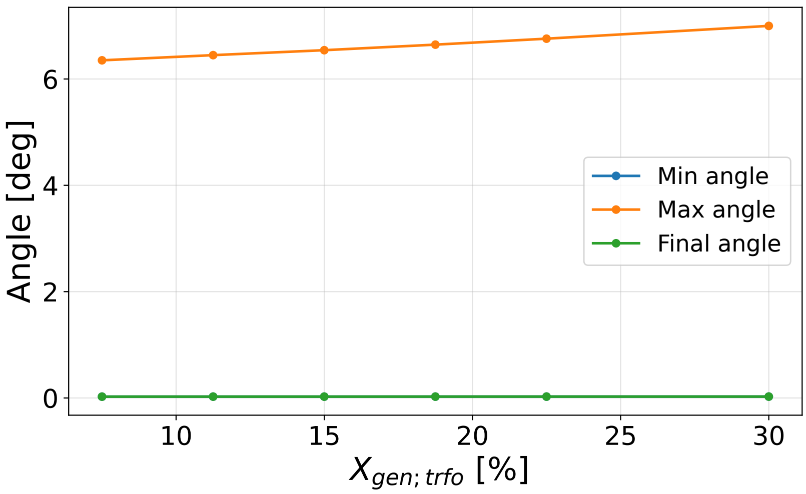

Figure 74: Extrema and final value of the relative rotor angle between the synchronous machines for different values of the external generator transformer reactance $X_{gen;ext}$.

B.1.5 Sensitivity to inertia

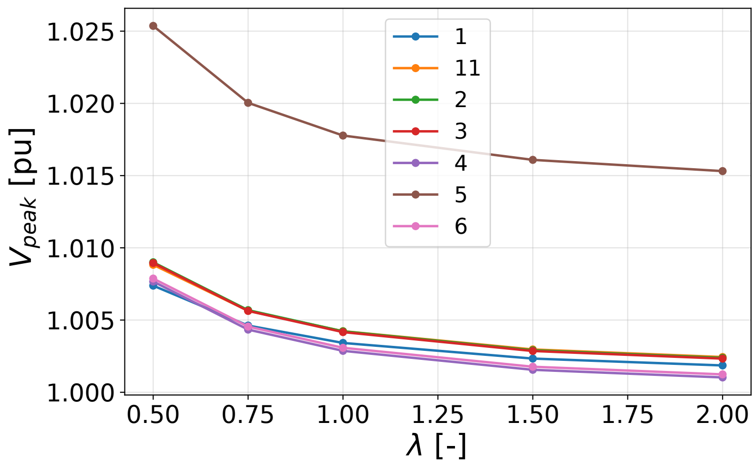

Figure 75: Voltage peaks at each bus of the network for different values of the multiplier *lambda*.

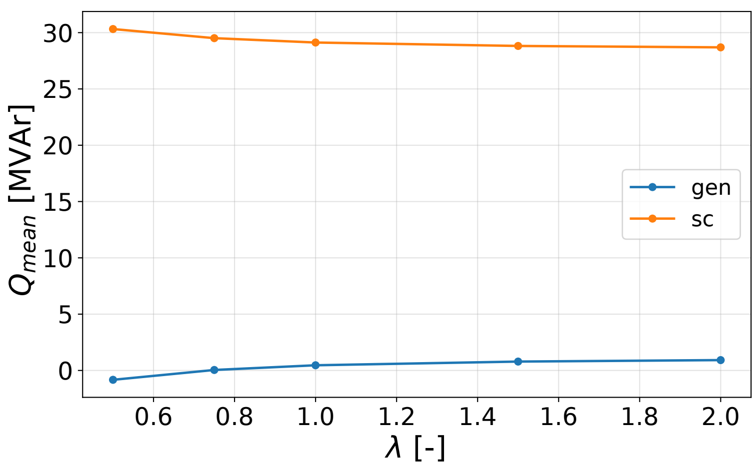

Figure 76: Mean reactive power exchanged by the synchronous machines for different values of the multiplier *lambda*.

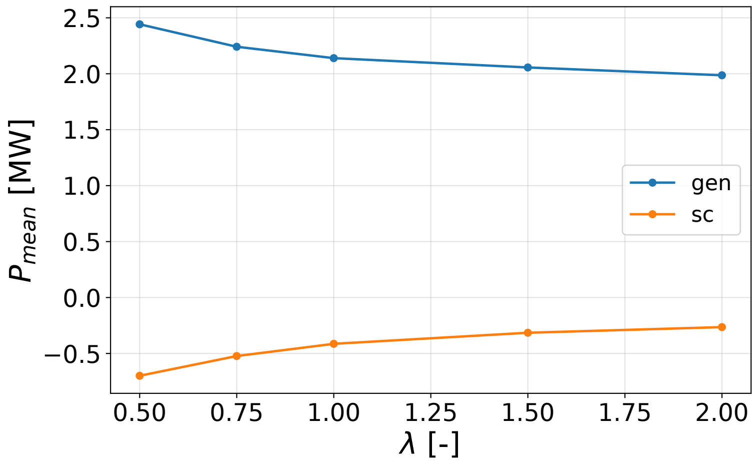

Figure 77: Mean active power exchanged by the synchronous machines for different values of the multiplier *lambda*.

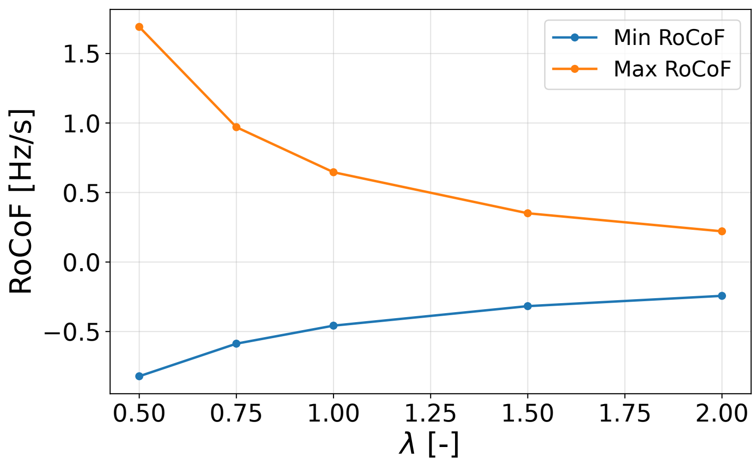

Figure 78: Min and max ROCOF for different values of the multiplier *lambda*.

C Appendix C

This appendix summarises the main input data used in the load-flow file `lf.dat` and in the dynamic data file `dyn.dat`. The data include the bus definitions, the network branches, the transformers, the static operating point of the devices, and the main dynamic parameters of the synchronous machines and VSCs.

C.1 Load-flow input data

Table 15: Bus data used in the load-flow file.

Bus	V_{nom} (kV)	P_{load}	Q_{load}	B_{shunt}	Main associated device
1	15	0	0	0	External synchronous generator
11	220	0	0	0	Generator transformer HV side
2	220	0	0	0	Wind-side HV bus
3	220	0	0	0	Electrolyser and synchronous condenser HV bus
4	20	0	0	0	Electrolyser VSC
5	15	0	0	0	Synchronous condenser
6	66	0	0	0	Wind VSC

Table 16: Line data used in the load-flow file.

Line	From bus	To bus	R	X	$\omega C/2$	S_N (MVA)
1–2	11	2	0.78	5.64	26.411	1000
1–2bis	11	2	0.78	5.64	26.411	1000
2–3	2	3	0.02	0.12	0.556	1000
2–3bis	2	3	0.02	0.12	0.556	1000

Table 17: Transformer data used in the load-flow file.

Transformer	From bus	To bus	R	X	N	S_N (MVA)
`eol_trf`	6	2	0.0	12	100.0	850
`load_trfo`	3	4	0.0	12	100.0	800
`sync_trfo`	3	5	0.0	12	100.0	300
`gen_trfo`	1	11	0.0	15	100.0	800

Table 18: Static device data used in the load-flow file.

Device	Bus	P (MW)	Q (MVAr)	V_{imp} (pu)	S_N (MVA)	$Q_{\min}$	$Q_{\max}$
`gen`	1	0	0	1.00	800	-500	500
`sc`	5	0	0	1.01	300	-9999	9999
`VSC_WIND`	6	500	0	0	800	-9999	9999
`H2_load`	4	-500	0	0	-800	-9999	9999

C.2 Dynamic input data

The nominal frequency used in the dynamic simulations is $f_N = 50$ Hz.

Table 19: Grid-following VSC dynamic and control parameters used for the wind and electrolyser converters.

Parameter	`VSC_WIND`	`H2_load`
Model	`GFOL_det`	`GFOL_det`
Bus	6	4
F_P	1.0	1.0
F_Q	1.0	1.0
P	0.0	0.0
Q	0.0	0.0
S_N (MVA)	800	800
R	0.005	0.005
L	0.15	0.15
r	1.02	1.02
R_c	0.005	0.005
X_c	0.15	0.15
K_p	0.5730	0.5730
K_i	6	6
T_{lpf}	0.0033	0.0033
K_{pp}	0.0333	0.0333
K_{ip}	10	10
T_{rlim}	0.002	0.002
dP/dt_{min}	-999	-999
dP/dt_{max}	10	10
K_{pv}	0.1667	0.1667
K_{iv}	50	50
τ	0.10	0.10
V_{pllb}	0.4	0.4
V_{pllu}	0.5	0.5
I_{max}	1.000	1.000
V_{s1}	-1000	-1000
V_{s2}	-2000	-2000
$i_{q1,\text{max}}$	1.001	1.001
$v_{q,\text{switch}}$	0	0

Table 20: Main synchronous-machine dynamic parameters.

Parameter	`sc`	`gen`
Bus	5	1
F_P	1.0	1.0
F_Q	1.0	1.0
P	0.0	0.0
Q	0.0	0.0
S_N (MVA)	300	800
P_{nom} (MW)	0	750
H (s)	2	4
D	0	0
IBRATIO	1.40	2.05
Model type	`XT`	`XT`
X_l	0.15	0.15
X_d	1.55	2.20
X'_d	0.30	0.30
X''_d	0.20	0.20
X_q	1.00	2.00
X'_q	–	0.40
X''_q	0.20	0.20
m	0.1	0.1
n	6.0257	6.0257
R_a	0.0	0.0
T'_{do}	7.00	7.00
T''_{do}	0.05	0.05
T'_{qo}	–	1.50
T''_{qo}	0.10	0.05
Excitation model	`GENERIC1`	`exc_GENERIC3`
Torque model	`CONSTANT`	`THERMAL_GENERIC1`

Table 21: Excitation and stabilisation parameters of the synchronous condenser.

Parameter	`sc`
Excitation model	`GENERIC1`
I_{flim}	2.9579
d	-0.1
f	0.0
S	1.0
K_1	100
K_2	-1
L_1	-17
L_2	10
G	50
T_A	4
T_B	20
T_E	0.1
L_3	0.0
L_4	4.0
SPEEDIN	1
K_{PSS}	0.0
T_w	10
T_1	10
T_2	2
T_3	10
T_4	2
ΔV_{min}	0.00
ΔV_{max}	0.00

Table 22: Excitation-system and PSS parameters of the external synchronous generator.

Parameter	`gen`
Excitation model	`exc_GENERIC3`
G	70
T_a	1.0
T_b	1.0
T_e	0.4
$v_{f,\min}$	0.0
$v_{f,\max}$	5.0
K_{PSS}	0.0
T_w	5.0
T_1	0.323
T_2	0.0138
T_3	0.323
T_4	0.0138
C	0.06
$if_{1,\mathrm{lim}}$	2.90
$if_{2,\mathrm{lim}}$	1.00
T_{oel}	12.0
K_{oel}	2.0
L_1	-1.10
L_2	0.10
L_3	0.20

Table 23: Thermal governor and turbine parameters of the external synchronous generator.

R	T_{mes}	T_{sm}	$\dot{z}_{\min}$	$\dot{z}_{\max}$	$z_{\min}$	$z_{\max}$	T_{hp}	f_{hp}	T_r	f_{mp}	T_{lp}
0.04	0.10	0.40	-0.2	0.2	0.0	1.0	0.3	0.4	5.0	0.3	0.3

References

[1] M. Bar and O. Leukhina, “Demographic transition and industrial revolution: A macroeconomic investigation,” *Review of Economic Dynamics*, vol. 13, no. 2, pp. 424–451, Apr. 2010. DOI: 10.1016/j.red.2009.03.002 Accessed: Apr. 22, 2026.

[2] R. Lee, “The Demographic Transition: Three Centuries of Fundamental Change,” en, *Journal of Economic Perspectives*, vol. 17, no. 4, pp. 167–190, Dec. 2003. DOI: 10.1257/089533003772034943 Accessed: Apr. 22, 2026.

[3] D. Cutler, A. Deaton, and A. Lleras-Muney, “The Determinants of Mortality,” en, *Journal of Economic Perspectives*, vol. 20, no. 3, pp. 97–120, Sep. 2006. DOI: 10.1257/jep.20.3.97 Accessed: Apr. 22, 2026.

[4] P. Malanima, “Energy, productivity and structural growth. The last two centuries,” *Structural Change and Economic Dynamics*, vol. 58, pp. 54–65, Sep. 2021. DOI: 10.1016/j.strueco.2021.04.003 Accessed: Apr. 23, 2026.

[5] “Energy Systems,” in *Climate Change 2022 - Mitigation of Climate Change: Working Group III Contribution to the Sixth Assessment Report of the Intergovernmental Panel on Climate Change*, Intergovernmental Panel on Climate Change (IPCC), Ed., Cambridge: Cambridge University Press, 2023, pp. 613–746. DOI: 10.1017/9781009157926.008 Accessed: Apr. 23, 2026.

[6] K. Calvin et al., “IPCC, 2023: Climate Change 2023: Synthesis Report. Contribution of Working Groups I, II and III to the Sixth Assessment Report of the Intergovernmental Panel on Climate Change [Core Writing Team, H. Lee and J. Romero (eds.)]. IPCC, Geneva, Switzerland.,” und, Intergovernmental Panel on Climate Change (IPCC), Tech. Rep., 2023. DOI: 10.59327/ipcc/ar6-9789291691647 Accessed: Apr. 23, 2026.

[7] H.-O. Pörtner et al., Eds., *Climate Change 2022: Impacts, Adaptation and Vulnerability. Contribution of Working Group II to the Sixth Assessment Report of the Intergovernmental Panel on Climate Change.* 2022. DOI: https://doi.org/10.48490/2w53-yw15

[8] A. Grubler et al., “A low energy demand scenario for meeting the 1.5 °C target and sustainable development goals without negative emission technologies,” en, *Nature Energy*, vol. 3, no. 6, pp. 515–527, Jun. 2018. DOI: 10.1038/s41560-018-0172-6 Accessed: May 19, 2026.

[9] B. van der Zwaan et al., “Electricity- and hydrogen-driven energy system sector-coupling in net-zero CO2 emission pathways,” en, *Nature Communications*, vol. 16, no. 1, p. 1368, Feb. 2025. DOI: 10.1038/s41467-025-56365-0 Accessed: Apr. 24, 2026.

[10] S. J. Davis et al., “Net-zero emissions energy systems,” *Science*, vol. 360, no. 6396, Jun. 2018. DOI: 10.1126/science.aas9793 Accessed: Apr. 24, 2026.

[11] I. Eryazici, N. Ramesh, and C. Villa, “Electrification of the chemical industry—materials innovations for a lower carbon future,” en, *MRS Bulletin*, vol. 46, no. 12, pp. 1197–1204, Dec. 2021. DOI: 10.1557/s43577-021-00243-9 Accessed: Apr. 25, 2026.

[12] IRENA and WTA, "International trade and green hydrogen: Supporting the global transition to a low-carbon economy," en, Tech. Rep., Dec. 2023. Accessed: Apr. 26, 2026. [Online]. Available: https://www.irena.org/Publications/2023/Dec/International-trade-and-green-hydrogen-Supporting-the-global-transition-to-a-low-carbon-economy

[13] IEA, *Executive summary – Global Hydrogen Review 2025 – Analysis*, en-GB, Paris. Accessed: May 19, 2026. [Online]. Available: https://www.iea.org/reports/global-hydrogen-review-2025/executive-summary

[14] IRENA, "Global Hydrogen Trade to Meet the 1.5°C Climate Goal: Green Hydrogen Cost and Potential," en, Tech. Rep., May 2022. Accessed: May 19, 2026. [Online]. Available: https://www.irena.org/Publications/2022/May/Global-hydrogen-trade-Cost

[15] Carlos, Cacciuttolo, Ariana, Huertas, Bryan, Montoya, and Deyvis, Cano, "The Present and Future of Production of Green Hydrogen, Green Ammonia, and Green E-Fuels for the Decarbonization of the Planet from the Magallanes Region, Chile," Jun. 2025. DOI: https://doi.org/10.3390/app15116228 Accessed: May 19, 2026.

[16] S. Karimi, P. Musilek, and A. M. Knight, "Dynamic thermal rating of transmission lines: A review," *Renewable and Sustainable Energy Reviews*, vol. 91, pp. 600–612, Aug. 2018. DOI: 10.1016/j.rser.2018.04.001 Accessed: May 20, 2026.

[17] P. Kundur, *Power System Stability and Control*, 3rd ed. CRC Press, 2012.

[18] L. Bauer, *Siemens Gamesa SG 6.0-154 - 6,00 MW - éolienne*, fr. Accessed: May 20, 2026. [Online]. Available: https://fr.wind-turbine-models.com/turbines/1886-siemens-gamesa-sg-6-0-154

[19] P. Lakshmanan, R. Sun, and J. Liang, "Electrical collection systems for offshore wind farms: A review," *CSEE Journal of Power and Energy Systems*, vol. 7, no. 5, pp. 1078–1092, Sep. 2021. DOI: 10.17775/CSEEJPES.2020.05050 Accessed: May 20, 2026.

[20] M. Chen, S.-F. Chou, F. Blaabjerg, and P. Davari, "Overview of Power Electronic Converter Topologies Enabling Large-Scale Hydrogen Production via Water Electrolysis," en, *Applied Sciences*, vol. 12, no. 4, p. 1906, Jan. 2022. DOI: 10.3390/app12041906 Accessed: May 20, 2026.

[21] Van Cutsem, Thierry and Papangelis, Lampros, "Description, Modeling and Simulation Results of a Test System for Voltage Stability Analysis - 2013," Université de Liège, Tech. Rep., Nov. 2013, pp. 1–49. Accessed: Mar. 19, 2026. [Online]. Available: https://orbi.uliege.be/handle/2268/141234

[22] International Electrotechnical Commission, *Power transformers – Part 5: Ability to withstand short circuit*, English, Geneva, Switzerland, 2006. Accessed: May 27, 2026. [Online]. Available: https://www.iecee.org/certification/iec-standards/iec-60076-52006

[23] P. Kundur et al., "Definition and Classification of Power System Stability IEEE/CIGRE Joint Task Force on Stability Terms and Definitions," *Power Systems, IEEE Transactions on*, vol. 19, pp. 1387–1401, Sep. 2004. DOI: 10.1109/TPWRS.2004.825981

[24] N. Hatziargyriou et al., “Stability definitions and characterization of dynamic behavior in systems with high penetration of power electronic interfaced technologies,” English, Institute of Electrical, Electronics Engineers (IEEE), and Energy Society, Technical Report PES-TR77, Apr. 2020. DOI: 10.17023/zwwp-vv02 Accessed: Feb. 20, 2026.

[25] J. Morren, S. de Haan, W. Kling, and J. Ferreira, “Wind turbines emulating inertia and supporting primary frequency control,” *IEEE Transactions on Power Systems*, vol. 21, no. 1, pp. 433–434, Feb. 2006. DOI: 10.1109/TPWRS.2005.861956 Accessed: May 15, 2026.

[26] G. Lalor, A. Mullane, and M. O’Malley, “Frequency control and wind turbine technologies,” *IEEE Transactions on Power Systems*, vol. 20, no. 4, pp. 1905–1913, Nov. 2005. DOI: 10.1109/TPWRS.2005.857393 Accessed: May 15, 2026.

[27] M. Kayikci and J. V. Milanovic, “Dynamic Contribution of DFIG-Based Wind Plants to System Frequency Disturbances,” *IEEE Transactions on Power Systems*, vol. 24, no. 2, pp. 859–867, May 2009. DOI: 10.1109/TPWRS.2009.2016062 Accessed: May 15, 2026.

[28] European Commission, *Commission Regulation (EU) 2016/631 of 14 April 2016 establishing a network code on requirements for grid connection of generators (Text with EEA relevance)*, en, Table 2: Frequency ranges and minimum time periods for operation, Apr. 2016. Accessed: May 12, 2026. [Online]. Available: http://data.europa.eu/eli/reg/2016/631/oj

[29] Z. Liu, S. Miao, Z. Fan, J. Liu, and Q. Tu, “Improved power flow control strategy of the hybrid AC/DC microgrid based on VSM,” en, *IET Generation, Transmission & Distribution*, vol. 13, no. 1, pp. 81–91, 2019. DOI: 10.1049/iet-gtd.2018.5839 Accessed: May 13, 2026.

[30] W. Du et al., “Modeling of Grid-Forming and Grid-Following Inverters for Dynamic Simulation of Large-Scale Distribution Systems,” *IEEE Transactions on Power Delivery*, vol. 36, no. 4, pp. 2035–2045, Aug. 2021. DOI: 10.1109/TPWRD.2020.3018647 Accessed: May 13, 2026.

[31] X. Shan, K. Hou, L. Guo, C. Niu, and G. Cai, “Active Support Control for Hybrid Renewable Energy Stations with Grid-Following and Grid-Forming Capabilities Considering Grid Strength,” en, *Journal of Physics: Conference Series*, vol. 3012, no. 1, p. 012 020, Jun. 2025. DOI: 10.1088/1742-6596/3012/1/012020 Accessed: May 13, 2026.

[32] H. Gong, X. Wang, and L. Harnefors, “Rethinking Current Controller Design for PLL-Synchronized VSCs in Weak Grids,” *IEEE Transactions on Power Electronics*, vol. 37, no. 2, pp. 1369–1381, Feb. 2022. DOI: 10.1109/TPEL.2021.3105549 Accessed: May 15, 2026.

[33] P. Tielens and D. Van Hertem, “The relevance of inertia in power systems,” *Renewable and Sustainable Energy Reviews*, vol. 55, pp. 999–1009, Mar. 2016. DOI: 10.1016/j.rser.2015.11.016 Accessed: May 11, 2026.

[34] F. P. Demello and C. Concordia, “Concepts of Synchronous Machine Stability as Affected by Excitation Control,” *IEEE Transactions on Power Apparatus and Systems*, vol. PAS-88, no. 4, pp. 316–329, Apr. 1969. DOI: 10.1109/TPAS.1969.292452 Accessed: Apr. 11, 2026.

[35] Mircea, Eremia and Mohammad, Shahidehpour, *Handbook of Electrical Power System Dynamics*, en. John Wiley & Sons, Ltd, 2013. DOI: 10.1002/9781118516072.fmatter Accessed: Apr. 8, 2026.

[36] F. Milano, F. Dörfler, G. Hug, D. J. Hill, and G. Verbič, "Foundations and Challenges of Low-Inertia Systems (Invited Paper)," en, in *2018 Power Systems Computation Conference (PSCC)*, Dublin, Ireland: IEEE, Jun. 2018, pp. 1–25. DOI: 10.23919/PSCC.2018.8450880 Accessed: May 17, 2026.

[37] R. Ma, Q. Qiu, J. Kurths, and M. Zhan, "Fast-Slow-Scale Interaction Induced Parallel Resonance and its Suppression in Voltage Source Converters," *IEEE Access*, vol. 9, pp. 90 126–90 141, 2021. DOI: 10.1109/ACCESS.2021.3091510 Accessed: May 17, 2026.

[38] C. Eckel, D. Babazadeh, and C. Becker, "Classification of Converter-Driven Stability and Suitable Modeling and Analysis Methods," *IEEE Access*, vol. 12, pp. 53 056–53 073, 2024. DOI: 10.1109/ACCESS.2024.3388098 Accessed: May 17, 2026.

[39] Van Cutsem, Thierry, *Grid-following Voltage Source Converter: Modelling under phasor approximation and simulation results on the 4-VSC test system*, English, Unpublished presentation slides, Internal course material., May 2024.

[40] Van Cutsem, Thierry, *Power system dynamics, control and stability: Models, case studies and discussions*, English, Unpublished workshop slides, Includes the 5-bus test system, synchronous machine, speed governor, automatic voltage regulator, excitation system and overexcitation limiter models., Feb. 2025.

[41] Siemens Energy, *Synchronous condenser for grid stability and efficiency*, en. Accessed: May 20, 2026. [Online]. Available: https://www.siemens-energy.com/global/en/home/products-services/product/synchronous-condenser.html